Stockholm University

FLAIR
Facility for Low-energy Antiproton and Ion Research

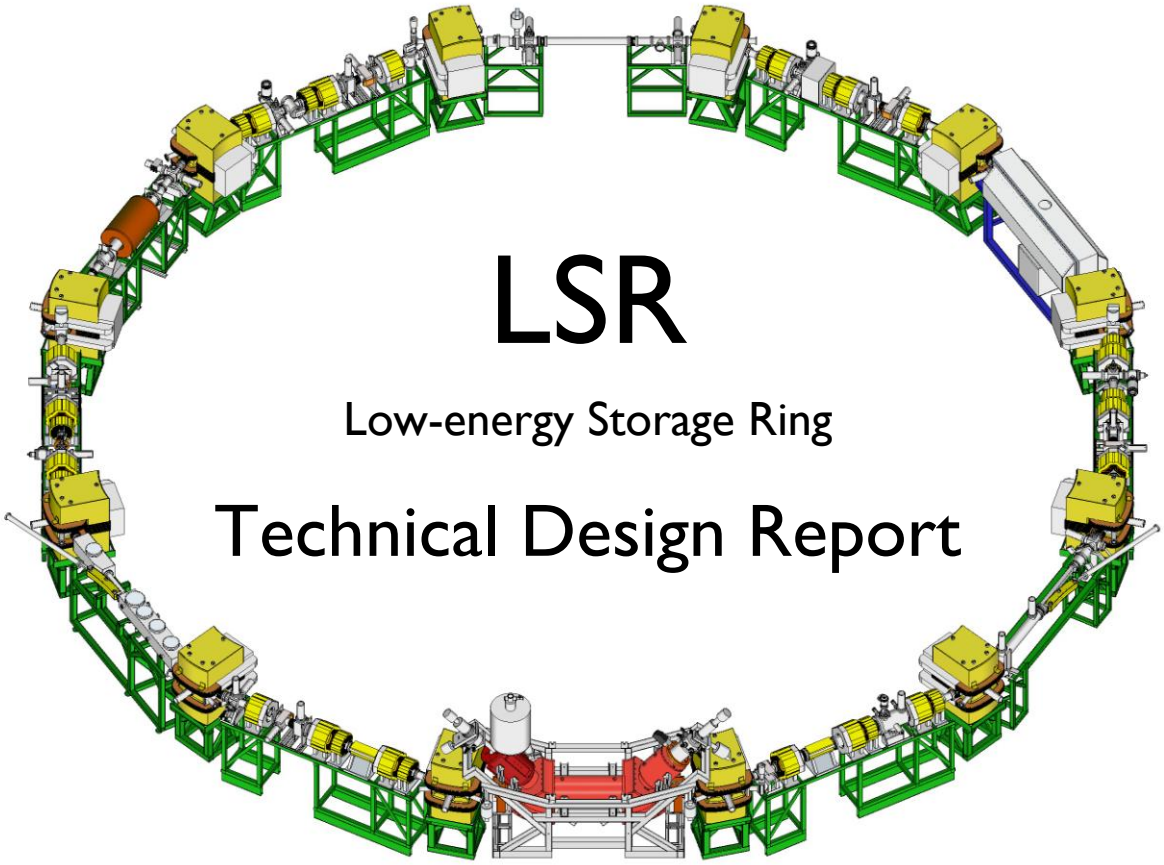

LSR

Low-energy Storage Ring

Technical Design Report

Version 1.2 Draft

Stockholm University
4 February 2011

LSR
Low-energy Storage Ring
Technical Design Report

Håkan Danared, Guillermo Andler, Mikael Björkhage, Mikael Blom, Lars Brännholm, Peter Carlé, Kjell Ehrnstén, Mats Engström, Anders Hedqvist, Fredrik Hellberg, Anders Källberg, Sven Leontein, Leif Liljeby, Patrik Löfgren, Andras Paál, Dag Reistad, K.-G. Rensfelt, Ansgar Simonsson, Jan Sjöholm and Örjan Skeppstedt

Stockholm University
4 February 2011

Table of Contents

1. About This Report

This design report is intended to serve several different purposes: to give an overview of the basic CRYRING hardware that has been built up since the start of the project, to describe in more detail the modifications that have been and will have to be made to adapt the ring to its new use at FLAIR, to give a short introduction to operational aspects, and also to serve as a guide to further documentation.

After the introduction in chapter 2, chapter 3 provides a description of CRYRING such as it looked before the implementation of the FLAIR-related modifications started, giving information about the major components that CRYRING consists of. However, the ring has been in operation for almost two decades, and this report is not intended to constitute a basis for the evaluation of the individual hardware components from a functional point of view. Instead, the Manne Siegbahn Laboratory has since the start of the discussions to move CRYRING to FAIR made efforts to show through machine experiments that the ring, as a sum of all individual components, will be able to function as an antiproton and heavy-ion decelerator. In other words, the results of these experiments rather than studies and evaluation of the hardware components should provide the basis for a decision on CRYRING's suitability for its new task. Thus, the description of the hardware components in chapter 3 is complemented with results from studies at CRYRING of maximal stored beam currents, cooling times, deceleration cycles and deceleration efficiencies in chapter 7.

It is different with the modifications that are made to the ring, mainly consisting of new injection and extraction systems. Of these, only the slow extraction has been implemented and tested. (It was originally planned that also fast extraction and aspects of the new injection should be tested before the transfer to FAIR, but this has not been possible due to the delays of the FAIR project and consequent delays in the funding to MSL.) Instead, the new injection and extraction systems are described in considerably more detail than the previously existing hardware, in order to allow a careful review of their design. For the slow extraction, also results of detailed numerical simulations based on particle tracking are presented. Chapter 4 gives an overview of the modifications while chapters 5 and 6 discuss injection and extraction respectively. Results from tests of slow extraction are also presented in chapter 6.

2. Introduction

2.1. The FLAIR Facility

FLAIR [1], the Facility for Low-energy Antiproton and Ion Research at FAIR, will be the next-generation facility for physics with low-energy antiprotons, providing the world's highest fluxes of antiprotons at energies from tens of MeV down to rest. It will also offer unique possibilities for physics with highly charged ions at very low energies. The physics at FLAIR was evaluated by one of the programme advisory committees (APPA PAC) appointed by International Steering Committee of FAIR in 2005 at the same time as the other proposed experiments at FAIR were evaluated. The committee noted that "FLAIR will be the world's unique facility combining low energy antiprotons and exotic ions" and describes "its extraordinary significance and recommends it to become an integral part of the FAIR facilities". The physics case for FLAIR has thus already been reviewed, and will not be commented upon any further in this Technical Design Report.

FLAIR will obtain beams of already decelerated antiprotons and ions from the NESR ring. The particles will then be further decelerated in one magnetic deceleration ring, the Low-energy Storage Ring LSR which will be the modified CRYRING, and in one electrostatic ring, the Ultralow-energy Storage Ring USR, such that antiprotons can be delivered to experiments at a kinetic energy of only 20 keV. Also ions can be decelerated to low energies, limited by the increasing rate of recombination in collisions with residual-gas atoms as the energy is reduced, and by the consequent rapid reduction of the lifetime of stored beams of highly charged ions at low energies. Furthermore, antiprotons and ions can be decelerated by HITRAP for other experiments at very low energies or sent directly to experiments from the NESR or the LSR.

The perhaps most important new feature at FLAIR, as compared to the Antiproton Decelerator, AD, at CERN, is that antiprotons will be phase-space cooled at several energies during the entire deceleration process. The high production rate of antiprotons at FAIR, compared to what is currently achievable at CERN, can thus be combined with beams that have the smallest possible emittance. This results in a beam intensity at low energies, expressed as the number of particles per unit time, energy spread and transverse emittance, that is orders of magnitude higher than what is available today.

The current layout of the FLAIR hall is seen in fig. 2.1. Antiprotons will be delivered from NESR to the first deceleration ring, the Low-energy Storage Ring LSR, in the FLAIR building at a kinetic energy of 30 MeV. In the LSR, the antiprotons can be decelerated down to 300 keV, or possibly somewhat lower if this is desirable. At 300 keV, the antiprotons are extracted to the electrostatic Ultralow-energy Storage Ring, USR, for further deceleration down to, at minimum, 20 keV. At that energy the particles can be trapped electrostatically and brought to rest at earth potential by lowering the trap voltage from 20 kV to zero. The LSR will, however, not be limited to extraction at the lowest energy, but antiprotons can be extracted at any energy between 30 MeV and 300 keV. For example, antiprotons will be delivered to HITRAP at 4.2 MeV.

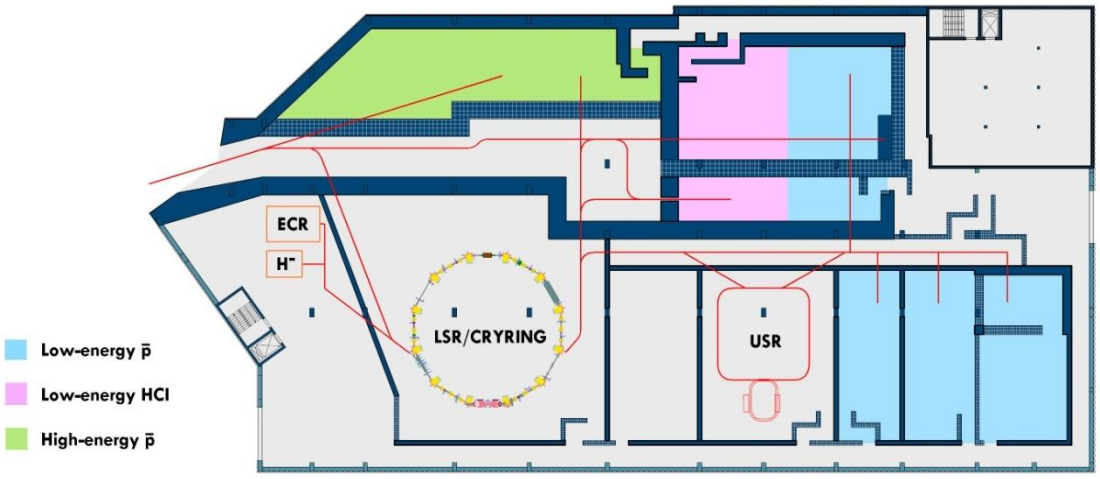

Fig. 2.1. Current preliminary layout of the FLAIR hall. Coloured areas represent halls for experiments with different kind of particles and different energies. Gray areas represent space for accelerator equipment and for other use.

Ions will be injected from NESR to the LSR at the same magnetic rigidity $B\rho$ of 0.80 Tm as 30 MeV antiprotons have, or at an energy of 30 Z^2/A^2 MeV/u, where Z is the charge state of the ion and A is its mass number. The ions can be decelerated and extracted over the same range of rigidities as the antiprotons, although the lowest limit may in reality be determined by the beam lifetime as already mentioned.

2.2. CRYRING

The LSR ring will consist of today's CRYRING synchrotron and storage ring [2] at the Manne Siegbahn Laboratory, MSL, in Stockholm. CRYRING, the operation of which has recently stopped at MSL, has been used during almost two decades for experiments mainly in atomic and molecular physics. It is being modified to fit in its new role as an antiproton and ion decelerator, and it will then be disassembled and put in boxes for transport to FAIR. Reassembly will take place as soon as the FLAIR building becomes available.

The CRYRING project was initiated at the then Research Institute of Physics in the early 1980's [3–5], based on technology developed at, e.g., the low-energy antiproton ring LEAR at CERN. At that time, an EBIS (Electron Beam Ion Source) [6, 7] was already being installed at the Institute, and the idea was to connect the EBIS and other ion sources "to a small synchrotron ring for studies of atomic, molecular and nuclear collisions, and in particular for experiments with interacting beams of ions, molecules, electrons and laser photons", quoting the title page of an early study. Major funding of the project, from the Knut and Alice Wallenberg Foundation, started in 1985, the first deuteron beam was stored in the ring in early 1991, and the experimental programme started the following year. The focus of the experimental activities has been on atomic and molecular physics, with some contributions of applied physics. Also accelerator physics has been pursued, and the machine has been developed and improved continuously.

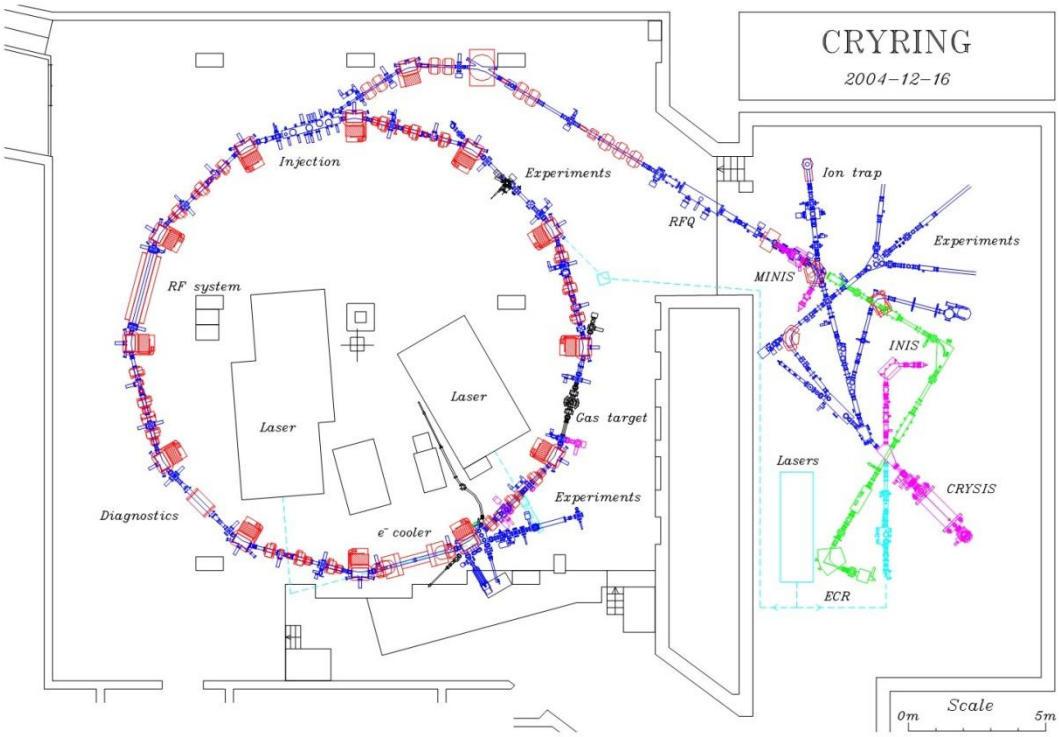

Fig. 2.2. Layout of the CRYRING facility at the Manne Siegbahn Laboratory from 2004 when all injectors were still in place.

The CRYRING project included the ring and three different injectors: the EBIS source, an ECR (Electron Cyclotron Resonance) ion source [8], and a platform for small sources of singly charged ions. Experiments have been performed both at low-energy beamlines directly after the ion sources, and with accelerated beams stored in the ring. Low-energy experiments have included precision mass measurements, atomic collisions and surface physics while the programme of atomic and molecular physics in the ring has had three cornerstones: electron–ion recombination in the electron cooler, fast ions–atom collisions in a gas-jet target and laser spectroscopy of, mainly, forbidden atomic transitions. Highlights of accelerator physics and the machine development have been the introduction of an electron cooler/electron target with a very cold electron beam, down to one or a few meV energy spread, and the study of ordered ion beams. A list of publications from the CRYRING facility over the period 1992–2010, with close to 400 references to publications in peer-reviewed journals plus 43 doctoral dissertations and 39 licentiate dissertations, has been compiled [9].

The layout of CRYRING, such as it looked in 2004 when all three injectors were still in operation is shown in fig. 2.2. Since then, the EBIS source CRYSIS has been decommissioned, and some of the beamlines for low-energy experiments (in the hall to the left in the figure) have been dismantled. The experimental programme at the ring stopped at the end of 2009, and after successful tests of slow extraction during the spring of 2010, the ring is no longer in operation although it is still intact, waiting for disassembly.

A photograph of the ring from 2003, as viewed from the bottom of fig. 2.2, is shown in fig. 2.3. The ring looks essentially the same today, except that a large helium storage balloon prevents a similar picture from being taken again.

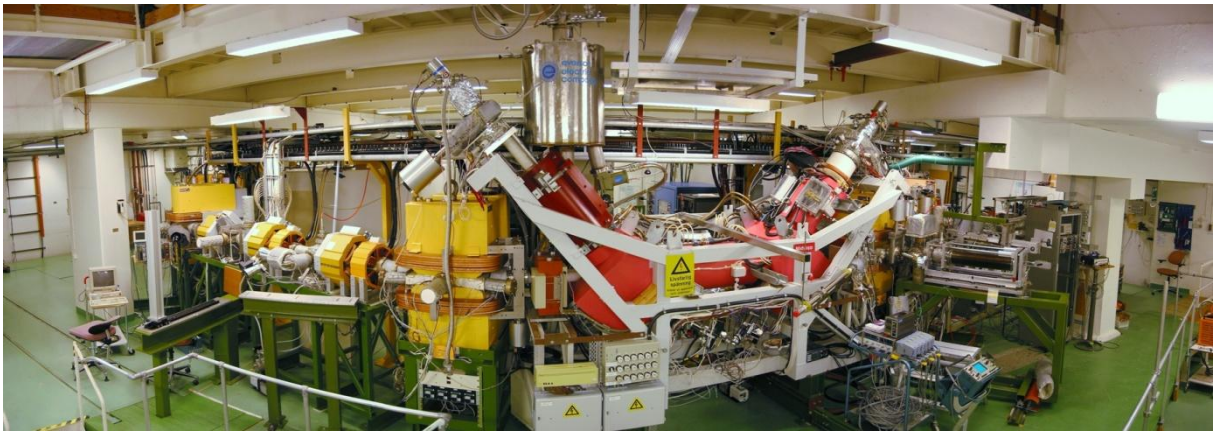

Fig. 2.3. Photograph, with a fish-eye-like perspective, of the CRYRING synchrotron and storage ring from 2003. In yellow are dipole, quadrupole and sextupole magnets while the electron cooler is in red.

2.3. From CRYRING to the LSR

This report describes CRYRING such as it looks today, discusses modifications that have to be made in order for the ring to fit in its new role as an antiproton and ion decelerator, and presents estimates of expected performance of the new LSR. It is shown that CRYRING is well suited to its new task, and that the modifications that have to be made are dominated by the replacement of the injection so that particles can be injected at higher energy and by the addition of a beam extraction. Today, injection is, clearly, made near the minimum rigidity of the ring, and the existing multiturn injection is neither fast enough nor capable to accept a beam with the energy of that coming from the NESR. Beam extraction has never been implemented at CRYRING (except for recent tests of slow extraction), although it was foreseen in the original design, where nuclear physics at an extracted beamline was planned for. Because of this planning, essentially no existing components need to be modified in order to accommodate a beam extraction; it is sufficient to add new equipment at positions that easily can be made available.

Apart from the injection and the extraction, CRYRING already has all the major features needed at FLAIR. It has the right energy range, very good vacuum, efficient electron cooling and a fast ramping which ensures a high throughput of particles. It is regularly switching between positive and negative ions, and it has been in operation for user experiments both in acceleration and deceleration modes. These properties have made it possible to demonstrate that the ring, already as it is configured today, is capable of decelerating protons through the full energy range relevant for FLAIR, with cycle times around 5 s, and with beam intensities approaching the space-charge limit.

An important complement to the LSR ring itself will be its low-energy injector. At CRYRING today, singly charged atomic and molecular ions are injected from a small 50-kV platform where different types of ion sources can be installed depending on user requirements. A similar injector will be installed at FLAIR, using components from the present injector, but with a layout that must be modified according to the geometry of the FLAIR hall and the space available there. Here, ion sources for protons or H^- ions can be installed, allowing the LSR and the beamlines in the FLAIR building to be commissioned without the need to wait for antiprotons from NESR. If desirable, also the USR and

some aspects of the experiments in the FLAIR building can be commissioned with particles from this injector.

The low-energy injector can be used not only during the start-up phase, but also for developments during the operations phase, for training of operators and other staff, etc., during periods when the NESR or other components of the FAIR facility are not available for the production of beams to FLAIR. There are furthermore plans to add a platform with an ECR ion source next to the proton/H^- source, injecting through the same beamline, for development and commissioning also of atomic-physics experiments. Such a source is, however, not part of the present project of transferring CRYRING to FLAIR. Although the components of the present injector beamline will be transferred along with the ring, the design of the new injector beamline is also not part of the project since the final layout of the FLAIR building is not yet known, and the same is true for the connection to the beamline from the NESR ring.

2.4. The Commitment of the Manne Siegbahn Laboratory

During 2009 and 2010, hardware for resonant extraction has been installed and tested, kicker magnets have been designed and ordered, and further modifications and hardware acquisitions will be made during 2010 and 2011. The ring will then be disassembled and put in boxes during 2011 according to current plans. The boxes should be transferred to GSI or to a warehouse near GSI where they will kept until the FLAIR building is ready.

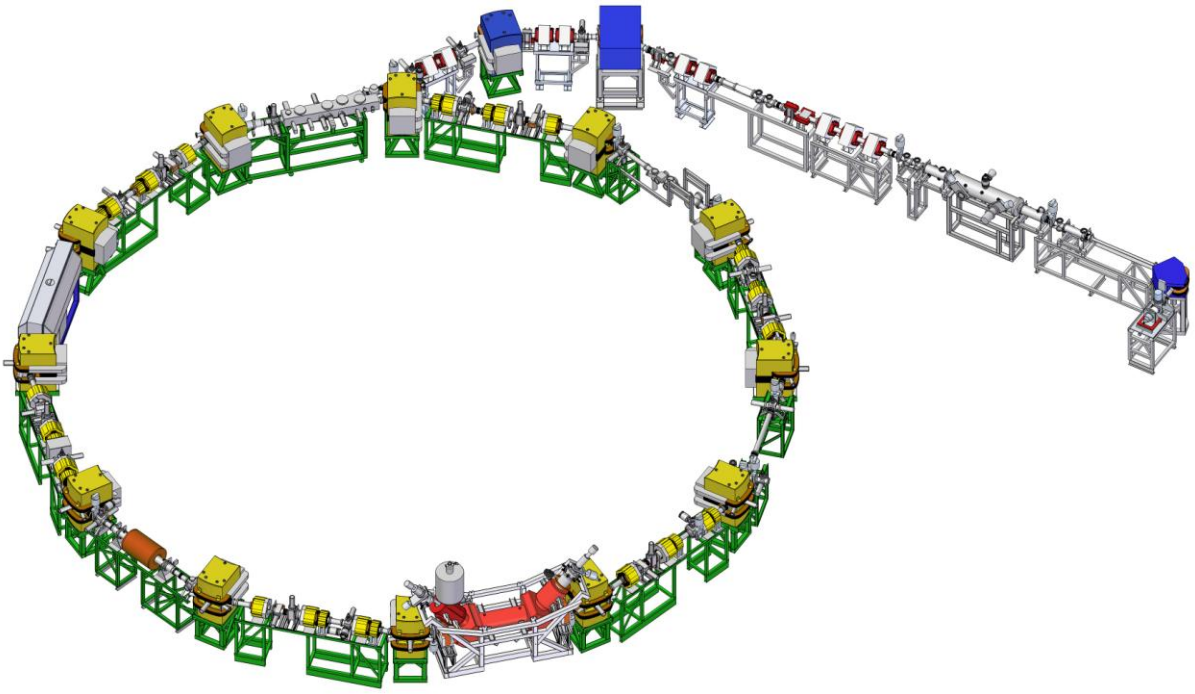

Fig. 2.4. CAD model of CRYRING in its present configuration at MSL.

The commitment of the Manne Siegbahn Laboratory, defining the Swedish in-kind contribution of CRYRING, includes design and acquisition of new hardware, modifications of existing hardware, operations costs for hardware tests, disassembly of the ring and the transport to Darmstadt. It also

includes a thorough documentation of all hardware. At the time when CRYRING was designed, mechanical drawings were made either on paper or with AutoCAD, and these drawings have subsequently been modified as new components have been added to the ring. A substantial effort has now been made in transferring these 2d drawings to a modern 3d format with SolidEdge, and at the same time it has been ensured that the drawings are up-to-date and correspond to what is delivered to FAIR. Fig. 2.4 shows a complete 3d model of CRYRING including those parts of the injector which will be transferred to FLAIR. When the ring is reassembled at FLAIR, the straight sections must be rearranged to fit the geometry of the FLAIR building with its incoming and outgoing beamlines. This modified ring layout is shown in fig. 4.1 and also on the cover of this report.

The reassembly of the ring at FLAIR and all subsequent operations will have to be the responsibility of FLAIR, FAIR or any other body, but MSL will give advice during the reassembly and assist to the best of its ability so that LSR can come into operation as smoothly as possible. The formal offer from MSL to the FLAIR collaboration is reproduced in Appendix 1. When this offer was made, it was anticipated that the reassembly of the ring could take place in 2012–2013. Now, it seems that it will take another perhaps five years before the ring can be reassembled, and it is thus hardly meaningful to now purchase any new equipment that ages significantly on a timescale of 5–10 years. This is discussed in Appendix 2.

3. Properties and Components of CRYRING

3.1. General

Some general parameters of CRYRING in its current configuration are listed in table 3.1 [10] (in the following we will often refer to the ring itself as CRYRING, although this name originally was given to the entire facility, including ion sources and other equipment). The ring has twelve straight sections separated by twelve dipole magnets. Every other straight section has quadrupole and sextupole magnets for focusing of the beam, and also horizontal and vertical correction dipole magnets for adjusting the position of the closed orbit. The sections in between have no such magnetic elements because of the original intention to perform merged-beam experiments at CRYRING, one beam being stored in the ring and the other beam coming from a separate ion source. The superperiodicity of the ring is 6 since all pairs of magnet/magnet-free straight sections are beam-optically equal. In this report, a superperiod is defined to start at the centre of one magnet-free straight section and ends at the centre of the next. The lattice functions are then symmetric around the midpoint of the superperiod. (This is different from the labelling scheme of the control parameters, where devices located in one entire magnet-free section and the following magnet section are given the same superperiod index.)

Circumference	51.63	m
Superperiodicity	6	
Dipole bending radius	1.2	m
Length of magnet sections	3.85	m
Length of magnet-free sections	3.50	m
Rigidity	0.054–1.44	Tm
Energy for protons	0.14–96	MeV
Injection energy from RFQ	300	keV

Table 3.1. General parameters of CRYRING in its present configuration.

The circumference of the ring is calculated as 2π times the dipole bending radius plus the length of the straight sections, as given in the table 3.1. The more detailed geometry of the magnet straight sections is shown in fig. 3.1, with nominal values for the length of the magnets and the drift spaces between them (transverse dimensions are not to scale).

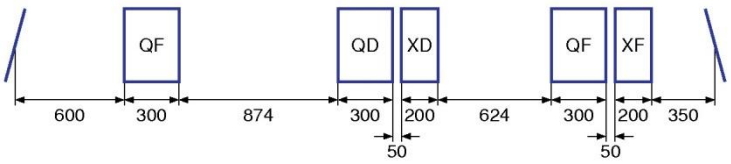

Fig. 3.1. Geometry of magnet straight section, between edges of dipole magnets, with dimensions in mm. QF = focusing quadrupole, QD = defocusing quadrupole, XF = focusing sextupole, XD = defocusing sextupole.

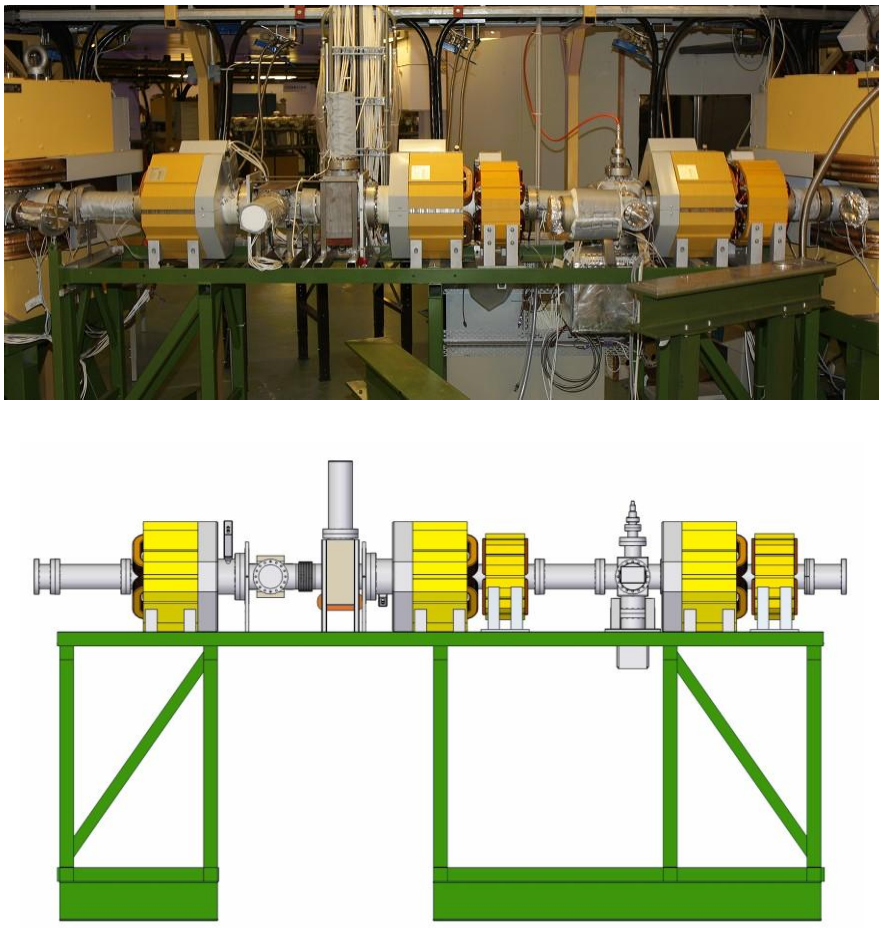

Fig. 3.2. Photograph and CAD model of a magnet straight section, with a horizontal and a vertical correction dipole between the left and middle quadrupole magnets and electrostatic pickups inside the left and middle quadrupoles.

Today, the six magnet-free straight sections are used for 1) Injection, 2) Acceleration, 3) Schottky-noise detection and a compensation solenoid for the electron cooler, 4) Electron cooling, 5) Experiments, mainly with a gas-jet target, and 6) Experiments, mainly collinear laser spectroscopy. Diagnostic elements, such as Faraday cups, electrostatic pickups, current transformers and beam position monitors are distributed among both magnet sections and magnet-free sections.

One of the present experimental straight sections will be used for beam extraction at FAIR, and the position of the injection will be changed in order to match the layout of the FLAIR building. Generally speaking, the magnet-free sections are interchangeable, and their order can be optimized according to the detailed layout of the building.

The maximum rigidity of the ring is 1.44 Tm, as given by the dipole magnets with 1.2 m bending radius and 1.2 T nominal maximum rigidity. The minimum rigidity is given by lowest current in the dipole power converters, as mentioned in section 3.13, to 0.054 Tm. However, the remanence and hysteresis in the magnets become noticeable below 0.079 Tm which is the rigidity for injection of protons from the RFQ. The limits for injection are further discussed in section 5.1.

3.2. Low-Energy Injector

Three different injectors have been in operation at CRYRING: the cryogenic EBIS (Electron Beam Ion Source) CRYSIS for very highly charged ions, an ECR (Electron Cyclotron Resonance) ion source for ions in medium-high charge states, and a 50-kV platform MINIS where different sources of positive or negative atomic or molecular ions—with few exceptions singly charged—can be installed. Only the 50-kV platform will be discussed in this report, since a modified version of it will be transferred to FLAIR together with the ring.

Ions from the 50-kV platform are injected into an RFQ (Radio Frequency Quadrupole), which is a linear accelerator with a fixed input velocity corresponding to an energy per nucleon equal to 10 keV/u and with a fixed output velocity corresponding to 300 keV/u. The RFQ can accelerate particles that have a charge-to-mass ratio q/A above 0.25, thus including protons, antiprotons and ions in sufficiently high charge states. Particles with q/A below 0.25 can be transported through the RFQ without acceleration. In this case only a small RF voltage is applied in the RFQ, resulting in a certain amount of focusing of the particles. The beamline connecting the ion source and the RFQ to the ring has a number of magnetic and electrostatic optical elements, as well as vacuum equipment and diagnostics which will be included in the transfer to FAIR, but only the components of this beamline, not the layout at MSL will be described, since the layout of the injection line will be different in the FLAIR hall.

3.3. Ion Source Platform

The 50-kV MINIS platform is shown in fig. 3.3. It has a flat flange with 80 mm I.D. at the end of a solenoid magnet into which ion sources of different types can be installed. At MSL, the most commonly used ion source for singly charged positive ions produced from gases or liquids is a Nielsen-type source with a hot filament in a cylindrical discharge chamber, immersed in the magnetic field from the solenoid. To this source an oven can be added for production of ions from solid substances. The oven can be used at temperatures between 300 and 800 °C. Also commonly used is a cold-cathode source using a glow discharge for ion production. The cold-cathode source has some advantages in that it normally produces molecular ions in lower vibrational states, and it is also useful for ions containing carbon atoms which tend to produce soot in the hot Nielsen source. Other types of ion sources that have been used for more specialized purposes include a cesium sputter ion source for negative ions and an expansion source where a short pulse of gas at relatively high pressure is released through a piezo-electric valve. This source produces molecular ions that are rotationally cold. More than 100 different ion species have been produced at this platform for use in CRYRING.

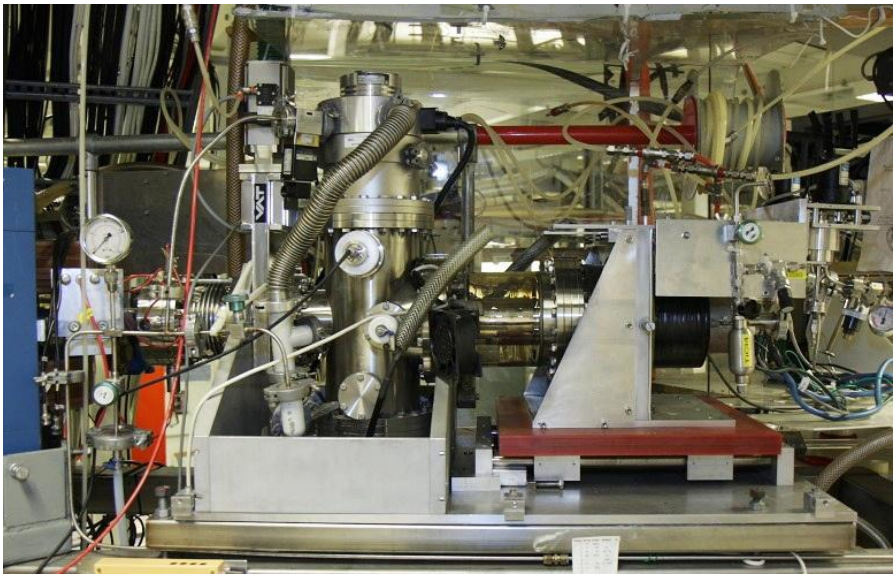

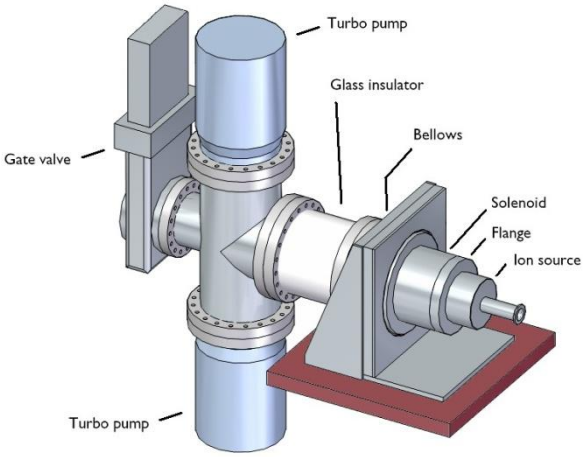

Fig. 3.3. Photograph of the 50-kV MINIS ion-source platform and schematic model of the setup between source and gate valve. The corner of the blue analyzing magnet is seen to the far left in the photo.

Although H^- ions have been produced both with the Nielsen source and with the cesium sputter ion source, none of these is ideal for use at FLAIR. Instead, MSL has a duoplasmatron source on loan from Brookhaven National Laboratories for evaluation, and this source or a similar one will be included in the transfer to FLAIR.

On the high-voltage platform there is a 40 A, 35 V supply for heating of filaments. There are also two 300 V, 2 A supplies that are used for the anode and the solenoid in the case of the Nielsen-type source. A 3 kV, 10 mA supply is used for the cathode of the cold cathode source. These supplies can also serve other purposes, depending on the kind of ion source used. For gas handling, there are two separate remote controlled needle valves that can be used for mixing gases in the ion source. This is often used to produce the desired ions for different experiments. The high-voltage platform is separated from earth potential by an 11 cm long glass insulator. Inside and downstream from the insulator, there is an einzel lens which is used to place the image of the source outlet at the focal point

of the double focusing magnet that is used for mass separation further downstream. The magnet has a bending radius of 0.5 m and gives a resolution of about 500. Vacuum pumping is done from earth potential where two turbo pumps are connected. With the help of a baffle, some differential pumping is achieved such that one of the pumps is mainly pumping upstream, on the higher gas load from the source, and the other downstream. Further downstream the beamline, close to the focal point of the analyzing magnet, there is a conductance limiter in the shape of a 100 mm long tube, 10 mm in diameter. A Faraday cup is placed right after this tube and the tube is designed not to scrape off any part of the desired beam, if the einzel lens is adjusted properly. To aid in finding the beams of different masses, there is also a fluorescent screen before the tube. On this screen several masses can be seen at the same time and a coarse adjustment can be made so the ions of the desired mass can be found in the Faraday cup. For heavy ions, beams with intensities down to a few nA can be seen on the fluorescent screen, while in the Faraday cup beams well below 1 pA have been detected.

3.4. Radio Frequency Quadrupole

The RFQ is designed to accelerate ions with a charge-to-mass ratio, q/A, which is larger than or equal to 1/4 from the nominal input energy of 10 keV/u to an output energy of 300 keV/u. In this mode a transmission of around 90% can normally be achieved. It is of the four-rod type and was constructed and built in collaboration with A. Schempp at the University of Frankfurt [11]. The main advantages of a four-rod RFQ are the relative ease of manufacturing and the inherent suppression of the dipole mode. The RFQ is resonant at 108.48 MHz and is powered by a custom-built RF transmitter capable of delivering up to 70 kW pulses of less than 0.5 ms length at full power or longer pulses at reduced power levels. The transmitter is mainly based on commercial units from ITELCO, such as a solid-state 500 W amplifier, two parallel intermediate-stage amplifiers with glass tubes and two final-stage amplifiers with two EIMAC 4CX12000A tetrodes. The lifetime of the final-stage tubes has been around 15 000 hours. A 3-dB coupler splits the input signal into two equal parts that are fed to each of the two tubes that are working in parallel. The output signals from the two tubes are coupled together in another 3-dB coupler which also protects the amplifiers by coupling any reflected power to a water cooled dummy load. A schematic diagram of the amplifier is shown in fig. 3.5, where the intermediate stages have been eliminated and a 2-kW solid-state amplifier is used instead as suggested in section 4.3. A separate amplifier, capable of driving the 2 kW stage has been omitted in the figure. It is estimated that a 15 W amplifier would be needed.

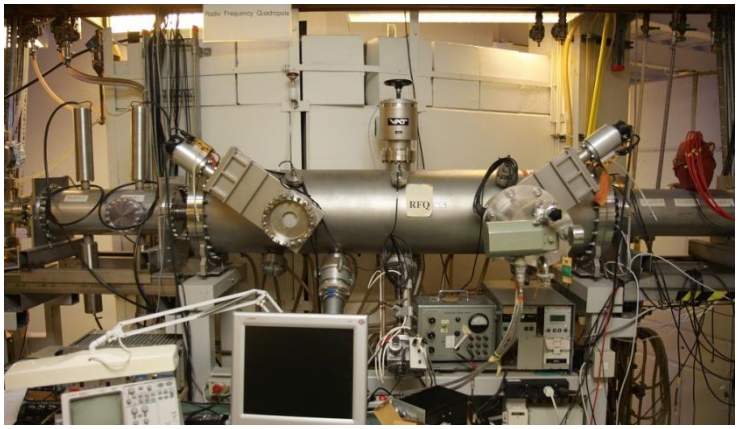

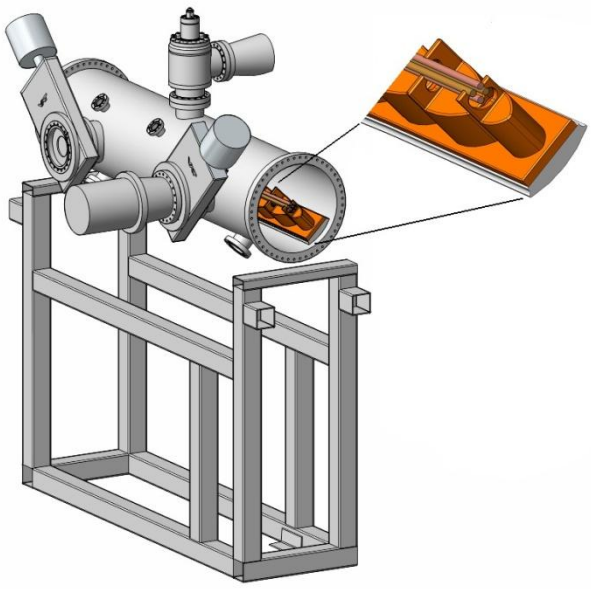

Fig. 3.4. Photograph and CAD model of radio frequency quadrupole.

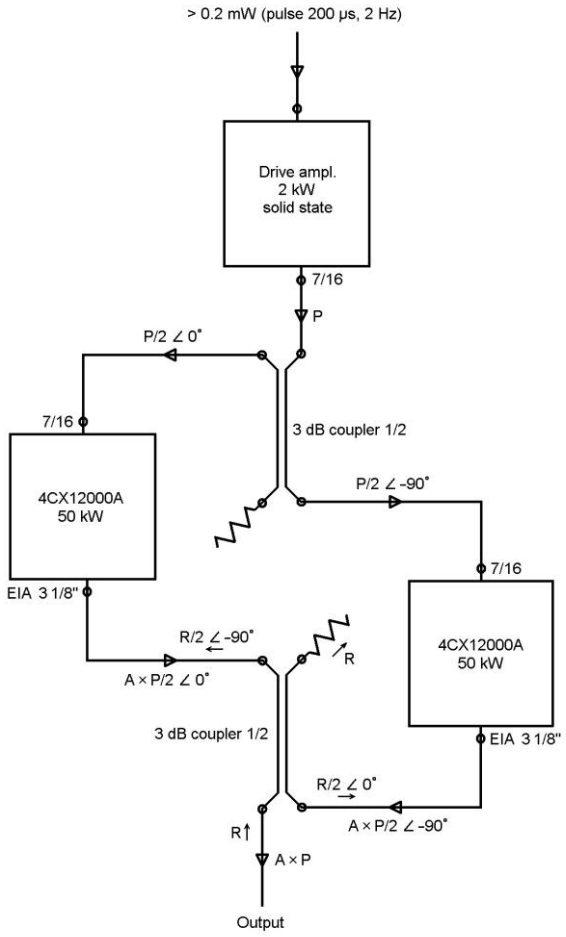

Fig. 3.5. Schematic diagram of the final stages of the RFQ amplifier.

The low-level electronics was custom built for this application by the German company IWB in Frankfurt. It contains a crystal oscillator as a stable source for the RF at 108.48 MHz as well as control loops to stabilize the amplitude and the phase of the RF signal. The pulse width is set by an external TTL gate signal which is supplied to the amplitude control module. There is also control electronics to keep the RFQ on resonance with the RF frequency. The resonance frequency of the RFQ is adjusted with the help of a mechanical tuner which is moved by a motor from the outside. This tuner can change the resonance frequency of the RFQ structure by around 200 kHz. This range is sufficient to compensate for the increased temperature of the structure at the higher RF peak powers that have to be applied for the lower charge-to-mass ratios, but it sets a maximum limit on the average power that can be used on the RF. The RFQ structure is cooled by cooling water entering the stems of the structure from below and exiting coaxially. This cooling is not very efficient and the maximum average power that can be applied before the tuner reaches its innermost position is only around 100 W. Thus there is a limit on the maximum permitted pulse lengths for different RF amplitudes. Naturally, there is also a limit to the maximum RF power that can be applied before sparking starts to occur in the RFQ structure. It is this limit of the maximum useable RF power that gives the lowest value of q/A that can be accelerated. To be able to use the highest RF power levels, normally some time for conditioning has been needed. The RF power needed to accelerate deuterons, with q/A=1/2, is around 12 kW. This value can be scaled to find the proper level need for different ion species, since the power is proportional q^2/A^2. To be able to obtain the highest RF powers, above 30 kW, the tetrode tubes in the final stages of the amplifier need to be run with increased anode voltages, above the specified maximum 10 kV, but no failures of the tubes have occurred due to the use of these over-voltages. To reach these voltages, the connection to the high-voltage transformer needs to be changed from Δ to Y coupling which is done remotely. This connection can be remotely changed as long as there is no voltage on the transformer. There is also a possibility to adjust the anode voltage by changing between different taps on the transformer. Taps giving –20%, –10%, 0% and +5% voltages are available. The changing between different taps has to be performed manually. With the transformer in Δ mode the anode voltage is around 7 kV and in Y mode around 11 kV. Very long RF pulses have been used to increase the intensity of the light from the fluorescent screens in the beamline after the RFQ for cases of very week beams of heavy, singly charged ions. For shorter times, at most a few minutes, RF pulses up to 10 ms with repetition rates around 1 Hz have been used. In normal use, the pulse width is set to be longer than the injection time in the ring by at least 200 μs to allow the amplitude of the RF to become constant after an initial overshoot that is created by the amplitude feedback electronics.

The control unit that keeps the RFQ in resonance performs this by keeping the phase difference of the input RF signal and the signal in the RFQ structure itself, as given by a small pickup electrode placed on the wall of the vacuum chamber, constant at a given value. This value needs to be manually adjusted by changing a potentiometer on the control unit. The correct position of this potentiometer is mostly found by adjusting it to the position of the tuner that gives the highest amplitude in the RFQ, again measured by an RF pickup electrode. In fig. 3.6, a drawing of the low-level electronics is given.

Due to the large interest to make experiments with heavy, singly charged ions in the ring, a transporting mode through the RFQ has been developed. In this mode the RFQ is used as a focusing channel for ions with charge-to-mass ratios that are too low for acceleration. A suitable level of the RF amplitude, much below what would be needed to accelerate these ions, has to be found for each ion species. Usually, transmissions well above 50% can be reached in this mode, often even close to 100%. This mode has been used for particles with q/A from 1/4 (He^+) down to 1/119 ($POCl_2^+$). In fact, He^+ has been stored in the ring both accelerated in the RFQ and just transported through.

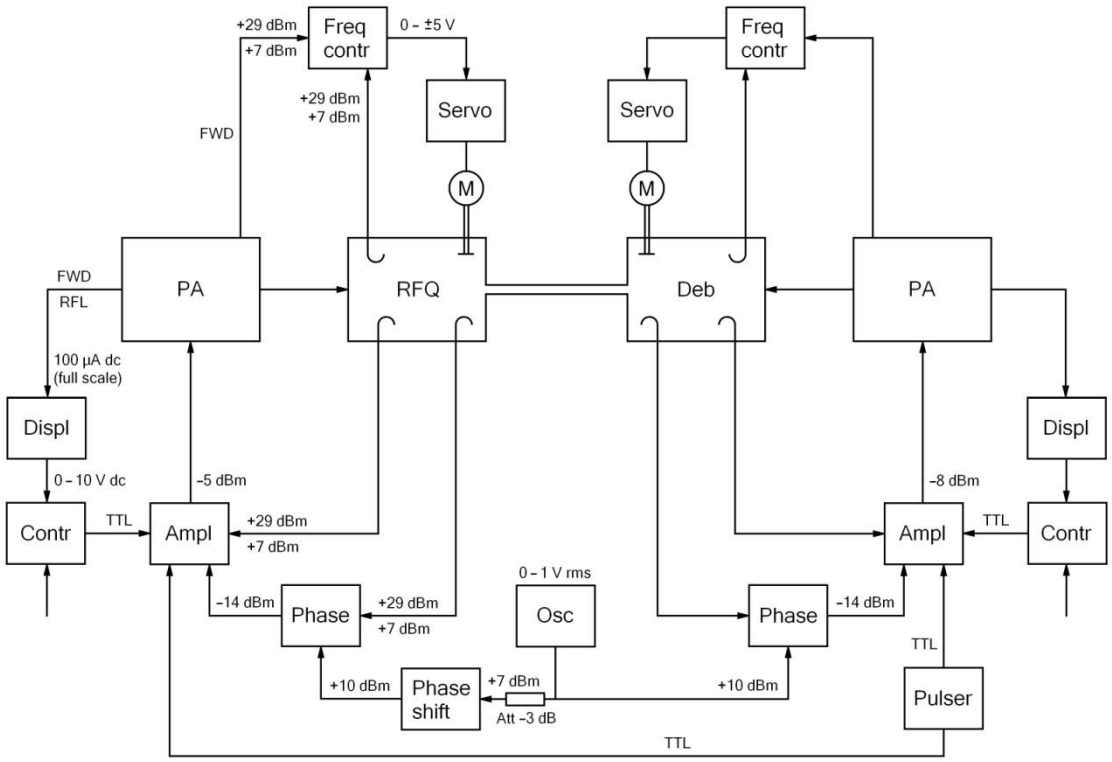

Fig. 3.6. Schematic of low-level RFQ and debuncher electronics.

Originally, it was planned that a debuncher should be placed after the RFQ with the purpose to reduce the momentum spread of the 108.48 MHz bunches coming from the RFQ from a calculated ±1% to ±0.5% or somewhat lower. The debuncher was built and installed in the beamline, but due to lack of time and some problems during the commissioning of the debuncher, it was never actually used. It is built as a spiral-loaded two-gap cavity, resonant at the same frequency as the RFQ, 108.48 MHz. The control electronics, similar to that of the RFQ, plus a unit to control the phase difference between the RF signals to the RFQ and the debuncher has also been built, c.f. fig. 3.6. This equipment will be delivered with the RFQ and it is believed that with a limited amount of work from a person with experience in RF and accelerator cavities, it should be possible to make the debuncher useful. Note, however, there is no RF amplifier available for the debuncher, so this equipment has to be acquired/built before it can be used. A 500 W amplifier should be sufficient. The debuncher could make the multi-turn injection more efficient for ions that are accelerated in the RFQ and thus increase the ion current that is stored in the ring, but, without testing this, it is difficult to estimate how large intensity increase could be achieved.

3.5. Injector Beamline

We here describe the injector beamline, from the ion source, via the RFQ, to the ring. Although the layout of the beamline from the low-energy injector at FLAIR will be different from the layout at

CRYRING today, this description is meant to give an impression of how the components from the present beamline can be used for the new one at FLAIR.

The beamline is divided into four sections, which according to the terminology used at CRYRING are referred to as L1, C1, R1a and R1b, see fig. 3.7. The sections have gate valves at both ends, and they can be pumped down separately by permanently installed turbo-molecular pumps (in L1 and C1) or by mobile pump-down stations that can be connected through angle valves (in R1a and R1b). L1 is approximately 2 m long, starts from the acceleration gap after the ion source platform, continues through a 90-degree analyzing magnet, and ends where ions from the ECR beamline are inflected from above through a vertical dipole magnet and ions from CRYSIS are inflected from below. If one chooses to keep a similar geometry at FLAIR, and if an ECR ion source will be added to the low-energy injector, a horizontal dipole magnet could replace this vertical dipole for inflection of the beam from such an ECR source. C1 is the beamline from CRYSIS to the RFQ, and the distance from the ECR/CRYSIS inflection magnet to the RFQ is also about 2 m. The R1a section extends from the RFQ and 9 m downstream, and from there R1b continues for a distance of 4.5 m to the injection into the ring. The entire beamline, from ion source to injection into the ring, is built with CF flanges, although other types of flanges very well could be used instead in the early parts where the vacuum requirements are less stringent. The R1b beamline is built according to full UHV standards, with all-metal valves, careful choice of materials, cleanliness, bakeablility etc.

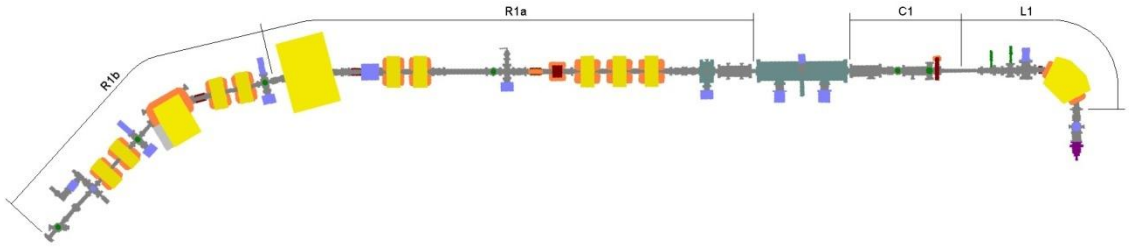

Fig. 3.7. Layout of the present injection beamline of CRYRING.

The vacuum pressure close to the ion source depends on the type of ion source used and on the particular running conditions of the source, but it is typically 10^{-4}–10^{-5} mbar. There is one turbo-molecular pump in the L1 section and one in C1, and there is a 10 mm aperture at the end of L1, just before the Faraday cup, improving the differential pumping between the ion source and downstream sections of the beamline. As a result, the pressure at the entrance of the RFQ is normally in the range 10^{-7}–10^{-8} mbar. The RFQ has a turbo-pump and two CF150 flanges, where cryopumps can be mounted. Such pumps were installed and used during the early operation of CRYRING, but have since then been removed and are no longer considered necessary. In the R1a and R1b sections, after the RFQ, only ion pumps and NEG (Non-Evaporable Getter) pumps are used in order to make the system less sensitive to power outages or mechanical failures of turbo-molecular pumps. A 10 mm aperture after the electrostatic quadrupole doublet after the RFQ improves the differential pumping between R1a and R1b. The R1b section is the only bakeable part of the injection line, and it is regularly baked out to 300 °C after opening to air. The pressure in R1a is lower than 1×10^{-8} mbar during normal operation, and at the end of R1b it has come down to the same level as in the ring, i.e. better than 1×10^{-11} mbar.

Element	ID	Aperture (mm)	Radius (m)	Angle (deg.)	Field/field integral (T/ Tm/ MVm^{-1})	Current/ voltage (A/kV)	Settings for He^+ (A/kV)
Analyzing magnet	L1BHM1	40	0.5	90	1.0	240	26
Vert. steering magnet	L1DVM1	155			0.005	5	< 0.2
Hor. steering plates	L1DHE1					±0.4	< ±0.4
Vert. steering plates	L1DVE2					±0.4	< ±0.4
Vert. bending magnet	C1BVM3	50		0	1.2	185	< 1
Hor. steering magnet	C1DHM5	220			0.003	5	< 1
El. quadrupole doublet	C1QDE3	80			0.3	2	0.9/1.0
El. quadrupole triplet	C1QTE4	80			1.1/1.5/1.9	6/8/10	1.8/3.6/4.8
El. quadrupole triplet	R0QFE/QDE	40			18/26	35	27/21
Magn. q-pole triplet	R1QM1	100			3.6	200	25/42/31
Hor. steering magnet	R1DHM1	100			0.01	3	< 0.5
Vert. steering magnet	R1DVM1	100			0.01	3	< 0.5
Magn. q-pole doublet	R1QM2	100			3.6	200	35/29
Vert. steering magnet	R1DVM2	100			0.01	3	< 0.5
Bending magnet	R1BHM1	70	0.725	28.9	1.6	370	43
Magn. q-pole doublet	R1QM3	100			3.6	200	26/38
Vert. steering magnet	R1DVM3	100			0.01	3	< 0.5
Bending magnet	R1BHM2	80	1.013	35	1.58	600	88
Magn. q-pole doublet	R1QM4	100			3.6	200	28/34

Table 3.2. Data for magnets and electrostatic elements in the injection beamline of CRYRING. For bending magnets, gap, bending radius, bending angle and maximum field strength are listed. Steering magnets and electrostatic steering plates, whose nominal bending angle is zero, have gap and field integral (maximum field strength times effective length). Quadrupoles have inscribed diameter, and integrated strength (maximum gradient times effective length, per pole in case of doublets and triplets). Some values are approximate.

The first beam-optical element after the ion-source platform is the 0.5-m-radius, 90-degree, double-focusing analyzing magnet The exit aperture of the ion source is just inside the entrance focal point of this magnet and an einzel lens is used to optimize the focusing into the magnet. After the magnet, there are a vertical steering magnet and two pairs of electrostatic steering plates, one for vertical and one for horizontal correction. Each of these steering plates is equipped with a +800 V voltage supply. With the two magnets and the two electrostatic plates, the initial beam position and angle can be controlled both horizontally and vertically. Then the beam passes through the ECR/CRYSIS inflection magnet where the ECR beam is comes in at a 20-degree angle from above and the CRYRIS beam at a 45-degree angle from below. When the beam comes from INIS, this magnet is just another vertical steering. Just downstream from the inflection magnet there is another steering magnet for horizontal corrections and before coming to the RFQ there is an electrostatic quadrupole doublet and a triplet close to the RFQ, providing a rather tight focus onto the entrance of the RFQ. The part of the beamline between the last quadrupole and the RFQ is designed with special care to allow the quadrupole to be mounted as close to the RFQ as possible, to be able to fulfil the requirements on the shape of the injected beam.

Just after the RFQ there is an electrostatic quadrupole triplet with the outer electrodes connected to the same voltage supply. All following elements of the injection beamline are magnetic. These are one

quadrupole triplet, three doublets, two bending dipoles and four steering dipoles. Except for one bending dipole, all these magnets (in the case of the steering magnets only the coils) are recovered from the 225-cm cyclotron that preceded CRYRING as the main instrument for accelerator-based research at the then insitute. The coils are still in relatively good condition and there is no obvious reason why these magnets could not be reused once more for the injector beamline at FLAIR, in particular since they are, with the present layout, not running at more than a fraction of their design fields. The only magnet that is not recovered from the cyclotron is one of the bending magnets, which is a prototype of a ring dipole magnet although the conductor in the coils is different and the bending angle is 35 instead of 30 degrees. The other bending magnet is a former switching magnet from one of the old cyclotron beamlines, and it is quite heavy and bulky compared to what would actually be required for the present function. It can be used for bending angles up to 45 degrees. Data for the electrostatic and magnetic elements of the injection beamline are listed in table 3.2. All items listed in the table will be included in the transfer to FLAIR.

3.6. Ring Lattice

The basic geometry of the ring is given in table 3.1. The geometry is defined by 30-degree circular arcs with 1.2 m radius at the dipoles, magnet-free straight sections with a length of 3.500 m, and magnet straight sections with a length of 3.848 m according to fig. 3.1. The dipole magnets are of rectangular type and thus provide edge focusing in the vertical plane. There are only two families of quadrupoles. These are arranged as triplets with one defocusing quadrupole at the centre of the magnet straight sections and two focusing quadrupoles symmetrically positioned as seen again in fig. 3.1. All quadrupole magnets are physically identical. A basic MAD file defining the ring lattice is listed in table 3.3

```
TITLE, "CRYRING"
!
QF:QUAD,L=0.3/2,K1=4.4000
QD:QUAD,L=0.3/2,K1=-4.0000
BM:RBEND,L=1.2*PI/6,ANGLE=PI/6,HGAP=0.04,FINT=0.56
SF:SEXT,L=0.2
SD:SEXT,L=0.2
L1:DRIFT,L=3.5/10
L2:DRIFT,L=0.624/2
L3:DRIFT,L=0.05
LS:DRIFT,L=0.2
!
TW(X,Y):LINE=(5*L1,BM,L1,X,L3,2*QF,2*L2,Y,L3,QD)
SIX:LINE=(TW(LS,LS),-TW(SF,SD))
USE,SIX,SUPER=6
!
PRINT,#S/E
TWISS,TAPE
STOP
```

Table 3.3. A MAD input file that defines the lattice of CRYRING.

With only two quadrupole families, the tune diagram can be plotted in two dimensions as seen in fig. 3.8. The left graph shows the area where the particle motion is stable in the two planes simultaneouly as a function of normalized quadrupole gradients, and in the right graph the stable area is plotted as a function of the tunes. The normalized quadrupole gradient is given by $k = B'/B\rho$, the field gradient divided by the magnetic rigidity of the beam, and the nominal quadrupole length of 0.30 m is used (c.f.

section 3.7). A point with a certain k_x and k_y in the left graph and the point with the corresponding values of Q_x and Q_y in the right graph are plotted with the same colour. The black and white gridlines are included just to make it easier to identify points in the two graphs. Note that each point in the region $Q_x < 3$, $Q_y < 3$ corresponds to two points in the left graph. Fig. 3.9 shows a smaller part of the same diagram. Here, resonances up to third order are illustrated with colourless lines, the widths of which represent the resonance strength in a schematic, non-quantative manner. The standard working point of $Q_x = 2.42$, $Q_y = 2.42$, corresponding to $k_x = 1.80$ m^{-2} and $k_y = 2.35$ m^{-2}, is where the colours meet. This working point is found by experience to allow the most stable beams with the highest stored currents.

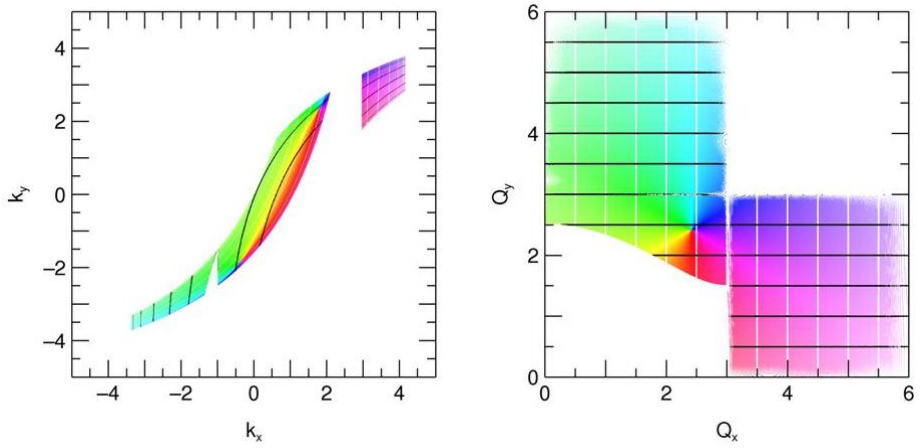

Fig. 3.8. Tune diagram for CRYRING, where the area of stable motion is plotted as a function of quadrupole gradients in m^{-2} in the left graph and as a function of the tunes in the right graph.

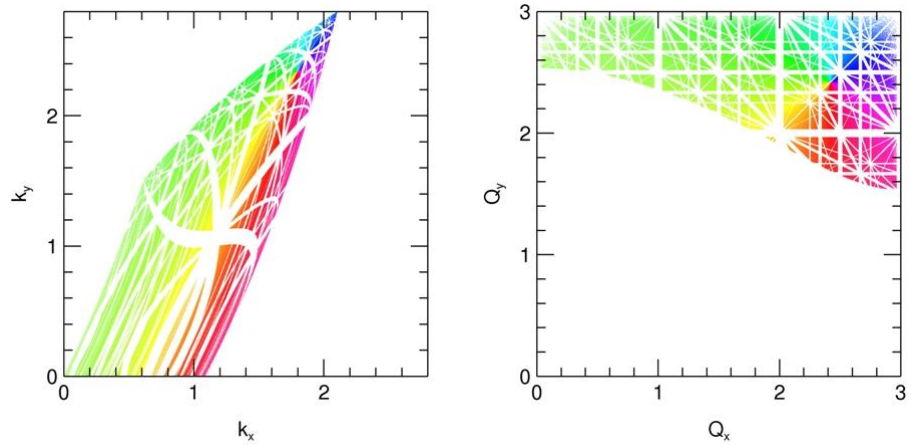

Fig. 3.9. Same tune diagram as in fig. 3.8 but only for positive quadrupole strengths and tunes $Q_x < 3$ and $Q_y < 3$. Resonances are drawn schematically as colourless lines.

There were a number of design considerations behind the CRYRING lattice [12, 13], leading to a quite symmetrical machine with rather smooth beta functions and rather constant dispersion. Beta functions and dispersion in one superperiod, starting at the centre of one magnet-free straight section and ending at the centre of the next one, are plotted in fig. 3.10 for the standard working point of $Q_x = 2.42$, $Q_y = 2.42$ and also for $Q_x = 2.33$, $Q_y = 2.42$ which will be used for the slow extraction. The shaded

areas represent the extent of the dipole and quadrupole magnets, with the dipoles outermost and the quadrupole triplet in the centre. It is seen that the difference between the two working points is very small.

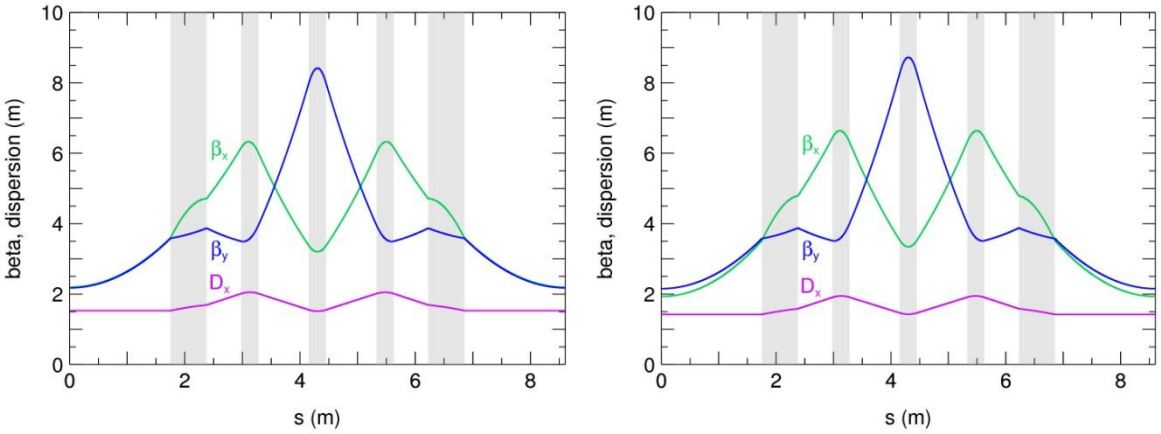

Fig. 3.10. Beta functions and dispersion for Q_x = 2.33, Q_y = 2.42 (left) and Q_x = 2.42, Q_y = 2.42 (right). The shaded areas illustrate the position of dipole and quadrupole magnets (c.f. fig. 3.1).

The lattice is rather flexible, and a number of other working points, fulfilling different requirements, were foreseen in the design of CRYRING. For instance, a solution with lower dispersion can be found at the expense of larger beta functions. It is also possible to obtain zero dispersion on three of the magnet-free straight sections by breaking the sixfold symmetry of the lattice into a threefold symmetry. This requires that the power converter for the focusing quadrupole magnets be split into two separate units. Such a mode of operation has been prepared in the design of the power converter but requires additional controls.

It would furthermore be possible to extend the circumference of CRYRING somewhat without large effects on the beta functions or other properties of the machine. This could be of interest if it would be found that more space is required for, e.g., some component of the new injection or extraction or some in-ring experiment, although no such need is anticipated today.

In all cases, the ring operates below transition gamma, which is 2.33 at Q_x = 2.42 and 2.25 at Q_x = 2.33. This can be compared to the relativistic gamma factor of 96 MeV antiprotons at the maximum rigidity of the ring which is equal to 1.10.

CRYRING has two sextupole magnets on each magnet straight section for chromaticity correction and for driving the 1/3 resonance used for slow extraction. A defocusing sextupole is positioned close to the defocusing quadrupole, and a focusing sextupole is located near the second focusing quadrupole of those sections, as illustrated in fig. 3.1. With these sextupole positions, where the focusing sextupole sits where β_x is large and β_y is small and vice versa, optimum chromaticity control can be obtained in the two planes independently. All twelve sextupoles have individual bipolar power supplies, but they are normally used in two families only.

There are one horizontal and one vertical correction dipole magnet, for adjustment of the closed-orbit position, in each superperiod. These do not have the same position in all superperiods due to lack of space. If more control of the closed-orbit position is found to be required, for instance to fine-tune the extraction, all 12 main dipole magnets are equipped with backleg windings. These are not used at

present, and there are no power supplies for them, except for the two dipoles surrounding the electron cooler (see section 3.11).

In addition to their use for chromaticity control, slow extraction and closed-orbit corrections, sextupoles and correction dipoles are needed at the fast ramping (7 T/s in the main dipoles), in particular at the beginning of the ramp, in order to compensate for the effect of eddy currents in the dipole vacuum chambers. These eddy currents produce fields which have both a dipole component and a sextupole component.

	Dipoles	Quadrupoles	Sextupoles	Correction dipoles[1]
Quantity	12	18	12	12
Bending radius	1.2 m	–	–	–
Bending angle	30 degrees	–	–	–
Nominal length	0.628 m	0.3 m	0.2 m	–
Effective length	0.621 m	0.283 m	0.203 m	0.19 m
Yoke length	0.628 m	0.238 m	0.17 0m	0.120 m
Maximum field	1.2 T	5 T/m	27 T/m^2	0.03 T
Nominal current	1097 A	336 A	10 A	10 A
Resistance	15 mΩ	40 mΩ	1.4 Ω	1.4 Ω
Inductance	22 mH	6 mH	268 mH	271 mH
Aperture (height/diam.)	0.080 m	0.125 m	0.125 m	0.120 m
Number of coils	2	4	6	1
Turns per coil	36	24	180	648
Wire dimension	14.9 × 14.9 mm^2	7.5 × 6 mm^2	1.8 × 4.7 mm^2	1.6 × 3.2 mm^2
Cooling channel diam.	6 mm	3.5 mm	–	–
Water flow	11 l/min	4.5 l/min	–	–
Pressure drop	7 bar	7 bar	–	–
Weight	4 500 kg	250 kg	85 kg	30 kg

Table 3.4. Data for ring magnets. Note that the values listed here in some cases only are nominal, and they should be verified by independent means before current sources with characteristics different from those used at present are connected to the coils. [1]Two of the correction dipoles have larger aperture, see text.

The acceptance of the ring is approximately 200π mm mrad horizontally and 100π mm mrad vertically. The horizontal acceptance is limited by the 100-mm inner diameter of the vacuum pipe in the focusing quadrupole magnets while the vertical acceptance is determined by vacuum chambers in the dipole magnets which have an internal height of 54 mm. The momentum acceptance is approximately ±2% at zero emittance. In [10], the single-particle acceptance is calculated more precisely: At the standard working point of $Q_x = 2.42$, $Q_y = 2.42$, the horizontal beta function in the focusing quadrupoles is 6.6 m. The maximum particle displacement $\hat{x}$ is taken as 40 mm, obtained from the 50 mm inside radius of the quadrupole vacuum chamber minus 10 mm to allow for magnet and alignment errors. The resulting acceptance is calculated from

$$\hat{x} = \left[\beta_x \varepsilon_x + \left(D_x \Delta p / p\right)^2\right]^{1/2},$$

which, at zero momentum spread, results in a horizontal acceptance of 254 π mm mrad. Similarly, the vertical beta function in the dipole magnets is 3.9 m, and subtracting 5 mm from half the internal height of 27 mm a vertical single-particle acceptance of 124 π mm mrad is obtained.

3.7. Ring Magnets

The main ring magnets are 12 dipoles, 18 quadrupoles (12 focusing, 6 defocusing) and 12 sextupoles (6 focusing, 6 defocusing), all of them delivered by Danfysik A/S. They are all laminated. Each one is made in a single piece, implying that the quadrupoles and sextupoles cannot be split open for insertion of the beam pipe. Instead, the beam pipe at one end has a flange that can be split in two halves and removed before the pipe is inserted axially into these magnets. The main characteristics of the ring magnets are listed in table 3.4.

The main dipoles, see fig. 3.11, are of rectangular type. Their aperture is 80 mm, although Rose shims, extending the width of the good-field region, reduce the aperture to 78 mm at the inner and outer edges of the pole surfaces. The magnetic field strength in the centre of the dipoles and its derivative with respect to excitation current are shown as a function of current in fig. 3.12.

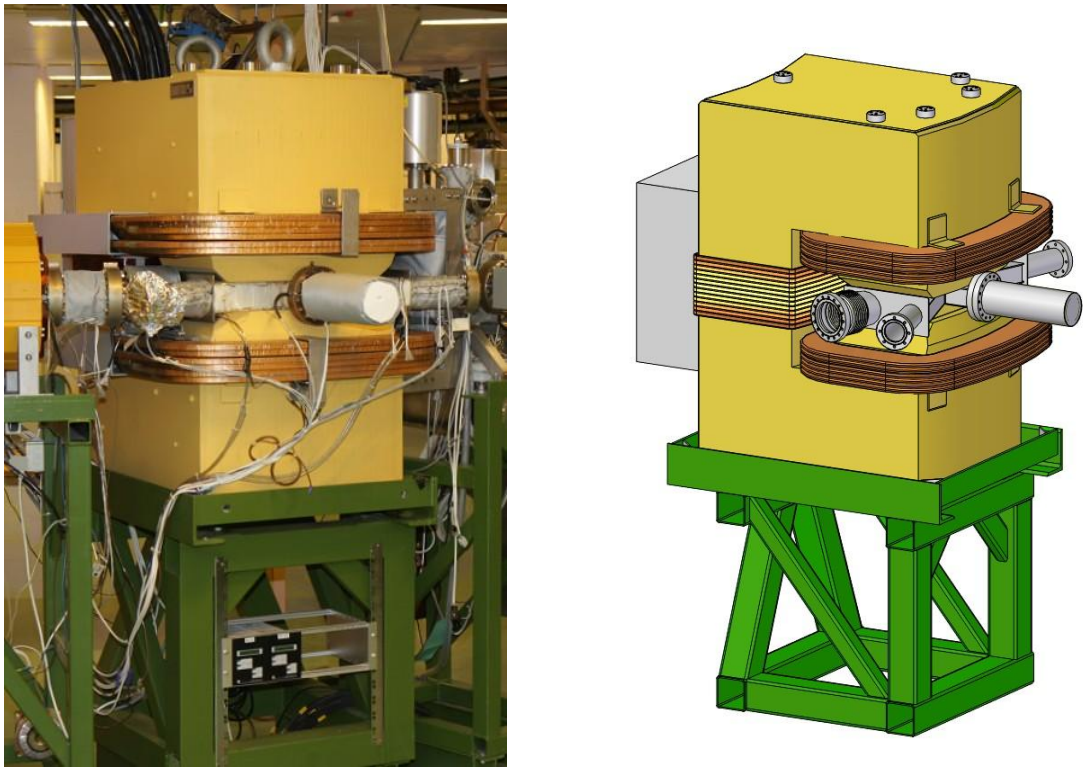

Fig. 3.11. Photograph and CAD model of a ring dipole magnet with support frame. Included in the CAD model are main coils, backleg winding, connection box at the back, alignment targets on top and vacuum chamber.

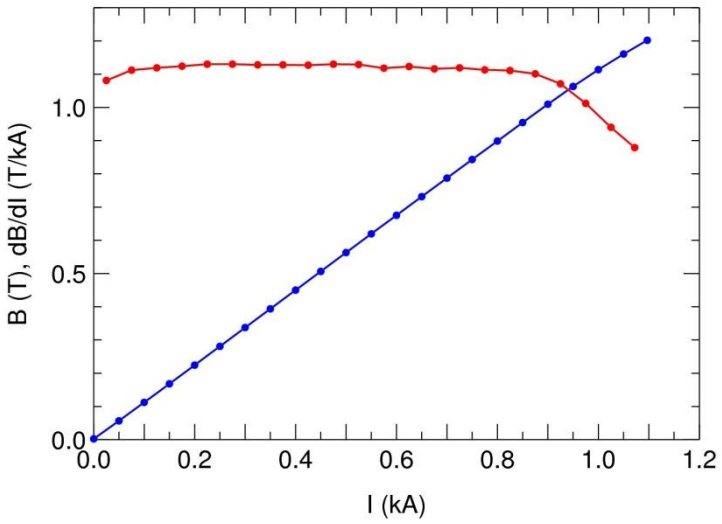

Fig. 3.12. Magnetic field strength in the dipole magnets as a function of excitation current (blue) and the derivative of the field with respect to the current (red). Data are taken from magnet measurements made by the manufacturer prior to delivery.

Fig. 3.13 shows the geometry of one quadrant of the quadrupole laminations with poles that have hyperbolic shape except for a straight contour toward the sides of the poles (largest *x* or *y*). Field lines are obtained from a two-dimensional Poisson calculation. The coil dimension is only approximate. In fig. 3.14, a photograph and CAD models of a quadrupole and a sextupole are shown.

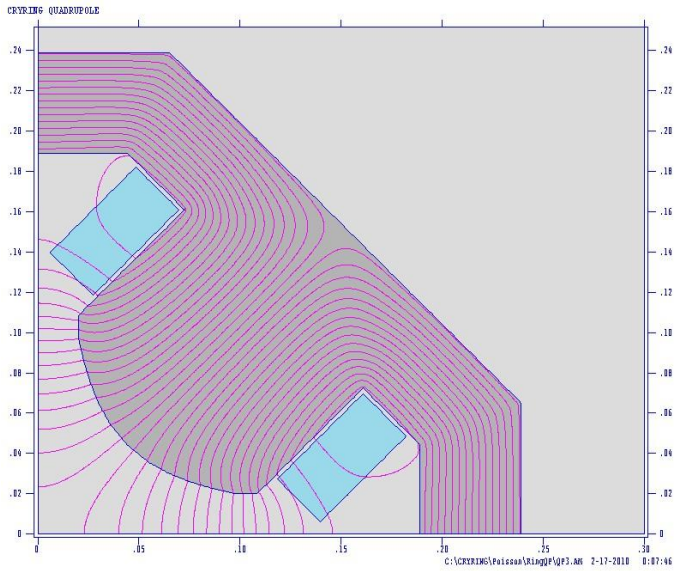

Fig. 3.13. Field lines in one quadrant of a quadrupole magnet as obtained from Poisson. The geometry of the coils (blue) is only approximate.

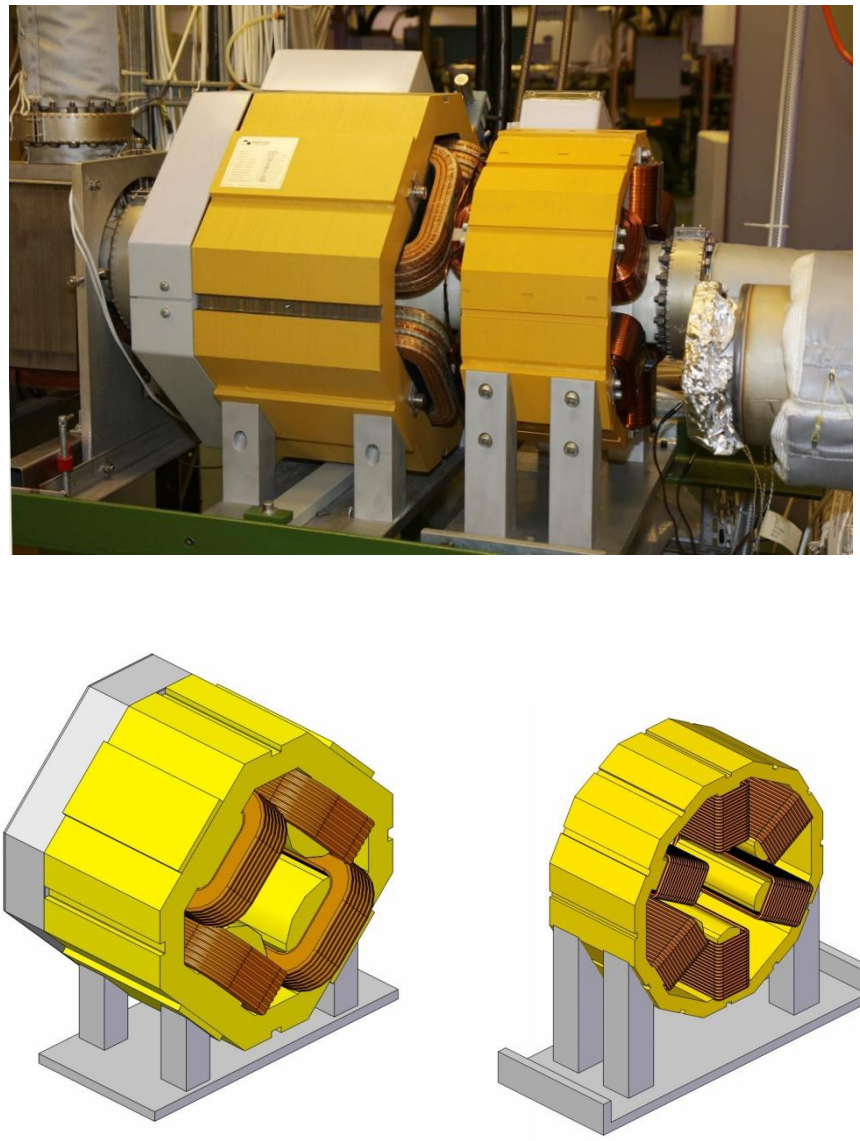

Fig. 3.14. CAD models of a ring quadrupole and a ring sextupole.

The horizontal and vertical correction dipoles, see fig. 3.15, have the same geometry, and they are quite short compared to the gap height, giving a large fringe field. The effective length (i.e., the integrated field relative to the nominal field $\mu_0 NI\ l\ /\ h$, where l is the yoke length and h is the gap height) is 1.58 times the physical length or 190 mm. Fig. 3.16 shows the vertical field component as a function of the coordinate s along the beam, obtained from a 3-d calculation with Tosca. Two of the 12 magnets are slightly different in that they have a larger aperture of 180 mm instead of 120 mm. These are used in the magnet section after the electron cooler where part of the vacuum pipes have 150 mm diameter instead of the standard 100 mm in order to allow detection of highly charged ions that have recombined in the cooler.

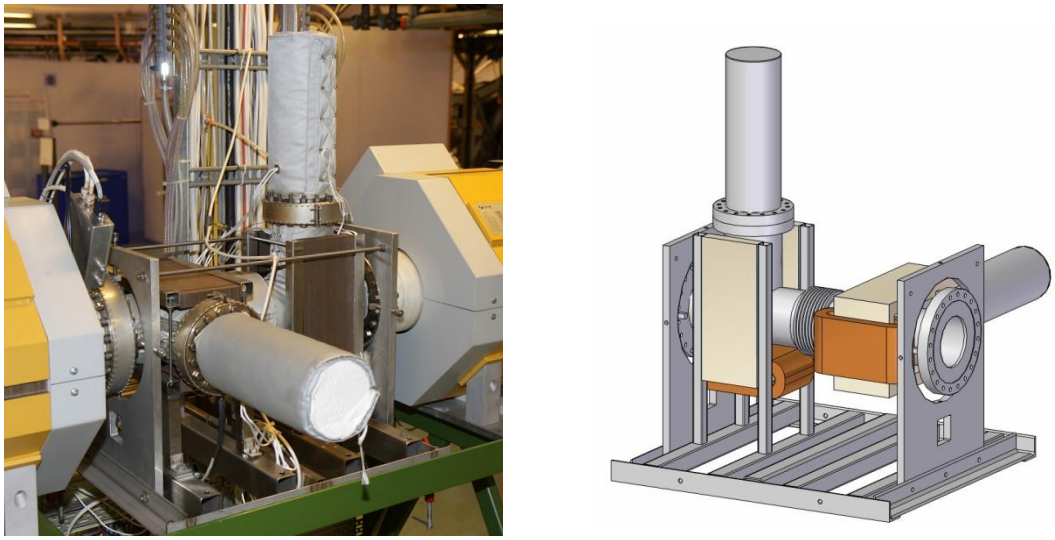

Fig. 3.15. Photograph and CAD model of horizontal and vertical correction dipole magnets, including vacuum chambers and NEG pump units. The CAD model is viewed from the opposite side compared to the photo, in order to show the coils more clearly.

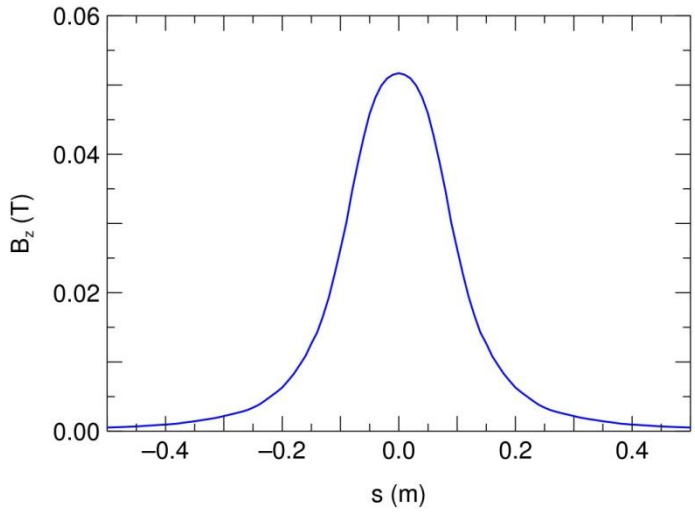

Fig. 3.16. Vertical component of the magnetic field in a horizontal correction dipole as a function of the coordinate *s* along the direction of the beam at the maximum current of 10 A in the winding.

All 12 main dipoles have backleg windings. Ten of the magnets have backleg windings of 30 turns with air cooling and a design current of 30 A. These were added as a precaution in case more degrees of freedom for the closed-orbit corrections would be needed, but there are at present no current supplies for these coils. The two magnets adjacent to the electron-cooler have 32 turns with water cooling and a design current of 125 A. Their function is described in more detail in section 3.11. Also discussed in section 3.11 are the electron-cooler magnets, the correction dipoles at the electron cooler and the compensation solenoid that produces a solenoidal field with the same integrated strength as the cooler solenoids but in the opposite direction.

3.8. Injection

CRYRING at present has a nominally 10-turn electrostatic multiturn injection [10]. There is an electrostatic septum foil that inflects the beam parallel to the circulating beam, and four pairs of kicker plates connected to a common fast voltage supply produce a closed-orbit bump. The closed-orbit bump with maximum 30 mm amplitude decreases over ten turns, although experience shows that the circulating current typically becomes 5−6 times higher than the current in the injection line. All kicker plates are located together with the septum in one straight section, see fig. 3.17, making the injection efficiency quite insensitive to the tune.

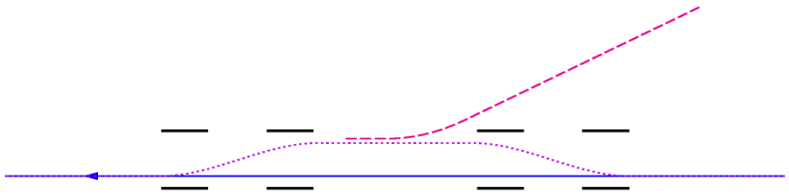

Fig. 3.17. Principle of existing multiturn injection at CRYRING. A local closed-orbit bump (dotted line) is produced by four pairs of electrostatic kicker plates. The injected beam (dashed line) is deflected electrostatically with a thin electrostatic septum foil (not shown) separating the injected beam from the circulating one. The closed-orbit bump becomes progressively smaller during the 10 turns of the injection, and particles become stacked in the horizontal phase space.

At FLAIR, the injection from the NESR will take place at a higher energies than at CRYRING today, and with the present design, the kicker voltages and also the septum voltage would become unacceptably high. For this reason, the injection will be completely rebuilt for FLAIR, although multiturn injection with a local closed-orbit bump will still be used for injection of low-energy ions from the dedicated injector. This is described in more detail in section 5.

3.9. Driven Drift Tube

Acceleration (or deceleration) in CRYRING does not use a resonant cavity but a driven drift tube. The drift tube, see fig. 3.18, has a length of 2.67 m and it is connected to a broad-band amplifier [14, 15]. In a small ring where the required rf voltage is not very high and the drift tube can be made relatively long, this arrangment has the advantage of a very large rf bandwidth and, at least in theory, of an accelerating field that can have an arbitrary waveform. The system is designed for frequencies between 40 kHz and 2.4 MHz, the latter being equal to the revolution frequency of protons at maximum rigidity. A slight disadvantage with the large bandwidth is that the sensitivity to rf noise increases, but in CRYRING this is noticed only when beams are stored for a long time with rf on.

With a driven drift tube, the effective acceleration voltage is the difference between the drift-tube voltage when a particle enters the drift tube and the voltage when it exits. If the time for the particle to pass the drift tube is Δt, this can be written

$$U_{\mathrm{eff}}(t) = U_{\mathrm{ddt}}(t + \Delta t/2) - U_{\mathrm{ddt}}(t - \Delta t/2).$$

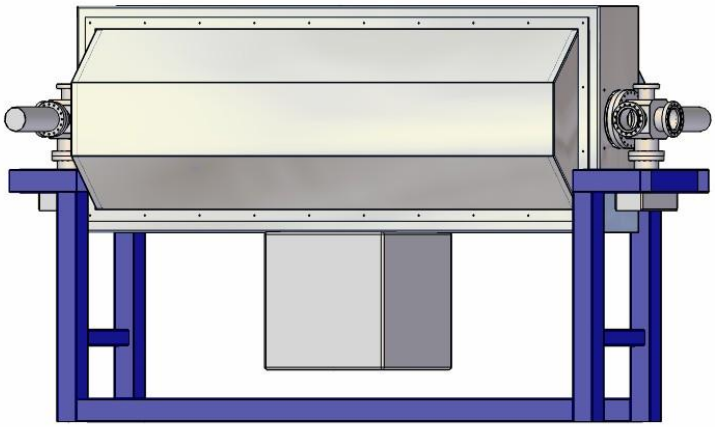

Fig. 3.18. Photograph and CAD model of driven drift tube, the CAD model is shown with the aluminium cover closed. On the photo, the drift tube itself is wrapped in ceramic paper for heat insulation during bakeout.

If $U_{\mathrm{ddt}}(t)$ is sinusoidal, the effective amplitude of the acceleration voltage thus becomes

$$U_{\mathrm{eff}} = 2\sin(\pi h L_{\mathrm{ddt}} / C) U_{\mathrm{ddt}}$$

if h is the harmonic number of the rf frequency. With h = 1, L_{ddt} = 2.67 m and C = 51.63 m, the effective acceleration voltage becomes smaller than the voltage on the drift tube by a factor 3.1.

The power converters for the ring magnets have two ramping modes (see sect. 3.13), a fast mode where the dipole fields change by 7 T/s and a slow mode with 1 T/s or less. The effective rf amplitude needed to accelerate a particle in the drift tube is $U_{\mathrm{eff}} = \rho C \dot{B} / \sin\varphi_{\mathrm{s}}$, where ρ is the magnet bending radius of 1.2 m, $\dot{B}$ is the time derivative of the dipole field, and φ_{s} is the synchronous phase. For a single particle, a lower limit for the required effective voltage is obtained when sin φ_{s} = 1, giving 434 V and 62 V for the two ramping modes, respectively. However, the voltage increases rapidly for a

beam with a non-zero momentum spread. The size of an accelerated bucket in the ΔE–Δt plane, where the size is an adiabatic invariant under acceleration, is [16]

$$A = \frac{1}{h\omega_0}\left|\frac{\beta^2\gamma m_0 c^2 Z q U_{\mathrm{eff}}}{2\pi h\eta}\right|^{1/2} 2\sqrt{2}\int_{\varphi_u}^{\varphi_e}\left|(\pi-\varphi_s-\varphi)\sin\varphi_s-\cos\varphi_s-\cos\varphi\right|^{1/2}\mathrm{d}\varphi\,,$$

where $\varphi_u = \pi - \varphi_s$ and φ_e is obtained from the equation

$$\cos\varphi_e + \cos\varphi_s = (\pi - \varphi_s - \varphi_e)\sin\varphi_s\,.$$

At the same time, an injected, coasting beam with an energy spread $\pm\Delta E$ that has to be contained in the deceleration bucket after adiabatic bunching has a size

$$A_{\mathrm{inj}} = \frac{2\pi}{h\omega_0}2\Delta E = \frac{4\pi\beta^2\gamma m_0 c^2}{h\omega_0}\frac{\Delta p}{p}\,.$$

Setting $A = A_{\mathrm{inj}}$, the required rf voltage is obtained as a function of momentum spread and ramp rate for a certain injected beam. Fig. 3.19 shows the required drift-tube voltage (peak-to-peak) as a function of momentum spread for antiprotons injected 30 MeV and for highly charged ions with charge-to-mass ratio 0.5 at the same magnetic rigidity as 30 MeV antiprotons. Curves are drawn both for the slow and the fast ramping modes.

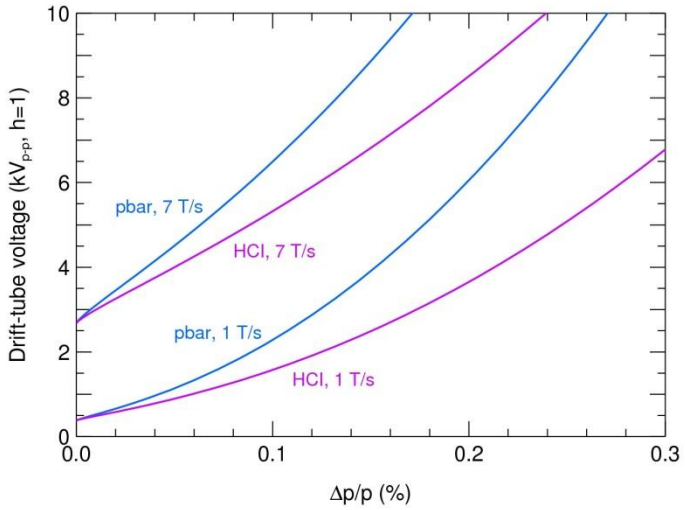

Fig. 3.19. Drift-tube voltage required for deceleration at the first harmonic of the revolution frequency of antiprotons and highly charged ions with $Z/A = 0.5$ as a function of the relative momentum spread. Curves are drawn both for the slow ramping mode where dB/dt in the ring dipole magnets is approximately 1 T/s and for the fast ramping mode with dB/dt about 7 T/s. The effective acceleration voltage is smaller by a factor 3.1 at $h = 1$.

At present, CRYRING has a system for rf power that covers the slow ramping mode only. It delivers 0–1000 $V_{p\text{-}p}$ to the drift tube which constitutes a capacitive load of approximately 120 pF, see fig. 3.20, and it has a bandwidth of 2.5 MHz. It consists of a numerically controlled oscillator (NCO) built at FZ Jülich, an amplitude modulator built at MSL, a modified 200-watt ENI 2100L linear solid-state

amplifier and a balun transformer. With a sinusoidal waveform, the 200-watt amplifier produces 280 $V_{p\text{-}p}$ into 50 Ω which the balun transformer multiplies by 4, resulting in the 1000 $V_{p\text{-}p}$ on the drift tube.

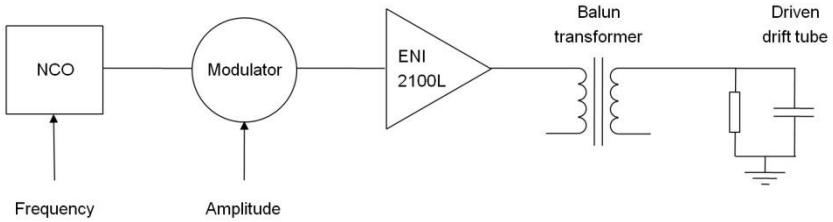

Fig. 3.20. Schematic diagram of rf electronics with numerically controlled oscillator, modulator, linear amplifier and balun transformer. The total capacity of the load is 160 pF and there is an 800-Ω resistor in parallel to the drift tube to match the 50-Ω output of the linear amplifier.

The existing rf system is sufficient for slow-mode acceleration at CRYRING where, for example, 1000 $V_{p\text{-}p}$ on the drift tube is enough to accelerate a proton beam with $\Delta p/p \leq 4\times10^{-3}$ from 300 keV at a magnet ramp rate of 1 T/s. However, with the same drift-tube voltage, a 30-MeV antiproton beam can be accelerated (or decelerated) with 1 T/s only if the relative momentum spread is 10 times smaller, i.e., if $\Delta p/p \leq 4\times10^{-4}$. For this reason, the design of a solid-state dc amplifier with higher output voltage is at present being considered at MSL.

3.10. Vacuum

The vacuum system of CRYRING [17], including the last 4.5 m of the injection beamline, is designed for pressures in the range of 10^{-11}–10^{-12} mbar. Most of the beam pipes are made from 100-mm-diameter stainless steel with CF 100 flanges. The vacuum chambers in the dipole magnets have an internal height of 54 mm. The six dipole chambers at the end of the magnet-free straight sections have large rectangular flanges with Helicoflex gaskets to allow more flexibility in the installation of particle or light detectors. A representative example is seen in fig. 3.21. At the dipole after the cooler, a bigger chamber with more ports for detection of charge-changed ions has been installed, but it is suggested to replace this with the original standard chamber when the ring is reassembled as the LSR.

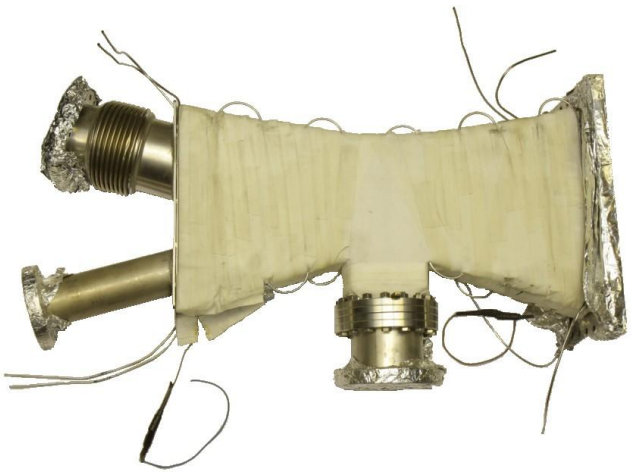

Fig. 3.21. Dipole vacuum chamber with rectangular flange on one side.

With very few and small exceptions, all vacuum chambers are made from 316 LN steel. After manufacturing, they have been vacuum fired at 950 degrees Celsius in order to remove hydrogen from the steel. In addition to stainless steel, alumina (Al_2O_3) and in some cases OFHC copper has been used.

The ring and all vacuum components belonging to it are bakeable, and after venting to air, a bakeout is always performed. In a typical bakeout cycle, the temperature is increased to 200–300 degrees at a rate of 25–50 degrees per hour, the temperature is maintained at the maximum value for 20–30 hours, and it is decreased back to room temperature with the same rate as the increase.

All components of the ring have heating jackets that either are permanently installed (such as inside the magnets) or removable. Permanently installed jackets are made from ceramic paper wrapped in fiberglass tape and have coaxial heating cables spot-welded to the vacuum chambers. The removable jackets, manufactured by Hemi Heating, have heating wire and thermal insulation integrated. Bakeout of vacuum flanges are made with heating collars. The complete bakeout system consists of approximately 300 individually controlled channels for heating elements and with temperature readout from thermoelements. Each channel has a 10-A fuse and can thus deliver at most 2.3 kW. The total installed power of all heating jackets is 210 kW, and at CRYRING the available power is sufficient to permit that the entire ring is baked out at the same time.

The different channels are grouped into eight separate microprocessor-controlled hardware units which are programmed from a pc. These units read the temperatures from the thermoelements and regulate the heating current autonomously. They are, however, becoming obsolete, it is difficult to find spare parts to them, and they should preferably be replaced by more modern controllers at FAIR.

Pumping in CRYRING relies heavily on NEG (Non-Evapourable Getter) pumps, complemented with ion pumps and cryopumps. CRYRING has approximately 40 NEG pump units, see fig. 3.22, built in-house from 100-mm-diameter stainless-steel pipes and strips of SAES707 getter. Each pump unit has 5 m of NEG strips and has an esitmated pumping rate of at least 500 l/s for hydrogen. These units are activated at 350ºC for at least 2–3 h at the same time as the rest of the respective vaccum sector is baked out. Their total capacity is sufficiently large compared to normal outgassing rates that they never need to be reactivated if the system is not opened to air.

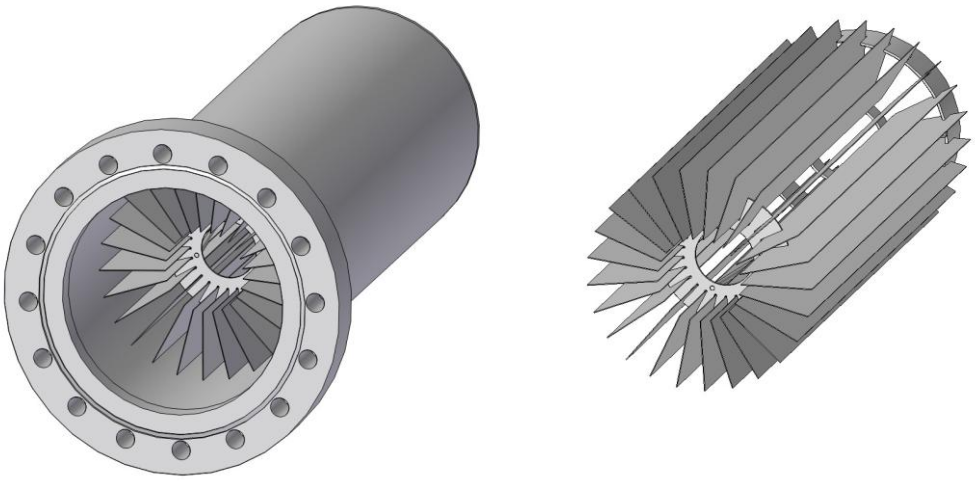

Fig. 3.22. Typical NEG-pump unit used in CRYRING, with and without vacuum can.

NEG material does not pump, e.g., noble gases and methane, and the NEG pumps are therefore complemented mainly by ion pumps. The ring originally had 12 Varian StarCell ion pumps of 60 or 120 l/s pumping rate. It has been found unnecessary to have this many ion pumps, and it is planned that the ring will be rebuilt at FLAIR with 6–8 ion pumps. These units will need to be equipped with new Varian MiniVac dual controllers or similar since the existing ion-pump controllers are quite old and somewhat unreliable. There are in addition two cryopumps at the electron gun and at the collector of the electron cooler, and more details are found in section 3.11 about the electron cooler.

CRYRING has altogether nine Balzers TCP300 vacuum gauge controllers connected to seven IKR060 and nine IKR070 inverted-magnetron gauges. The IKR060 gauges can measure down to 2×10^{-9} mbar and are used in the injection line and on the two cryopumps on the electron cooler. The IKR070 gauges are used in the R1b line and in the ring and can display nitrogen-equivalent pressures down to 1×10^{-11} mbar. Almost all of these are in underrange condition during normal operation. The ring is divided into eight vacuum sectors separated by pneumatically operated all-metal gate valves. Each sector has at least one vacuum gauge and a port for pump-down. The gate valves are controlled by the vacuum gauges such that the valves close if the pressure on either side of them exceeds pre-defined setpoints.

Although most vacuum gauges show underrange most of the time, the average pressure in the ring can be determined by storing particles with low cross sections for charge-exchange reactions in collisions with residual-gas molecules, such as protons or deuterons, and observe the rate at which an uncooled beam loses kinetic energy in collisions with the residual gas. The energy loss rate for such particles can be written as [18]

$$\frac{\mathrm{d}E}{\mathrm{d}x} = \frac{\mathrm{d}p}{\mathrm{d}t} = \frac{4\pi N_\mathrm{t} r_\mathrm{e}^2 m_\mathrm{e} c^2 Z_\mathrm{t} Z^2}{\beta^2} \ln \frac{2 m_\mathrm{e} c^2 \beta^2 \gamma^2}{10 q_\mathrm{e} Z_\mathrm{t}},$$

where N_t, and Z_t are the number density and atomic mass of the target species and β, γ and Z are the relativistic parameters and the charge of the stored particle. Fig. 3.23 shows how the Schottky frequency at the 10th harmonic of the revolution frequency for a beam of 3 MeV deuterons decreases as a function of time due to this energy loss. Assuming that half of the energy loss is due to hydrogen and half due to heavier residual-gas components (see below), it is found that the true pressure of hydrogen molecules in the ring was 8×10^{-11} mbar at the time when the curve was recorded. Other similar measurements have shown a true hydrogen pressure down to approximately 3×10^{-11} mbar when the ring has been well baked and has been under vacuum for an extended period of time.

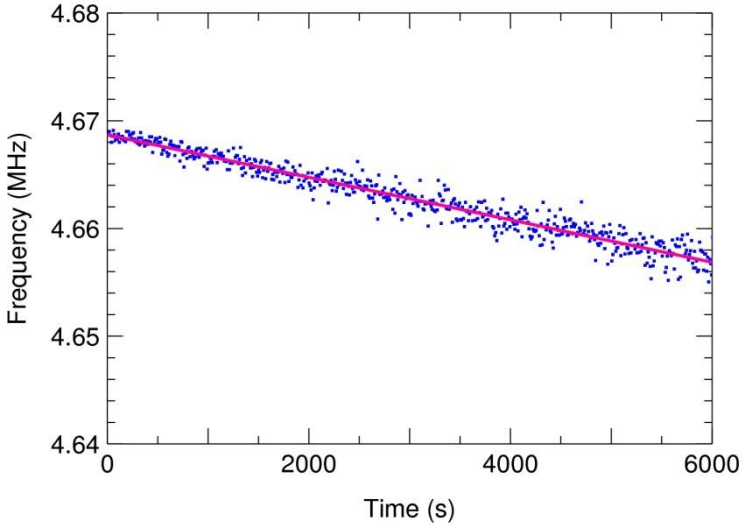

Fig. 3.23. Decrease in Schottky frequency as a function of time for a 3-MeV deuteron beam, resulting from friction against the residual gas and allowing the determination of the absolute pressure in the ring if the residual-gas composition is known on a relative scale.

Fig. 3.24 shows the residual-gas composition on a relative scale as measured with a Balzers QMA 125 residual-gas analyzer. As in any leak-tight and baked ultra-high-vacuum system, the completely dominating component is hydrogen which is contained in stainless steel from the manufacturing process. Methane is formed from this hydrogen and carbon also contained in the steel and is not so efficiently pumped by the NEG. Some water remains in spite of the bakeout, and some heavier components, such as CO, probably result from the filament of the RGA itself or from the ion pumps.

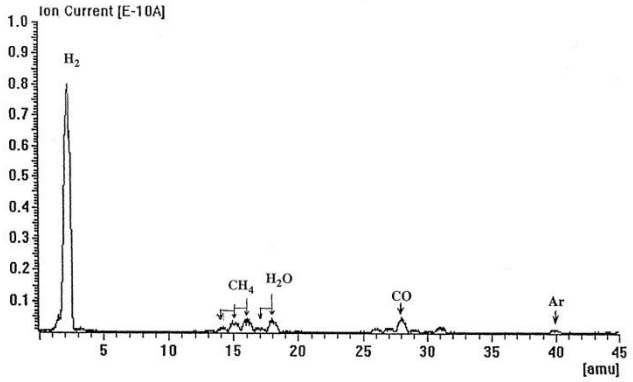

Fig. 3.24. Typical residual-gas composition as measured with a Balzers QMA 125 residual-gas analyzer having a low-EID (ion electron desorption) option to reach lower backgrounds and higher sensitivity.

3.11. Electron Cooling

The electron cooler at CRYRING [19] serves the dual purpose of phase-space cooling of the stored ion beam and acting as an electron target in investigations on ion–electron recombination. It was substantially rebuilt in the late 1990's, when a superconducting gun solenoid was installed in order to lower the transverse electron temperature by a factor of up to 100 through a magnetic expansion of the

electron beam [20–23]. A cross section and a CAD model of the cooler are shown in fig. 3.25, and main parameters are given in table 3.5. A photograph of the cooler is found in fig. 2.3.

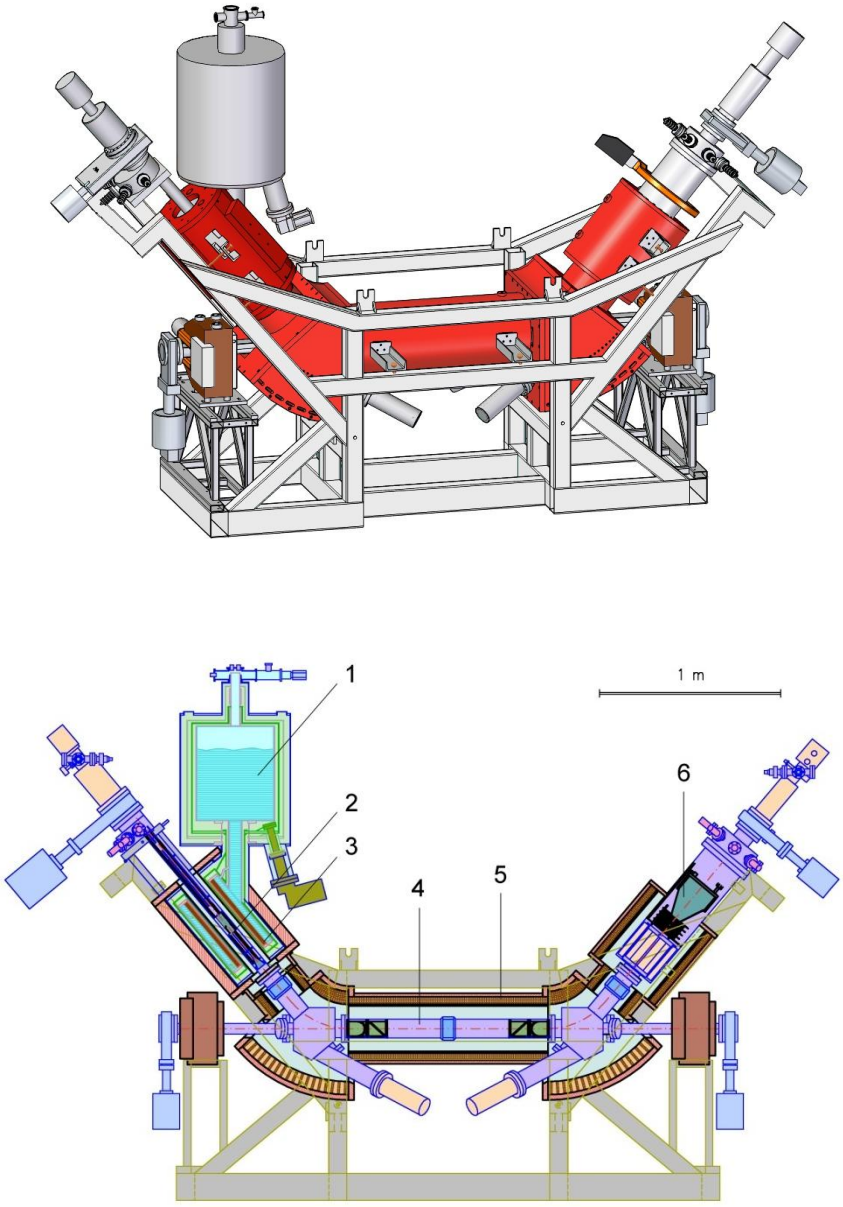

Fig. 3.25. CAD model and cross section of the CRYRING electron cooler with 1) liquid-helium reservoir, 2) electron gun, 3) superconducting gun solenoid, 4) vacuum chamber, 5) normal-conducting magnets, 6) electron collector.

Main components of the electron cooler are normal-conducting solenoid and toroid magnets, the superconducting gun solenoid with a cryo-generator, steering coils and correction coils, vacuum system with NEG-pumps and cryopumps, electron gun and electron collector. Integrated on the support frame are also two correction dipole magnets, and there is a compensation solenoid on another straight section. Approximately 20 voltage and current supplies belong to the electron cooler.

Parameter	Design value	Value used in operation
Length of cooling section	1.1 m	
Toroid angle	50°	
Field strength, normal conducting magnets	< 0.3 T	0.015 – 0.18
Field strength, superconducting solenoid	< 5 T	0.3 – 4
Cathode diameter	4 mm	
Beam expansion factor	< 100	10 – 100
Electron energy	0 – 20 keV	0.004 – 8.1 keV
Electron current	0 – 3000 mA	0 – 110 mA
Perveance	0 – 5 $\mu A/V^{3/2}$	0 – 4.8 $\mu A/V^{3/2}$

Table 3.5. Electron cooler parameters. The values in the last column are those used for cooling or recombination experiments with the superconducting version of the cooler, when different from the design value.

There are seven magnets that guide the electron beam from the gun to the collector: gun solenoid at the electron gun, cooling solenoid at the interaction region in the centre, collector solenoid at the electron collector, two toroid magnets bringing the electron beam in and out of the ion beam, and two smaller solenoids on top of the toroids. These normal-conducting magnets, including the normal-conducting gun solenoid from the original cooler setup, were delivered by Danfysik A/S. The normal-conducting gun solenoid is kept in storage and it can be reinstalled if required. All magnets are wound with hollow copper conductors. The solenoids are wound on aluminium mandrels whereas the toroids are made from 18 individual pancake coils each. A yoke of soft iron surrounds all magnets except for the two openings where the ion beam goes in and out and six openings for the collector, pumps and other connections together. The magnets are designed for a maximum field of 0.3 T, corresponding to a current of 600 A. All normal-conducting solenoids and toroids are connected in series to a single current supply.

A superconducting solenoid manufactured by Everson Electric Co., providing a field of up to 5 T nominally, is used for the electron gun [23]. During acceptance tests, the magnet quenched at 4.7 T, and, although it was believed that the quench was due to a misalignment of the coil with respect to the yoke and this alignment was improved after the quench, it has since then not been used at fields higher than 4.0 T. The magnet is cooled with liquid helium and a Gifford-McMahon cryocooler, the two stages of which under steady-state conditions operate at 68 and 32 K respectively. There is a liquid-helium reservoir in the upper part of the magnet assembly, and together with the lower part where the coil is, the cryostat can hold up to 68 l of LHe. With a boil-off rate of 4.5 l per 24 h, it needs to be refilled every 12–14 days.

A compensation solenoid, shown in fig. 3.26, is installed in another straight section. Its purpose is to remove the coupling between horizontal and vertical particle motion introduced by the solenoidal field in the cooler. This solenoid, from Sigmaphi, has essentially the same number of turns as the cooling solenoid and the two toroids together, and it is powered in series with the normal-conducting cooler magnets, ensuring that it always provides the right compensation.

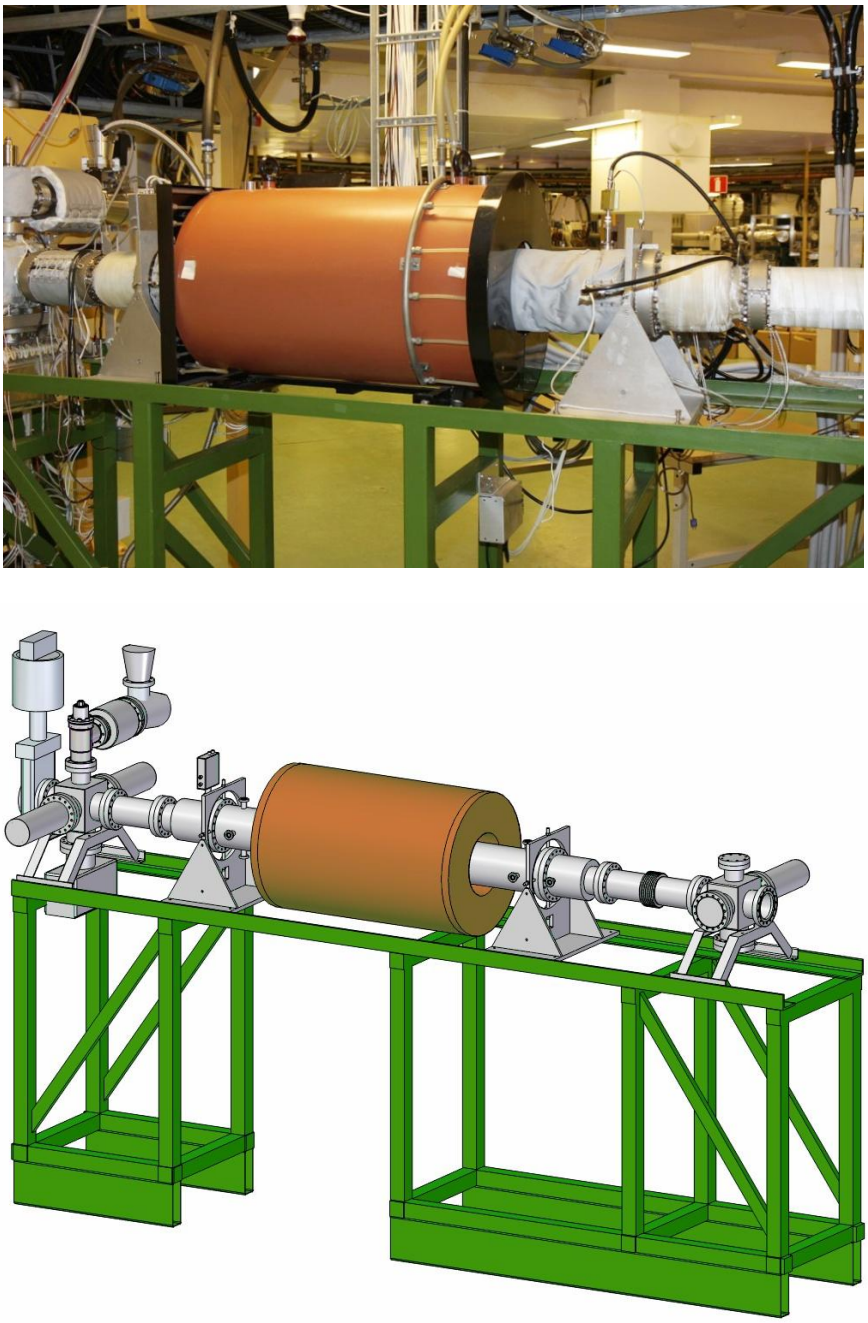

Fig. 3.26. Photograph and CAD model of compensation solenoid with Schottky detector, see section 3.15, inside. Two of the four preamplifiers for the Schottky detector with their black signal cables are seen on the photo, to the right of the solenoid. The CAD model does not include the black plastic covers around the electrical connections to the solenoid.

The toroidal fields that bring the electron beam in and out of the ion beam in the vertical plane also cause a deflection of the ion beam in the horizontal plane. To compensate for this and align the ion beam with the closed orbit, two additional dipole fields are thus needed at each side of the cooler. These fields are provided by the two correction dipoles mounted on the support frame of the cooler and by backleg windings on the adjacent main dipole magnets. A CAD model of a correction dipole is shown in fig. 3.27. As a second-order effect, there is also a small vertical deflection in the toroids, but

there are no dedicated magnets to compensate for this. Instead, the vertical correction has to be made with the regular correction dipoles in the ring.

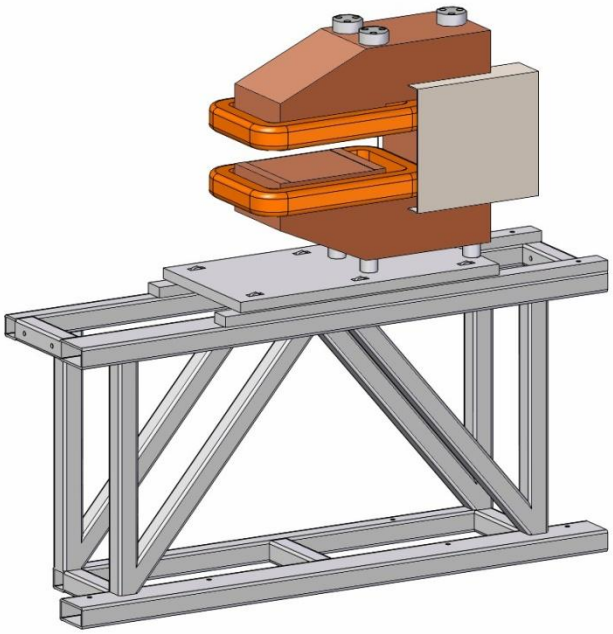

Fig. 3.27. CAD model of one of the two correction dipoles on the electron-cooler support frame.

The correction dipoles at the cooler are, like the compensation solenoid, powered in series with the solenoids and toroids. To avoid large closed-orbit distortions it is important that the field strength in the correction dipoles can be given the right value although the magnets are powered in series with the rest of the cooler. For this reason, a coarse adjustment can be made by mechanically shunting up to four out of the 20 turns of each dipole winding. This adjustment was made once and for all during the commissioning of the cooler. A fine adjustment is then made with a dual-channel supply which can shunt up to 50 A and which can be regulated as any other power supply to optimize the beam intensity and quality.

The backleg windings on the two main dipoles next to the electron cooler are made with a hollow water-cooled conductor, in contrast to the (unused) backleg windings on the other main dipoles. A current supply common to both windings can give up to 160 A corresponding to approximately 0.08 T in the dipole magnets. This is sufficient so that the maximum possible horizontal deviation of the beam due to the toroid fields is determined by the horizontal aperture of the beam pipe and the CF 100 gate valve between the cooler and the main dipoles. This aperture limits, as an example, the solenoid field in the cooler to approximately 0.02 T at the magnetic rigidity of 300-keV protons.

In the 1.1 m long cooling solenoid there are two saddle-shaped correction coils attached to the inside of the aluminium mandrel. These were wound after field measurements in the cooling solenoid with the purpose to make the solenoid field as straight as possible. As a result, the field could be made straight within better than ±0.1 mrad over the central 70 cm of the solenoid and within ±1 mrad over 80 cm [19]. There are also two pairs of steering coils, one horizontal and one vertical, to adjust the alignment between the electron beam and the ion beam. On the gun side, there is another set of steering coils inside the small solenoid below the superconducting magnet (or inside the normal-

conducting gun solenoid if this is used) to optimize the overlap between electron and ion beams, and there is a third set of coils inside the collector solenoid to steer the electron beam back into the collector. All these steering coils are saddle-shaped and attached to the aluminium mandrels. Inside each toroid there is a pair of vertical dipole coils to counteract the centrifugal drift that the electrons otherwise will get in the toroids. These 10 coils are powered by individual bipolar ±10 A current supplies.

The adiabatic expansion of the electron beam is based on the fact that the ratio between transverse energy and longitudinal field is an adiabatic invariant under slow variations of the magnetic field, i.e.,

$$\frac{W_{\perp}}{B_{||}} = \frac{mv_{\perp}^2/2}{B_{||}} \approx const.$$

At the same time as the electron beam expands, the electrons following the field lines in the decreasing field, the transverse energy spread thus decreases in proportion to the field strength. With the normal-conducting gun solenoid, an expansion factor of 10 could be obtained, running the gun solenoid at 0.3 T and the rest of the cooler magnets at 0.03 T. At the same time as the beam expansion was introduced, the linear dimensions of the electron gun were reduced by a factor square root of 10, keeping the beam diameter in the cooling section and the collector at the design value of 40 mm. With the superconducting gun solenoid, designed for an expansion factor of 100, yet another gun was built, the linear dimensions of which are 10 times smaller than in the original gun, giving a cathode diameter of only 4 mm. Note that this change in cathode diameter does not lead to a change in gun perveance, and the electron current is thus still the same for a given potential difference between cathode and anode.

The lower transverse electron temperature resulted in an increased cooling force (higher than any values published at that time), but in particular in a much improved resolution in recombination spectra. The electron temperature can be measured from the peak shapes in such spectra, and as an example, a spectrum of dielectronic recombination of F^{6+} is shown in fig. 3.28. For this system, a precise calculation of the $1s^2 2s(^2S) + e^- \rightarrow 1s^2 2p(^2P)6l$ resonances below 0.6 eV was made by E. Lindroth [24]. The spectrum shows a central peak at 10 meV (assigned to $1s^2 2p(^2P_{3/2})6p^2P_2$) sitting on a background of radiative recombination and other dielectronic-recombination peaks. The central peak, approximated by a delta function, plus the calculated background can be convoluted with a Maxwellian electron-velocity distribution and fitted to the experimental data, giving a transverse electron temperature $kT_{\perp}$ of 1.5 meV and a longitudinal temperature $kT_{||}$ of 0.10 meV. In other measurements with the same 100 times expansion, typical values for the electron temperature have been $kT_{\perp}$ = 1.5–3.5 meV and $kT_{||}$ = 0.05–0.2 meV.

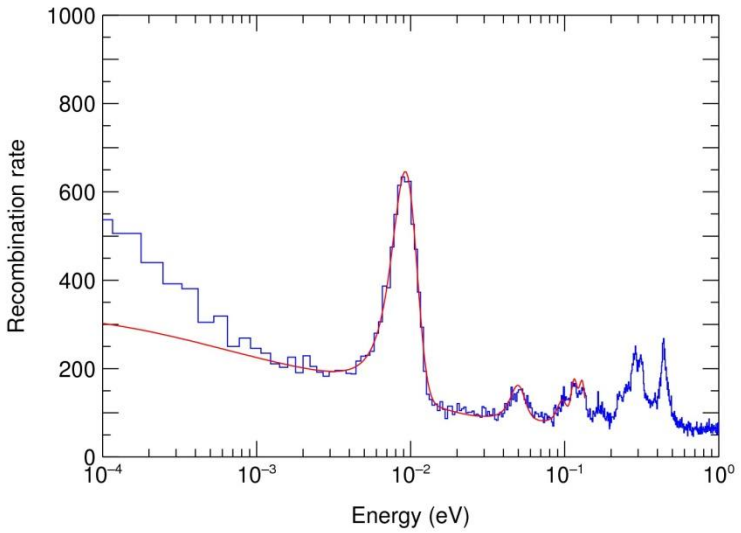

Fig. 3.28. Rate for dielectronic recombination of F^{6+} ions in CRYRING. The red curve is a fit to the blue experimental spectrum, containing a large peak at 10 meV. Including a background calculated by E. Lindroth [24] the fit to the 10-meV peak gives $kT_{\perp}$ = 1.5 meV and $kT_{\parallel}$ = 0.10 meV.

The electron gun has a 41180M oxide-impregnated tungsten cathode from Spectra-Mat, Inc., typically heated to around 900ºC by an embedded filament. It has one regular anode determining the current extracted from the cathode. There is a second 295 mm long anode introduced with the intention to achieve a longitudinal–longitudinal relaxation [25] at a voltage between the cathode voltage and earth. Such a relaxation would be fast in the high magnetic field of the superconducting magnet, and it was expected that a lower longitudinal electron temperature would result under certain conditions. No substantial effect on the temperature was seen, however, when the voltage on the second anode was changed, so now it is permanently on earth potential. The gun assembly fits inside a vacuum pipe with 58 mm inner diameter.

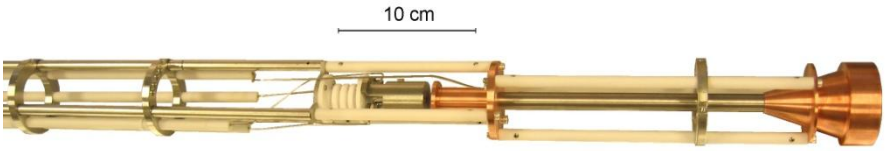

Fig. 3.29. Photograph of the electron gun for the superconducting gun solenoid. The cylindrical molybdenum piece in the centre is the outside of the anode, and the cathode is inside. The two copper pieces joined by a titanium tube constitute the second anode which in now permanently on earth potential.

The collector is a water-cooled can from OFHC copper with a conical opening, adapted to a beam diameter of 40 mm. It has three anodes in front of the collector opening for a smooth deceleration of the electrons into the collector. It is designed for a power dissipation of 10.5 kW which is the maximum which can be provided by the collector supply, although such high powers never have been used.

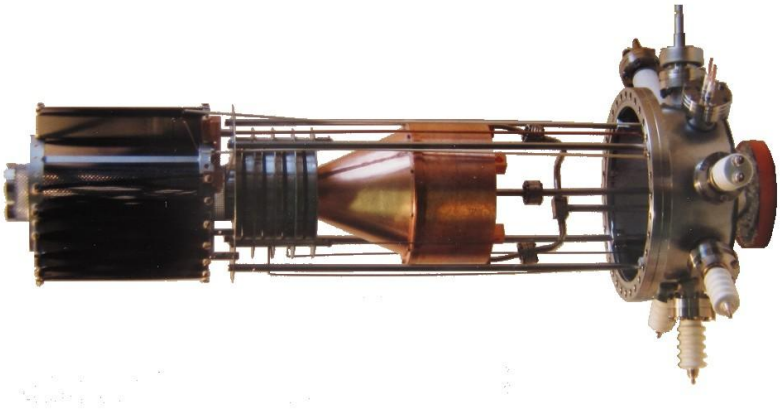

Fig. 3.30. Photograph of the electron collector with three anodes in front of it. To the left there is a drift tube made of steel mesh on earth potential which is surrounded by NEG strips. The entire unit is mounted on a CF 250 flange.

Most commonly, both for beam cooling and recombination experiments, the field in the superconducting solenoid is 3 T and in the normal-conducting magnets 0.03 T. Protons at the injection energy in CRYRING of 300 keV have a rigidity which is too low for a field of 0.03 T in the cooler, and the deflection in the toroids becomes too large. In this case the field is normally reduced to 1.5/0.015 T without negative effects for the cooling.

With the normal-conducting gun solenoid, the cooler was operating with electron energies up to 13 keV (corresponding to maximum ion energy in CRYRING for $q/A = 1/2$) and with currents up to 500 mA, and higher values were used for tests. With the superconducting solenoid, however, maximum values have been in the order of 8 kV and 100 mA. The difficulty in reaching higher voltages and currents are presumed to be due to the relatively high electric fields accelerating the electrons in the new small electron gun (which has ten times smaller linear dimensions than the original gun), and these fields must be parallel to the high magnetic field, which easily causes discharges. Some improvements have been made to the insulators of the gun which have not yet been tested to maximum voltage, but it is probable that this electron gun for the superconducting gun solenoid will not be able to cool antiprotons at the injection energy in LSR of 30 MeV. This should also not be necessary if the beam is cooled in NESR before transfer. If, nevertheless, cooling at 30 MeV turns out to be necessary, further attempts to improve the existing gun could be considered or the original normal-conducting gun solenoid will have to be reinstalled.

The performance of the electron cooler for protons and H^- ions, at energies relevant for FLAIR is discussed in section 7.

3.12. Beam Diagnostics

Beam diagnostics in CRYRING [26] includes fluorescent screens, Faraday cups, strip detectors, electrostatic pickups, Schottky pickup, beam profile monitors, dc and ac current transformers and diagnostic kickers. A device similar to a REX viewer [27, 28] has been developed and tested at MSL, and this is proposed as a cost-effective diagnostic device for the FLAIR beamlines.

The fluorescent screens, mounted on pneumatic actuators, are used only in the injection line. Closest to the ion source, a CsI(Tl) screen is used due to its high sensitivity, both in general and in particular for low energy ions. The other screens used are of Chromox type, from Morgan Technical Ceramics, made of aluminium oxide doped with chromium oxide. There are three Chromox screens between the RFQ and the ring. They are mainly used for alignment of the beam, where quadrupole currents are varied and the resulting movement of the beam spot on a downstream fluorescent screen is minimized [29]. All the screens are covered with a thin metal mesh (95% transparency) to avoid charging up of the surface, and the light is registered by standard video cameras (Hamamatsu C5405 with removed IR filter). The beam pulses after the RFQ are in the order of 1 ms long, and beam currents down to a few tens of nA can normally be seen. For ions with $Z/A < 1/4$, which are not accelerated in the RFQ and for which the RF amplitude is much lower, the RFQ pulse length can be increased to allow weaker beams to be seen.

There are four Faraday cups—one between the ion source and the RFQ, one between the RFQ and the ring and two in the ring. These are also mounted on pneumatic actuators and are provided with an electrode for repulsion of secondary electrons. Electrometer amplifiers are used, enabling current measurements in the full range of ±1 μA and ±100 μA with 20 μs rise and fall time. The electrometer amplifiers are followed by 40 dB/decade low pass filters and differential output amplifiers. The full range of the electrometer amplifiers and the filter time constants can be changed remotely. The amplifier signals can be read locally on oscilloscopes, and they are also digitized in the control room and available to control software such as LabVIEW programs.

Strip detectors [30] are used in the beamline from the ECR source and occasionally for the singly charged ions from the MINIS platform (and earlier they were used also in the EBIS beamlines). They consist of 16 horizontal and 16 vertical aluminium strips in two layers. The front layer has narrower strips such that the transmission to the back layer of strips is 50%. The beam profiles are obtained by parallel integration of the currents on the 32 strips during the beam pulse. The outputs from the 32 integrators are multiplexed and fed to an ADC included in a Siemens microcontroller. With the programmable microcontrollers and network client/server software in a dedicated pc, the strip detectors are powerful and versatile devices. The pc software will, however, probably be somewhat outdated by the time when LSR comes into operation, and since the strip detectors are not essential for the beam transport from the MINIS source to the ring, the use of the strip detectors for LSR should be considered optional.

For beam-position/closed-orbit measurements, eight horizontal and eight vertical electrostatic pickups are installed in the ring. An additional two of each kind are mounted inside the cooling solenoid of the electron cooler. One electrostatic pickup consists of a 150 mm long diagonally cut cylinder with the same 100-mm diameter as the beam pipe, as seen in fig. 3.31. The pickups in the cooler are smaller with a length of 100 mm and an inner diameter of 77 mm. The electrode capacitance is 40 pF and the coupling capacitance between the electrodes is about 10 pF. The system has a resolution of 0.1 mm and an absolute accuracy of 1 mm. To preserve signal integrity against noise and to avoid attenuation due to unwanted stray capacitance, the preamplifiers are mounted directly on the vacuum feedthroughs of the pick-ups. The preamplifier is a combination of sum and difference switchable gain amplifiers with 60/80 dB gain and 1 $\mu V/Hz^{1/2}$ equivalent input noise in the 4 kHz–10 MHz frequency range. (At present, three pickups use these preamplifiers while the others use an older type with ten times higher noise, but it is planned to replace all of them with the new type.) The construction of the preamplifiers gives the possibility to choose between forming the sum and difference signals before or after the

digitalization. Closed-orbit measurements are not performed during normal beamtimes for experiments (c.f. section 3.17). Instead, one of the sum signals is connected to a spectrum analyzer for intensity monitoring and optimization. Originally, all pickup signals were connected to peak detectors, digitized and processed by a dedicated VME computer for the closed-orbit measurements [31, 32], but this system is no longer in use.

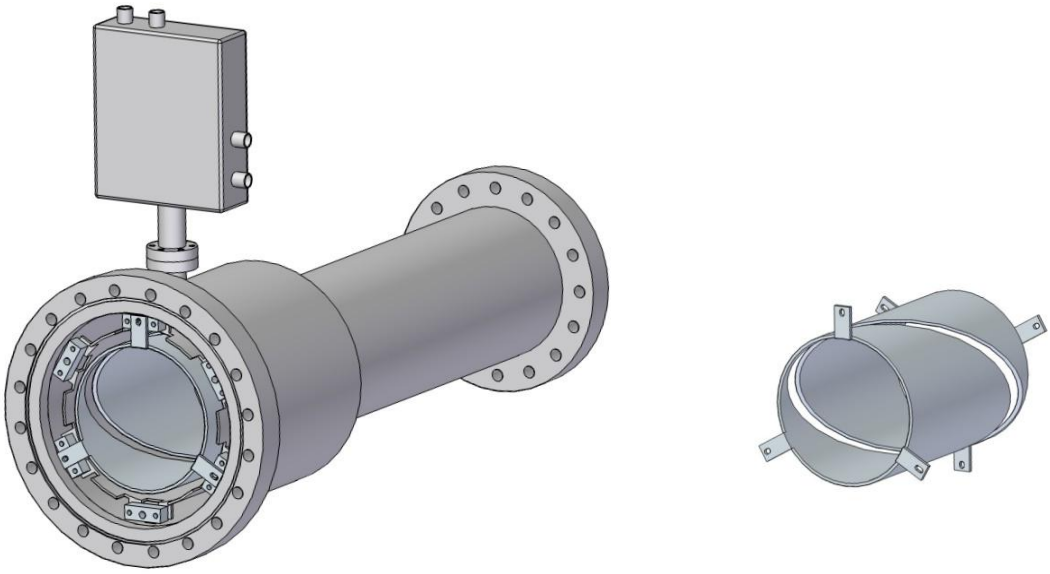

Fig. 3.31. Horizontal electrostatic pickup, inside vacuum chamber and including preamplifier to the left and bare pickup electrodes to the right. The vacuum chamber extends through a quadrupole magnet as seen in fig. 3.2.

A Schottky noise pick-up is installed in the diagnostics straight section, extending through the compensation solenoid for the electron cooler, see fig. 3.26. The pick-up consists of four 1350 mm long steel electrodes aligned with the beam, giving the possibility for longitudinal as well as transversal Schottky noise measurements. The four signals are amplified by low noise, 50 MHz bandwidth, 200 ohm input impedance amplifiers from Trontech Inc. at one end of the electrodes while the other end is open, and the Schottky pickup is thus similar to a long capacitive pickup. The sum and difference signals are formed by hybrid transformers connected directly to the amplifier outputs and are sent to spectrum analyzers in the control room.

To measure the transverse density distribution of a stored ion beam, residual gas ionisation beam profile monitors (RGBPM) which detect the ionisation products arising from the interaction of the ion beam with the residual gas are used [33]. One horizontal and one vertical unit are installed in the ring, measuring horizontal and vertical profiles of the stored ion beam with a spatial resolution of about 0.5 mm FWHM. Examples of vertical beam profiles are seen in fig. 7.3. The imaging components for these detectors are MCPs mounted in a chevron configuration (set of two 40 mm diameter MCPs) matched to a resistive anode encoder. The electrode arrangement of the RGBPM and the related electronics are shown in fig. 3.32.

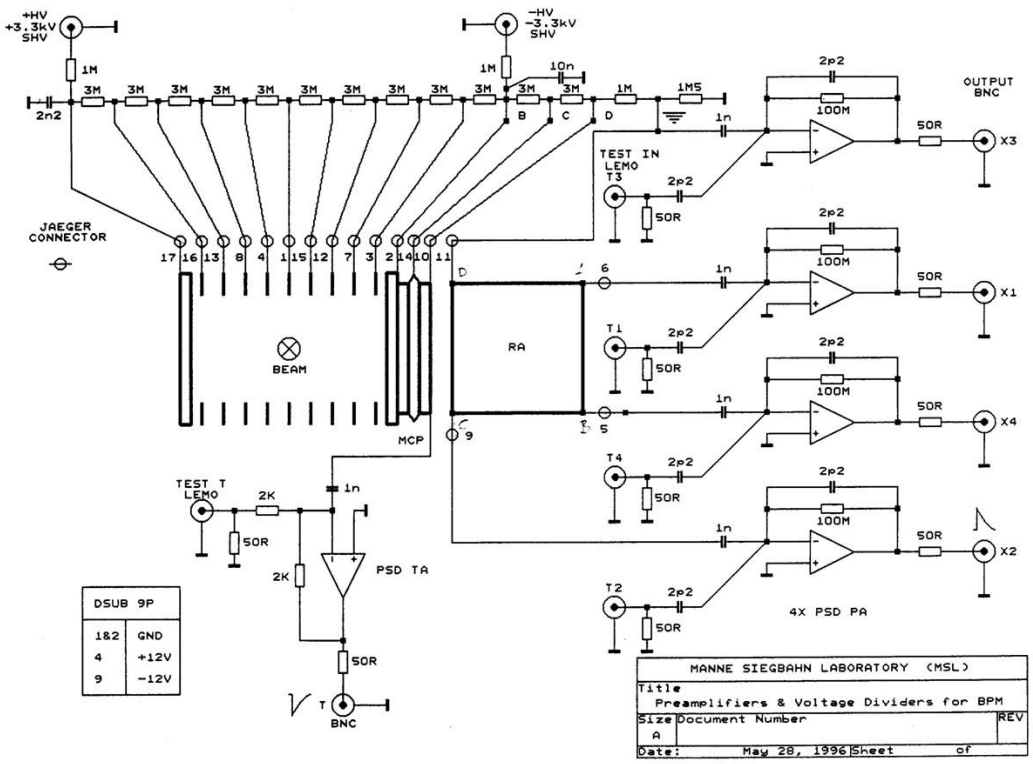

Fig. 3.32. Electrode arrangement, voltage divider network, preamplifiers and timing circuit for residual gas ionization beam profile monitors.

Position signals from the resistive anode are derived with a charge-division method. Charge pulses at each corner of the resistive anode are integrated in charge-sensitive preamplifiers. The absolute *x*, *y* location of an event is computed by two analogue dividers coupled to the stretched bipolar signals from the main amplifiers. For real-time visualisation with a PC, an outdated ISA-bus card with ADCs is used which will have to replace by contemporary-standard hardware at FLAIR. A timing signal is generated by a fast transimpedance amplifier from the second MCP electron current with 2 ns rise time and 10 ns pulse width.

A standard tool for absolute beam-current measurements at CRYRING is a Parametric Current Transformer from Bergoz. This is a DC device with a sensitivity of 10 mV/µA and a nominal 0.5 µA resolution for 0.1 s integration time. The current transformer is shielded from stray fields with several layers of mu metal. In addition, wire loops are wound around the transformer core which are connected through potentiometers to the windings of the nearby dipole and quadrupole magnets and to pickup loops in these magnets. In this way, backgrounds due to the fields and their time derivatives in these magnets can be reduced substantially. With digital averaging over many cycles and additional subtraction of the signal background without beam, currents down to a few nA can be measured. An example is given to the left in fig. 3.33 [34].

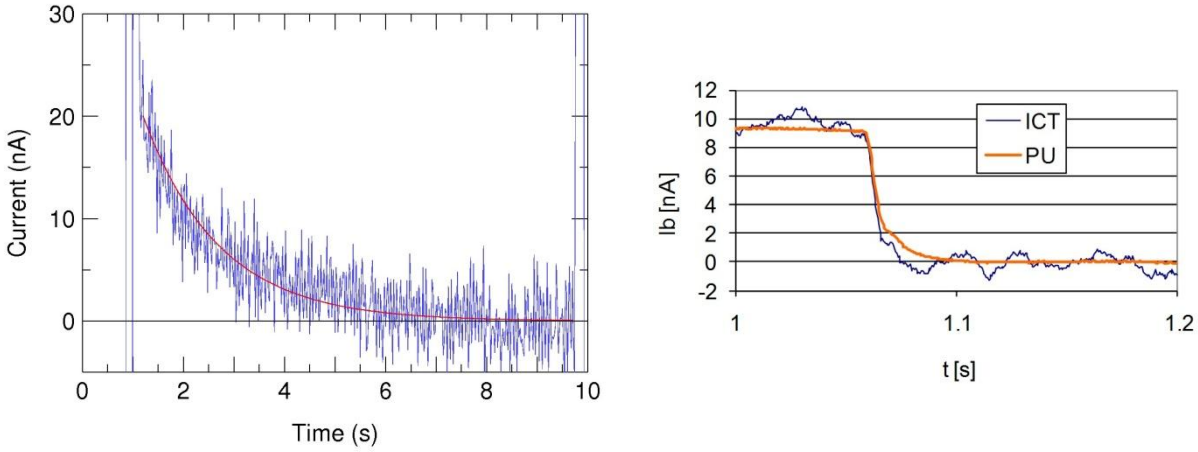

Fig. 3.33. Left: Decay of a 20-nA NH_4^+ beam measured with the DC current transformer, averaged over 120 machine cycles (the red curve is a fitted exponential). Right: Measurement of a bunched CD_3CND^+ beam with the ICT using 16 averages (blue), where a pickup signal (red) simultaneously is calibrated to the current measurement (after 1.06 s, the RF is turned off and the signal goes away).

For low beam currents, there is also an AC beam transformer, Integrating Current Transformer (ICT), from Bergoz of type ICT-178-090-10:1. This device has a current noise related to the input of the ICT of approximately 1 nA rms at 20 Hz bandwidth. For even lower currents, the current of a bunched beam is measured with the ICT at the same time as the sum signal from an electrostatic pickup. The pickup signal is calibrated to the ICT signal, and absolute currents down to 100 pA can be measured. This technique has been used for many dissociative-recombination experiments where the beam current must be reduced to very low values in order to avoid pile-up in the detectors [35]. One such case is illustrated to the right in fig. 3.33.

CRYRING has one horizontal and one vertical diagnostic kicker which can be used for, e.g., tune measurements. These consist of a pair of rectangular plates, 75 mm long and 55 mm apart which can be connected either in sum or difference mode, producing a longitudinal or a transverse kick. The kickers are driven by transistor amplifiers providing up to ±100 V with a bandwidth of 3 MHz.

REX-type beam viewers [27, 28] are not in regular use at CRYRING, although a prototype has been constructed and tested [36]. The main reason for this work has been the future use of these viewers for the DESIREE project at MSL [36, 37], but they could also be useful for diagnostics in the beam lines at FLAIR thanks to their high sensitivity, wide dynamic range, technical simplicity and their relatively low cost. They consist of a metal plate at a negative potential of a few kV that emits secondary electrons when hit by the ion beam, see fig. 3.34. These electrons are accelerated towards a thin grid at earth potential. Most of the ions will pass through the grid, which has a geometrical transmission of 95%, and impinge on two stacked multi channel plates (MCPs). Depending on the voltage applied on the MCPs, the electrons are amplified with a factor that can reach up to 10^6. The electrons produced by the MCPs are further accelerated towards a fluorescent screen and the light emitted by the screen is registered by a video camera. The viewer has been tested with low energy argon ions and protons, and by varying the voltage on the MCPs, beam currents from a few μA down to 10 fA could be detected. The weakest beam that was observed during these tests, a pulsed beam of 5 keV protons with a pulse width of 1 ms, corresponding to 60 protons, could easily be seen using an MCP voltage close to the maximum that can be applied.

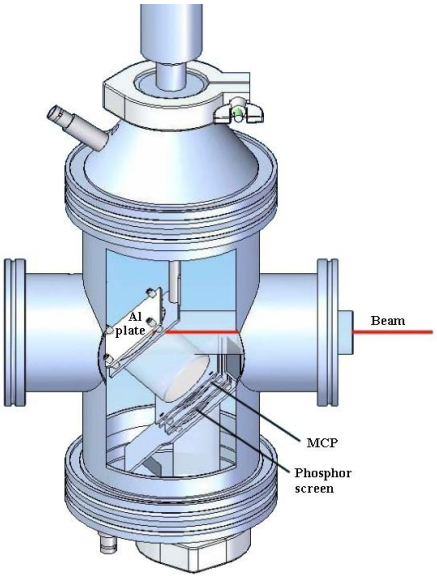

Fig. 3.34. Drawing of REX-type beam viewer, where the beam comes in from the right, hits an aluminium plate and produces electrons that are amplified by MCPs and detected on a phosphor screen.

3.13. Main-Magnet Power Converters

The CRYRING main power converters supply main dipole magnets, focusing and defocusing quadrupole magnets and electron cooler solenoids and toroids. The installation is fed from a 10.5 kV, 50 Hz line, and the major components are a 10.5 kV transformer for the dipole converter (DPS), a 10.5 kV / 400 V transformer, switchgear at 10.5 kV and 400 V, a harmonic filter to reduce the 10.5 kV waveform distortion, the DPS, the converters for focusing (QFPS) and defocusing (QDPS) quadrupoles and the electron cooler converter (ECPS). A photograph of the dipole converter is seen in fig. 3.35.

The power converters are current-stabilized and cycle between flat-bottom currents and peak currents according to an external digital reference waveform which is followed with a precision of up to 1×10^{-4} of actual value and a delay of around 4.5 ms (for the ECPS the numbers are 1×10^{-3} and 7.5 ms). Each converter is water cooled, has input power transformers, 12-pulse thyristor rectifiers followed by a damped LC lowpass filter (passive filter) and, except for the ECPS, a transistor series-injected active filter. The DPS is directly fed from 10.5 kV ac whereas the QFPS, QDPS and ECPS are fed via a the common 10.5 kV / 400 kV transformer. The three-phase, three-branch harmonic filter is connected to the 10.5 kV distribution system and is tuned to the 11^{th}, 13^{th} and 23^{rd} harmonics of the mains frequency. A schematic overview of the installation is seen in fig. 3.36.

Fig. 3.35. Photograph of dipole power converter (and control cabinet of electron cooler power converter to the left).

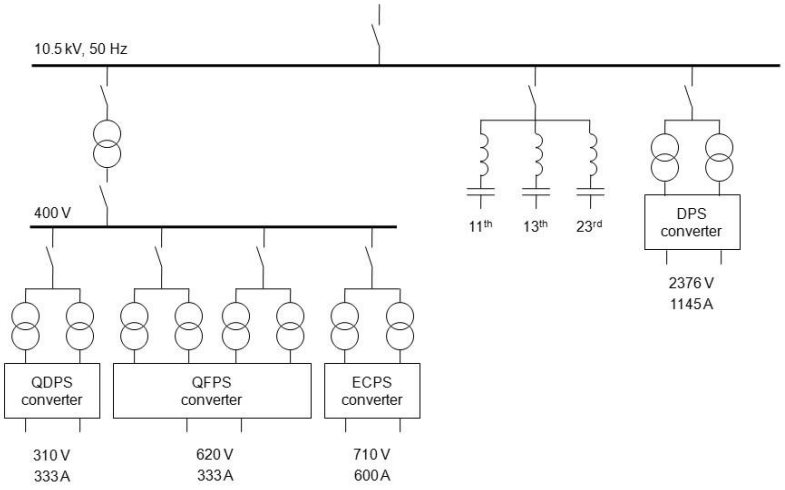

Fig. 3.36. Schematic diagram of the installation for the CRYRING main magnet power converters. Voltages are maximum resistive plus reactive voltages during ramps, and currents are nominal flat-top values.

Special measures to reduce the counter-reaction on the 10.5 kV grid include two thyristor bridges on the DPS, one high-voltage rectifier system and one low-voltage system. In the high-voltage or fast mode, the maximum output voltage is 2390 V, allowing the dipole magnets to ramp up or down in 150 ms. In the low-voltage or slow mode, a ramp to or from full current can be made in 1 s or more. There are additional taps on the 10.5 kV transformer, allowing a semi-fast ramp, which was added in case the disturbance on the grid would turn out to be too high in spite of the filters, and there is also a possibility to run in a low-range mode with maximum current 240 A for higher stability at low dipole currents. Neither of these two options is expected to be of interest at FLAIR.

The maximum current 1145 A delivered by the dipole converters gives the nominal maximum rigidity of 1.44 Tm of CRYRING. The minimum current is at present hardware-limited to 40 A, giving

theoretically a field strength $B = \mu_0 NI/d$ = 0.045 T and a rigidity $B\rho$ = 0.054 Tm. Below this limit, the current ripple increases and the stability decreases due to the small firing angle of the thyristors.

For the quadrupoles, with their lower currents and inductances, the fast ramp can be made with a single bridge. The QFPS is built as two power converters in series, each one identical to the QDPS. There is no control electronics installed to run the two halves separately, but if such electronics is added, the quadrupoles can be split into two families that are controlled separately, allowing more freedom to find working points for special purposes. The ECPS can ramp with 1600 A/s up to 240 A and with 540 A/s between 240 and 600 A. The harmonic filter is an impedance parallel to the 10.5 kV grid. It is a short-circuit at 550, 650 and 1100 Hz which are typical frequencies where a 12-pulse rectifier causes perturbations. At 50 Hz, the filter impedance is capacitive, giving a 380 kvar reactive power load. The output characteristics of the converters are summarized in table 3.6.

	Dipoles	Quadrupoles	Electron cooler
Nominal flat-top current	1145 A	330 A	600 A
Minimum flat top/bottom duration	50 ms	50 ms	50 ms
Ramping time/rate	150 ms or ≥ 1 s	150 ms or ≥ 1 s	1600/540 A/s
Stability at flat top/bottom	10^{-4}	10^{-4}	10^{-3}
Stability during ramps	10^{-3}	10^{-3}	10^{-2}

Table 3.6. Output characteristics of the main power converters. For the electron cooler, the ramp rate is 1600 A/s up to 240 A and 540 A/s above that. The stability, as specified by the manufacturer, is given as a fraction of actual values.

The complete installation sketched in fig. 3.36 was delivered by Holec Projects B.V. Holec no longer deals with this kind of equipment, but support is still given by Imtech Vonk, where the key persons behind the CRYRING installation are now employed. It is thus perfectly feasible to dismount the equipment at MSL and rebuild it at FAIR, and also to perform adaptations that are needed for, e.g., the higher grid voltage at FAIR, c.f. section 4.4.

3.14. Power-Converter Ripple

Ripple on the magnetic field of the main ring magnets, i.e. on dipoles, quadrupoles and sextupoles, can cause variations in the intensity of slowly extracted beams. In section 6.6.2.6, the sensitivity to dipole and quadrupole ripple is investigated numerically, and it is also argued that sextupole ripple is much less serious.

Dipole and quadrupole ripple have been measured using windings on the magnet yokes. The voltage over these windings is proportional to dB/dt, and after an integration over time, $B(t)$ is obtained. This method is much more sensitive than measuring the ripple directly on the coil current since the induced voltage signal does not have a dc component. For the dipole measurements, the existing backleg winding on one of the magnets was used. The integrated voltage could be calibrated to the field in the magnet gap by ramping the magnets between fields that are measured with a dc gaussmeter or known from previous measurements of field strength vs. coil current (see fig. 3.12). Additional measurements on the dipole magnets were made with a standard gaussmeter equipped with an ac probe. The quadrupole magnets do not have backleg windings, and instead a thin copper wire was wound some

tens of turns around the yoke for the purpose of these measurements. Since the flux in the quadrupole yokes is smaller than that in the dipole yokes by more than an order of magnitude, the background noise was higher in the quadrupole measurements. In an attempt to suppress some of the background, two wires were wound around opposite sides of the quadrupole yoke, where the fluxes are in opposite direction, and the voltage was measured over the two windings in series. The voltage was calibrated in the same way as for the dipoles.

Fig. 3.37 shows the results of measurements on the dipole magnets. The upper plot covers two 50-Hz periods. The blue curve of that plot shows the voltage picked up from the 30 turns of the backleg winding when the magnet current was constant at 57 A, corresponding to 300 keV antiprotons. It is dominated by short spikes at 600 Hz frequency deriving from the switching of the thyristors in the 12-pulse power converter. The red curve shows the time integral of the voltage divided by the 30 turns of the winding, producing the flux in the yoke (plus a constant of integration). The voltage spikes have both positive and negative components (not resolved in the plot), and when they are integrated, the resulting flux variations have a quite small amplitude of approximately 0.2 μWb. This of similar magnitude as the wiggles seen in the red curve over time scales of a few ms, where the dominating frequency is found to be 150 Hz when a Fourier transform is made of the flux curve. The total ripple amplitude is thus estimated to be 0.4 μWb at 57 A. The flux also shows a general, slowly increasing trend. This is due to an offset of unknown origin in the voltage measurement and is further discussed below.

The lower part of fig. 3.37 shows the voltage and flux, measured in the same way as in the upper plot, when the dipoles are ramped through a standard ring cycle which always goes from a minimum current of 40 A, through the desired current of 57 A in this case, up to the maximum value of 1070 A and back again. From this plot it is found that 57 A corresponds to a flux of 16 mWb. Consequently, the dipole ripple at the field required for 300 keV antiprotons has a relative amplitude of approximately 2.5×10^{-5}. The approximately constant thickness of the blue curve is an indication of the fact that the amplitude of the voltage spikes is relatively constant over the entire range of magnet current, and the ripple amplitude is also quite independent of magnet current.

Using a gaussmeter with an ac probe it could be confirmed that the relative field fluctuations on time scales from tens of ms to many seconds were in the order of, at most, 1×10^{-5} and that the increasing flux seen in the upper part of fig. 3.37 indeed is an artefact of the integration. The stability over even longer timescales can best be judged from the stability of the Schottky frequency of stored particle beams, in particular when ordered ion beams are observed, where the Schottky peak is very narrow [38]. Also here, the stability was found to be better than 1×10^{-5} and often closer to 1×10^{-6} although this was at the maximum dipole field. According to the numerical calculations in section 6.6.2.6, a dipole ripple of this magnitude will not influence the stability of the extracted beam intensity in any significant way.

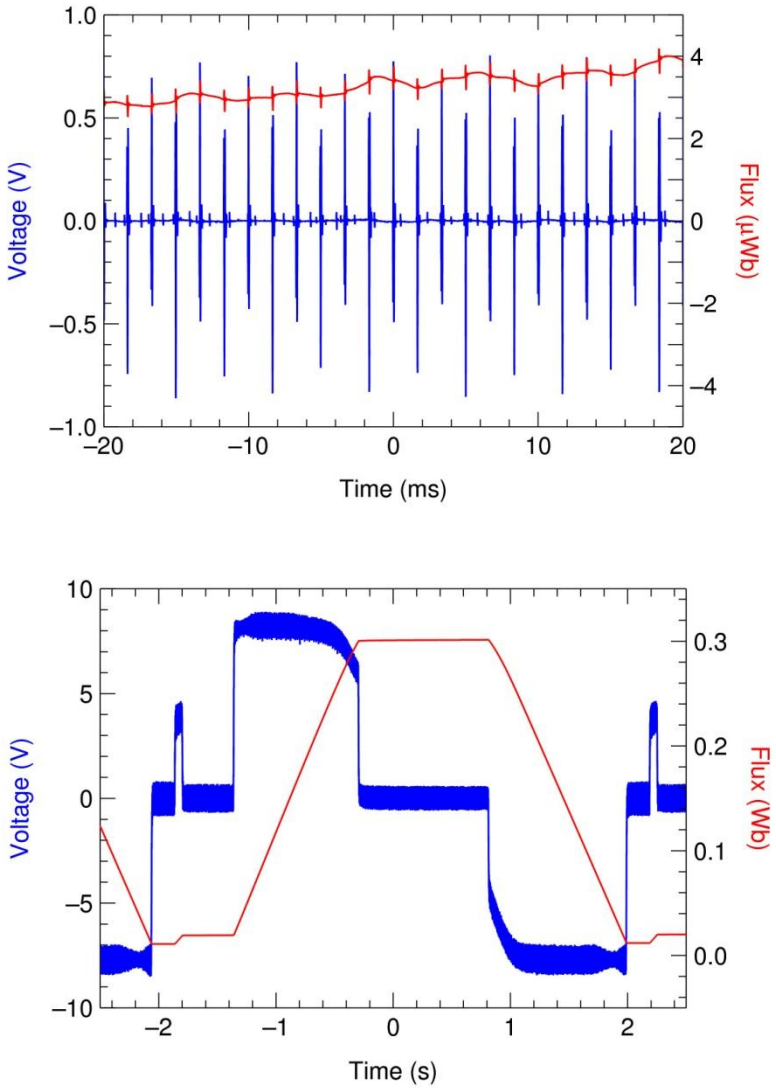

Fig. 3.37. Voltage over the backleg winding (left scale, blue) and the flux through the magnet yoke (right scale, red; see text concerning slope of curve) of a dipole magnet as a function of time when the current is constant at 57 A, corresponding to 300 keV antiprotons (upper plot), and when the field is ramped from a minimum of 40 A, through 57 A, up to a maximum of 1070 A and back again (lower plot). The flux is offset by an undetermined integration constant although the lower plot is adjusted by hand so that zero flux approximately corresponds to zero magnet current.

In fig. 3.38, the voltage over the wire wound on the yoke of a defocusing quadrupole is shown together with the flux through the yoke (which is half of the flux through a pole), still for a current corresponding to 300 keV antiprotons. Also here, the voltage signal is dominated by the thyristor spikes, but in the flux, mainly harmonics of 50 Hz are seen. Calibrating the flux to a ramp similar to the one in the lower part of fig. 3.37, it is found that the absolute ripple amplitude of 0.09 μWb corresponds to a relative amplitude of 2.8×10^{-4}. This is much higher than the dipole ripple due to an active filter of simpler construction. The ripple on the focusing quadrupoles, where the power converter in principle is two units of the same kind as used for the defocusing quadrupoles connected in series, was measured in the same way, and the ripple amplitude was found to be essentially the same.

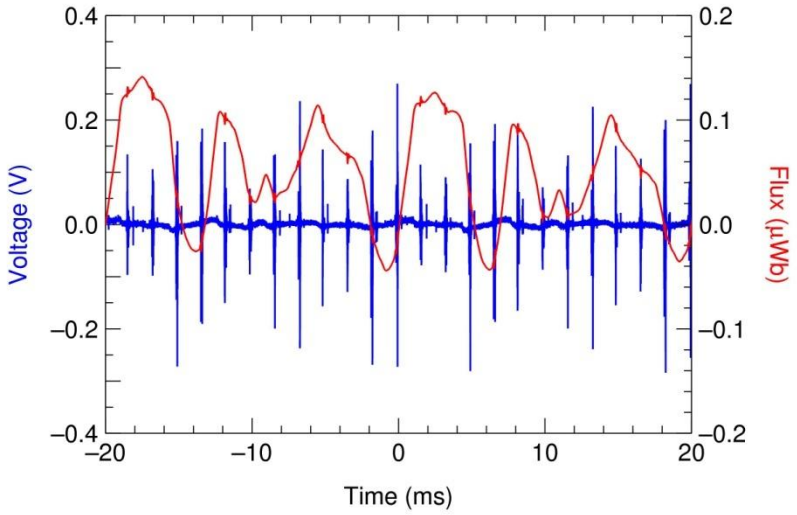

Fig. 3.38. Voltage over the coil wound on yoke of a defocusing quadrupole (left scale, blue) and flux through the magnet yoke (right scale, red) at 8.6 A magnet current, corresponding to 300 keV antiprotons. The flux is offset by an undetermined integration constant.

The amplitude of the Fourier transform of the flux in the quadrupole yoke is shown in fig. 3.39. It is seen that the two largest frequency components are at 100 and 150 Hz, with smaller components at 50 Hz and some of its lower harmonics up to 600 Hz. From the tracking calculations of section 6.6.2.6 it is clear that a quadrupole ripple of the magnitude observed in these measurements will cause a more or less 100% modulation of the extracted beam intensity. It is also demonstrated that it is possible to counteract the quadrupole by intentionally adding ripple on a single correction dipole. The Fourier spectrum of the quadrupole flux shows that such added ripple will need to have several frequency components between 50 and 600 Hz. Two additional remarks are that it ought to be investigated whether the quadupole power converters can be fine-tuned to reduce the ripple at this rather low current and that a very unstable grid, perhaps with other large pulsed loads, may cause further variations in dipole or quadrupole currents.

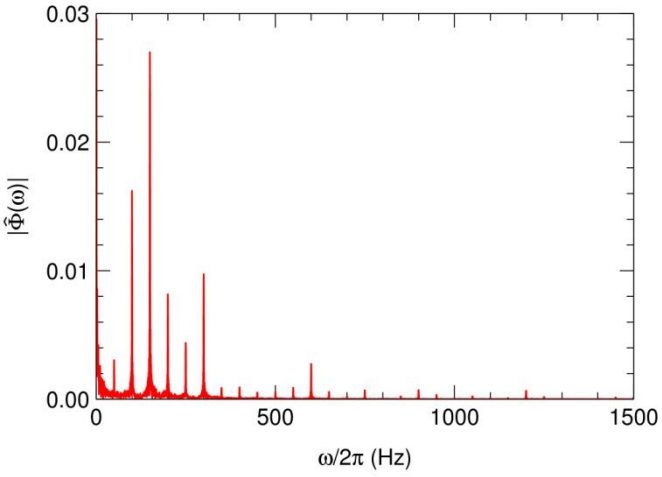

Fig. 3.39. Fourier transform of the quadrupole flux plotted in fig. 3.38, where the two largest frequency components are at 100 and 150 Hz.

3.15. Controls

On the hardware side, the control of power supplies, diagnostics hardware, etc. at CRYRING are essentially unchanged since the start of the project [39]. It is based on CAMAC and the G64 bus system. The computer system and the software, which essentially was copied from LEAR, were replaced some years ago by a modern PC-based system developed at Aarhus University [40]. Although it is expected that both hardware and software for controls will be different at FAIR, a short account of the present control hardware is given here as a basis for the adaptation to a new system.

The common control system hardware interface for accelerator equipment at CRYRING is the G-64 bus system. It is a modular computer system in European standard mechanics. At CRYRING a G-64 system typically contains a CPU card with a Motorola 6809 8-bit microprocessor, a DAC card, an ADC card, a digital I/O card, a digital function generator and a card for communication with the next higher level of the control system. It also contains some interfacing electronics like driver circuits, optocouplers, protection circuits etc.

The typical G-64 system then has three different channels for communication with the higher levels of the control system. The CPU has a serial bi-directional interface for receiving DAC data for the ”static” mode of operation, explained below, and commands for switching the connected power supplies on and off etc. This interface is also used for returning ADC data and device status information. In addition to this, the digital function generator has its own serial interface for receiving programming data, and it also has inputs for synchronisation pulses from the CRYRING timing system.

Since the beginning the CRYRING control system uses CAMAC for communication between the G-64 systems and the control computer level. A CAMAC serial loop distributes the control system to six CAMAC crates in various locations. These crates then act as a nodes with connections to a number of G-64 systems via special CAMAC modules, designed and manufactured by CERN. Each of the three communication channels described above uses its own type of CAMAC module. In later years, most of the CAMAC modules for communication with the CPUs in the G-64 systems have been replaced by standard Ethernet RS-232 serial ports. The serial CAMAC loop is however still used for downloading functions into the function generators and for synchronising the function generators with the timing system.

CRYRING uses GFD digital function generators designed at CERN. A GFD can be programmed to produce a function consisting of up to 256 linear segments, each segment having a duration of between 2 and 2048 ms. The output of the GFD is a sequence of 16-bit words, which normally are fed into a DAC in the G-64 system as most power supplies have analogue control inputs. The standard GFD is designed to produce a single function output, in order to control a single power supply. It is used in the cases where a power supply has its own G-64 unit. In many cases it is desirable to have a cheaper and more compact solution where one G-64 unit can control a number of power supplies. For this purpose there is a special multiplexed version of the GFD. The multiplexed GFD runs 8 functions at the same time and gives at its output connector both the number of the function, 0 ... 7, and its current value. It then scans round the functions in a circular manner. The output is connected to a demultiplexer which separates the function values into 8 output registers which then can feed 8 different DACs.

All power supplies that need to change their output to follow the ring cycle are controlled by the programmable function generators, GFDs. In CRYRING there is also a possibility to set every such supply in "static mode" as an alternative to the GFD-controlled "ramped mode". In static mode the supply is controlled from the control system via an output register. The switching between static and ramped modes is done in the G-64 units for each supply individually. There are command bits sent from the higher levels of the control system to the G-64 units to switch between the two modes, and there are status bits read back to show the settings. With some exceptions the G-64 systems are connected to the CRYRING timing system only through the function generators, which have input connectors for start, stop, hold and release events.

Another, but simpler, special G-64 module used at CRYRING is the BCD timer. It is an MSL-designed delay unit with TTL pulse inputs and outputs. The delay of the output signal from the input signal and the width of the output signal can be set in the range between 1 μs and 999.999 ms with a resolution of 1 μs.

Standard analogue interface signal levels are 0 – 10 volts for unipolar signals, but 0 – 5 volts can also appear. Standard levels for bipolar signals are ±10 volts or ±5 volts.

The G-64 systems normally have MSL-designed interface cards with optocouplers for digital I/O signals, both for outgoing command signals and incoming status signals. The interfaces for the ring dipoles and quadrupoles and for the electron cooler main magnet have a different design where the optocouplers are at the receiving side, regardless of the signal direction.

The CAMAC and G-64 systems are now since long obsolete, and for a number of years it has been regarded as desirable to avoid new investments in those systems when additions to the CRYRING control system have been made. The standard choice for installations without the need for function generators has then been fieldbus systems from Beckhoff, connected to the local area network. The fieldbus systems in that way replace the G-64 systems, and the local area network replaces the serial CAMAC loop.

3.16. Alignment

The alignment of CRYRING is thoroughly described in ref. [41]. The main dipole magnets were aligned with respect to their gaps before vacuum chambers were installed. Vertical positions were adjusted using an optical leveling instrument while horizontal distances to the centre of the ring and between adjacent dipoles were measured using an ISETH Distometer from KERN together with invar wires. The Distometer or its invar wire was attached to aluminium plates temporarily mounted in the magnet gaps. The distance measurements were calibrated off-line using a laser interferometer. Quadrupoles were adjusted in height and roll again using a target installed in the gap and the leveling instrument while they were positioned horizontally using the neighbouring dipoles as secondary standards. The alignment accuracy achieved for the dipoles was 0.03 mm vertically and 0.12 mm horizontally, and for the quadrupoles 0.07 mm vertically and 0.21 mm radially were achieved. The electron cooler, electrostatic pickups, etc,. were aligned with somewhat lower accuracy.

In order to allow a survey of the magnet positions after the vacuum chambers have been installed, there are alignment targets attached on the top of the dipole magnets, see fig. 3.40. These have central

8.02 mm diameter holes for attachment of suitable alignment devices. The quadrupoles have grooves in the laminations where alignment devices can be fitted as seen in fig. 3.41. There is also a pair of targets on the electron cooler. The positions of these alignment target with respect to the magnet gaps have not been accurately measured, so the targets can at present only be used to detect relative changes in magnet positions.

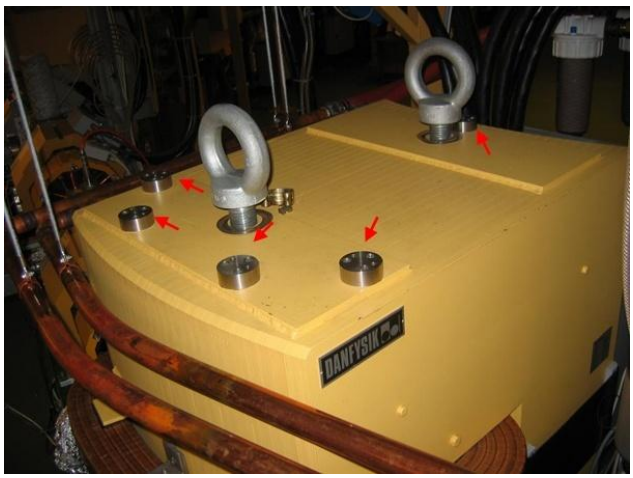

Fig. 3.40. Alignment targets on top of dipole magnets.

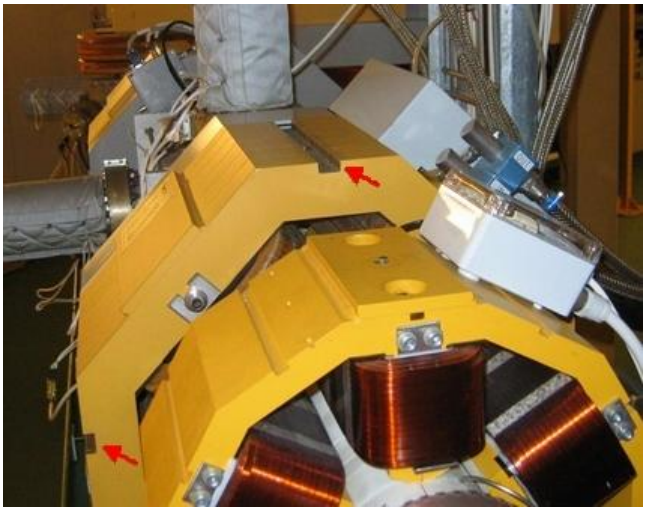

Fig. 3.41. Grooves on quadrupole magnet where close-fitting rods can be attached for alignment.

It is not expected that the alignment methods used at the time when CRYRING was built will be employed at FAIR. Instead it is suggested that the LSR ring be aligned with the same methods that will be used for the other machines at FAIR, i.e., probably using laser trackers. Then it should be rather straight-forward to relate the position of the magnet gaps to the alignment targets on top of the dipole magnets and to those that should be installed in the grooves on top of the quadrupoles, and these could then be used for the final alignment and also for future surveys. One may consider whether to combine the alignment with a simple field measurement to account for the displacement of the dipole field relative to the iron of up to 0.4 mm as mentioned in [41].

3.17. Operations and Instrumentation

This section describes some aspects of the operation of CRYRING with the purpose to give a hint on the requirements on instrumentation and other resources at the LSR. It is clear, however, that CRYRING today is used in a way which is quite different from the way it will be used at FAIR. At MSL, CRYRING has been running with different ions every week, and often with several different ion species in one week. A large part of the daily or weekly effort has thus been to produce these different beams from the ion sources, transporting them into the ring, storing them and usually accelerating them. The variations in mass and energy have been large, and many of the ion species have been difficult to produce in the ion sources, so that it has been necessary to handle very weak beams.

Table 3.7 lists all ions that have been stored in CRYRING, but in the following only the beams of singly charged ions from the MINIS source, corresponding to the low-energy injector at FAIR, are considered.

Once a beam has been extracted from the ion source and the proper mass has been selected in the analyzing magnet after the source, it is transported through the RFQ through optimization on intensity only. The intensity is measured on Faraday cups with sensitive amplifiers (see section 3.12). Between the RFQ and the ring, the beam is centered in the three quadrupole doublets by minimizing the movement of the beam spot on three corresponding downstream fluorescent screen when the quadrupole currents are changed. This can be done manually or, preferably, with an application software that guides the operator through the procedure. In the case of beams that are too weak to be seen on the fluorescent screens, this centering procedure can be performed with a "pilot beam" of another species with the same or nearly the same mass that can be formed with higher intensity. After some intensity optimizations near the entrance to the ring, the beam is transported 5/6 of a full turn in the ring to a Faraday cup on the S6 section. Here again intensity optimization is made, either manually or with another software application that tweaks all relevant power-supply knobs in sequence, round after round, while reading the current in the Faraday cup until the intensity has reached a maximum.

When this Faraday cup is pulled out and the rf is switched on, a circulating beam can with some luck be seen on a spectrum analyzer connected to an electrostatic pickup. Intensity and lifetime optimization is again made by tweaking power-supply knobs in a sequential manner. In most cases the beam is then accelerated, the exception being the singly charged atomic ions used for laser-spectroscopy experiments. Acceleration ramps for main dipoles, focusing and defocusing quadrupoles, rf frequency and rf amplitude are calculated by software and sent to the power supplies. These ramps are calculated from the charge-to-mass ratio of the ions and the desired final energy and are based on a combination of theory and experience. With some luck again, the ramps are good enough for a beam to be seen on the flat top immediately, but more often the ramps have to be adjusted by hand in order to get the beam all the way to the final energy. After optimizing the intensity once more, the electron beam may be turned on, and the electron energy is adjusted together with steering coils in the cooler until a good beam cooling is observed. At this point the beam is handed over to the users.

Singly charged positive atomic ions	H^+, D^+, $^3He^+$, $^4He^+$, $^7Li^+$, $^9Be^+$, $^{11}B^+$, $^{12}C^+$, $^{14}N^+$, $^{16}O^+$, $^{40}Ar^+$, $^{40}Ca^+$, $^{45}Sc^+$, $^{48}Ti^+$, $^{56}Fe^+$, $^{83}Kr^+$, $^{84}Kr^+$, $^{86}Kr^+$, $^{88}Sr^+$, $^{129}Xe^+$, $^{131}Xe^+$, $^{132}Xe^+$, $^{138}Ba^+$, $^{139}La^+$, $^{142}Nd^+$, $^{151}Eu^+$, $^{197}Au^+$, $^{208}Pb^+$
Multiply charged positive atomic ions	$^4He^{2+}$, $^{11}B^{2+}$, $^{12}C^{2+}$, $^{12}C^{3+}$, $^{12}C^{4+}$, $^{12}C^{6+}$, $^{14}N^{2+}$, $^{14}N^{3+}$, $^{14}N^{4+}$, $^{14}N^{7+}$, $^{16}O^{2+}$, $^{16}O^{3+}$, $^{16}O^{4+}$, $^{16}O^{5+}$, $^{16}O^{8+}$, $^{19}F^{5+}$, $^{19}F^{6+}$, $^{19}F^{9+}$, $^{20}Ne^{2+}$, $^{20}Ne^{5+}$, $^{20}Ne^{6+}$, $^{20}Ne^{7+}$, $^{20}Ne^{10+}$, $^{28}Si^{3+}$, $^{28}Si^{11+}$, $^{28}Si^{14+}$, $^{32}S^{5+}$, $^{36}Ar^{9+}$, $^{36}Ar^{10+}$, $^{36}Ar^{12+}$, $^{36}Ar^{13+}$, $^{40}Ar^{7+}$, $^{40}Ar^{9+}$, $^{40}Ar^{11+}$, $^{40}Ar^{13+}$, $^{40}Ar^{15+}$, $^{48}Ti^{11+}$, $^{58}Ni^{17+}$, $^{58}Ni^{18+}$, $^{84}Kr^{33+}$, $^{126}Xe^{36+}$, $^{129}Xe^{36+}$, $^{129}Xe^{37+}$, $^{136}Xe^{39+}$, $^{136}Xe^{44+}$, $^{207}Pb^{53+}$, $^{208}Pb^{53+}$, $^{208}Pb^{54+}$, $^{208}Pb^{55+}$
Singly charged positive molecular ions	H_2^+, HD^+, H_3^+, D_2^+, H_2D^+, $^3HeH^+$, $^3HeD^+$, $^4HeH^+$, D_3^+, He_2^+, LiH_2^+, D_5^+, BH_2^+, CH_2^+, CH_3^+, CH_4^+, NH_2^+, OH^+, CH_5^+, NH_4^+, H_2O^+, H_3O^+, HF^+, ND_3H^+, CD_5^+, ND_4^+, D_3O^+, C_2H^+, CN^+, $C_2H_2^+$, HCN^+, $C_2H_3^+$, $HCNH^+$, $C_2H_4^+$, CO^+, N_2^+, $^{13}CO^+$, N_2H^+, $C_2H_5^+$, $H^{13}CO^+$, NO^+, $D^{13}CO^+$, CH_3O^+, CF^+, O_2^+, $CH_3NH_3^+$, CH_3OH^+, $CH_3OH_2^+$, $H_2O_2^+$, H_2S^+, CD_3O^+, PD_2^+, $N_2H_7^+$, $D_2{}^{32}S^+$, $CD_3OH_2^+$, CD_3OD^+, $H_5O_2^+$, $D_2{}^{34}S^+$, $D_3{}^{32}S^+$, $CD_3OD_2^+$, $^{13}CD_3OD_2^+$, $D_3{}^{34}S^+$, $C_3H_4^+$, $D_2{}^{37}Cl^+$, $D_5O_2^+$, CH_3CNH^+, $C_3D_3^+$, $N_2D_7^+$, N_3^+, $C_3H_7^+$, NaD_2O^+, CH_3CHO^+, CO_2^+, HCS^+, $C_2H_5O^+$, DN_2O^+, $C_2H_5OH^+$, CO_2D^+, $C_2H_5OH_2^+$, CD_3CDO^+, $NO^+ \cdot H_2O$, O_3^+, $DCOOD_2^+$, $CD_3OCD_2^+$, $C_3D_7^+$, CF_2^+, $NO^+ \cdot D_2O$, DC_3N^+, $CD_3OCD_3^+$, $N_3H_{10}^+$, DC_3ND^+, $CD_3ODCD_3^+$, $H_7O_3^+$, COS^+, $N_2O_2^+$, $CH_3OCOH_2^+$, $D_7O_3^+$, $N_3D_{10}^+$, $C_4D_9^+$, $S^{18}O_2^+$, ArN_2^+, $H_9O_4^+$, $CD_3COHNHCH_3^+$, $CD_3CONHDCH_3^+$, $C_6D_6^+$, $PO^{37}Cl^+$, $C_6D_7^+$, $H_{11}O_5^+$, $C_2S_2H_6^+$, $C_2S_2H_7^+$, $H_{13}O_6^+$, $PO^{35}Cl_2^+$
Multiply charged positive molecular ions	N_2^{2+}
Negative atomic ions	H^-, Li^-, F^-, Si^-, S^-, Cl^-, Se^-, Te^-
Negative molecular ions	CN^-, C_4^-, Si_2^-, Cl_2^-
Energy per nucleon	38 eV/u – 92 MeV/u
Total energy	5 keV – 1.4 GeV

Table 3.7. Ion species stored in CRYRING, often accelerated and in almost all cases used for physics experiments.

Normally only the five parameters already mentioned are ramped, plus the electron energy in case the users want to measure recombination as a function of energy. Sextupoles and correction dipoles are adjusted to maximize the intensity on the injection energy but they are typically not needed for the accelerated beam, so they are left on their injection values throughout the machine cycle. The cooler magnets and if possible the electron current are also on the same value throughout the cycle. The focusing effect of the electron beam at injection is then compensated for by adjusting the quadrupoles. The reason why it is avoided to ramp the cooler parameters is that this tends to change the vacuum in the cooler and make the conditions for recombination experiments time-dependent.

For some experiments, more elaborate machine cycles must be used. One example is where intensity is accumulated from several injection pulses using cooler stacking before the beam is accelerated. Then the beam is cooled both at injection energy and at the flat top, requiring that several parameters of the electron cooler, both coil currents and voltages on the gun and collector side, must be ramped. Also, the settings of the beam at injection energy are more critical. Another case is acceleration of protons with their low rigidity at the injection energy. Then some sextupoles and/or correction dipoles may have to be ramped in order to compensate for eddy currents in the dipole vacuum chambers.

The experience in setting up the acceleration ramps makes it unnecessary to measure tunes or the closed-orbit position, and intensity optimization has turned out to be sufficiently powerful to obtain beams that in most cases are limited by the intensity from the ion source. It should be understood, however, that the cross sections and recombination rates for most processes studied in CRYRING are relatively large, and measurements are relatively fast. It is thus seldom worth while to spend a large fraction of a day on improving the beam intensity by small factors. This will become different at FLAIR, in particular when running antiprotons, and it may then pay off to spend more time and care on using beam diagnostics to reduce losses to a minimum.

4. Status and Modifications of CRYRING

4.1. Introduction

As mentioned in the introduction, CRYRING has many features that make it very suitable as a deceleration ring for antiprotons and ions at FAIR. These features include:

- CRYRING has been in production runs at magnetic rigidities between 0.079 Tm and 1.44 Tm, corresponding to (anti)proton energies between 300 keV and 96 MeV, and this exceeds the energy range of 300 keV to 30 MeV required for FLAIR.

- The ring has been running for experiments both in acceleration mode and deceleration mode, and machine tests described in section 7 demonstrate deceleration of protons through the entire range from 30 MeV to 300 keV.

- The ramping of the ring magnets is quite fast. In the slow ramp mode normally used for experiments, acceleration is performed in 1 s through the entire energy range, and the control of the power converters is symmetrical such that deceleration can be made in the same time. (In the tests of section 7 , the deceleration was made in 1.8 s to facilitate the tuning.) There is also a fast ramp mode where acceleration/deceleration take place in 125 ms. In either case, the fast ramping ensures a high throughput of particles.

- The ring has efficient electron cooling as shown in the tests described in section 7. Cooling times of antiprotons injected from the NESR ring are expected to be in the order of 1 s or less. Highly charged ions will cool still faster. The cooler is at present equipped with a superconducting gun solenoid, and a beam expansion with a factor 100 is normally used. It has been decided to keep this gun solenoid for FLAIR because of the proven high cooling rates and a possible future use in recombination measurements with high resolution. A disadvantage with the superconducting solenoid is the additional complexity of keeping it cold with liquid helium, and also the strong magnetic field in combination with the small electron gun limits the maximum cooling energy as discussed in section 3.11. The previously used normal-conducting gun solenoid together with electron guns made for 1 and 10 times expansion will therefore be included in the transfer to FAIR. It is expected to be straightforward to use these instead if it will turn out that a change is desirable.

- As discussed in section 3.10, CRYRING has a very good vacuum. The pumping is to a large extent based on NEG (Non-Evapourable Getter) pumps, and a true average pressure of H_2 has been measured to be 3×10^{-11} mbar. This ensures that the storage lifetime of antiprotons will be more than sufficient, and that also highly charged ions can be decelerated to low energies.

Still, there are a number of upgrades and modifications that must be made to the ring. Upgrades are necessary for some components which are outdated or otherwise unsuitable for transfer to FAIR, and these are discussed in the section 4.3. Major modifications are few and concern only injection and extraction.

In addition, it will have to be considered how the LSR will be interfaced to the surrounding infrastructure at FAIR. Generally speaking, it has been stated by MSL since the transfer of CRYRING to FAIR was first proposed that the ring will provided such as it has looked when it has been in

operation at MSL. Exceptions and additions have been specified to the FLAIR collaboration (see Appendix 1 and 2). In particular, MSL cannot take responsibility for connecting the LSR hardware to the FAIR control system, to safety interlocks that may be required or to cooling water, pressurized air, etc. An intermediate position is here taken by the main magnet power converters. These are expected to be disassembled by a company related to the original supplier, and some investigations on how to adapt these to the conditions at FAIR have already started as discussed in section 4.4.

4.2. New Ring Layout

When the ring is rebuilt at FLAIR as the LSR ring, its layout must be modified with respect to the present one in order to fit the constraints of the FLAIR building and the geometry of incoming and outgoing beamlines. Those beamlines are shown in fig. 2.1, and an example of a constraint imposed by the building (according to current plans) is that only the part of the LSR hall which is towards the bottom of fig. 2.1 is accessible by an overhead crane, and it is therefore suitable to put the electron cooler there.

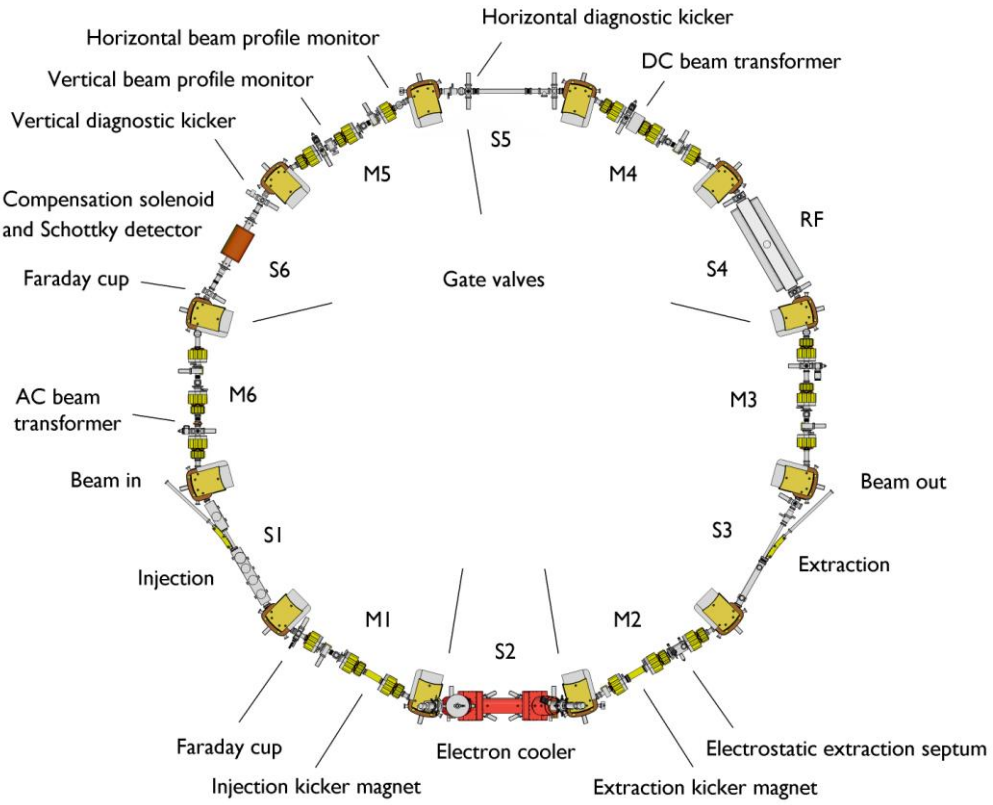

Fig. 4.1. Layout of LSR at FLAIR, where positions of major components are indicated.

The new layout is shown in fig. 4.1. For the purpose of the discussion in this section, the 6 superperiods in the new layout are indexed 1–6 according to the figure, and each one is divided into a magnet straight section M and a magnet-free section S. The magnet section is divided in Ma between the bending magnet and the first quadrupole, Mb between the first and second quadrupoles, Mc between the second and third quadrupoles, and finally Md between the third quadrupole and the dipole.

The same labelling is used for the present layout at MSL, with superperiod 1 still starting at the injection straight section.

The major components of the different LSR superperiods are described in the following list, and a summary of the layout is found in table 4.1.

LSR superperiod 1: The injection section will be completely new, as discussed elsewhere. The new injection kicker magnet will be installed after the defocusing quadrupole, in M1c.

LSR superperiod 2: This is the only place where a crane will be available and thus this will be the new position for the electron cooler. The dipole chamber after the cooler is different from the other dipole chambers with multiple ports for the installation of detectors for ions that have changed their charge state in the cooler. This chamber should be replaced by the original one, which is similar to the other dipole chambers in the ring.

The fast extraction kicker magnet has to be installed between the first two quadrupoles, where there presently are two correction dipoles. The horizontal correction magnet on this straight section in CRYRING will be moved upstream before the first quadrupole magnet and the vertical one downstream to the beginning of S3.

The electrostatic extraction septum will be installed after the defocusing quadrupole.

LSR superperiod 3: S3 will house the new extraction. First on S3 is the vertical correction magnet and next is the extraction septum magnet.

LSR superperiod 4: S4 will be used for the RF section, without changes compared to CRYRING.

The DC beam current transformer will be installed after the defocusing quadrupole in M4c.

LSR superperiod 5: S5 will contain a diagnostic kicker and two electrostatic pickups but is otherwise available for future experiments.

LSR superperiod 6: The compensation solenoid and the Schottky detector should be located in the straight section S6. The AC beam transformer will be in M6c, which in LSR is a more favourable position than in CRYRING since it is further away from the RF which gives lower background.

LSR will be divided into five vacuum sectors. Each sector will be separated by all-metal gate valves and contains an ion pump, a vacuum gauge, and an angle valve that can be used for pumping down and leak testing. These will be mounted together in a unit which in the table below is referred to as a "pump unit" There will also be a large number of NEG pumps. There will be six NEG units per magnet section and where possible a similar number on the other straight sections.

Section	Components
S1	New injection system
M1a	Faraday cup
M1b	Horizontal and vertical correction dipoles
M1c	Injection kicker magnet
S2	Gate valve, electron cooler, gate valve
M2a	Horizontal correction dipole
M2b	Extraction kicker magnet
M2c	Electrostatic extraction septum
S3	Vertical correction dipole, extraction septum magnet, two electrostatic pickups
M3b	Horizontal and vertical correction dipoles
M3c	Pump unit
M3d	Gate valve
S4	RF
M4b	Horizontal and vertical correction dipoles
M4c	DC beam transformer, pump unit
S5	Horizontal diagnostic kicker, gate valve, two electrostatic pickups
M5a	Horizontal beam profile monitor
M5b	Horizontal and vertical correction dipoles
M5c	Vertical beam profile monitor, pump unit
S6	Vertical diagnostic kicker, compensation solenoid, Schottky detector, Faraday cup
M6a	Gate valve
M6b	Horizontal and vertical correction dipoles
M6c	AC beam transformer, pump unit

Table 4.1. Summary of the layout of the straight sections in LSR. Each magnet section in addition has a pair of electrostatic pickups inside quadrupole magnets.

4.3. Upgrades and New Equipment

Most of the components of CRYRING are in good condition after almost 20 years of operation. This applies to magnets, vacuum system, electron cooler, many power supplies, etc. Upgrades or replacements are needed for components that have reached an age where it is difficult or impossible to find spare parts or where the cost of maintenance is comparable to the purchase of new equipment. Also equipment that is unreliable and where faults occur frequently should be upgraded, but there are no significant problems of this kind at present.

As specified in the offer from MSL to the FLAIR collaboration (see Appendix 1), some of these upgrades will be performed by MSL before the transfer of CRYRING to FAIR. Others—mainly replacements of power supplies—will have to be made by the FLAIR collaboration, since it has not been considered meaningful to purchase power supplies just to put them in storage for many years.

Upgrades performed at MSL before the transfer to FAIR concern the following items:

- The ion source platform will be rebuilt with a new support frame, new cabling, new power supplies and a new safety interlock system.

- An ion source dedicated for H^- will be installed on the platform. This ion source will be tested on the new platform before transfer to FAIR.

- Baking jackets made from ceramic paper will be replaced by an insulation material that is based upon glass fibre.

Equipment that need to be replaced, but where the FLAIR collaboration will have to be responsible for the replacements are:

- New current supply for the analyzing magnet after the ion source. This supply should be able to provide 7 A if only (anti)protons or H^- are to be used. In CRYRING, singly charged molecular ions up to 208 mass units have been injected from this platform, requiring 200 A, as, for instance, from a Danfysik 8500 series supply.

- High-voltage supplies for the electrostatic elements and current supplies for magnets in the injection line, c.f. table 3.2.

- The drive amplifier of the RFQ transmitter is equipped with glass tubes that have limited lifetime are increasingly difficult to obtain. This stage should thus be replaced by a modern solid-state 2-kW amplifier (c.f. fig. 3.5). The two vacuum tubes in the final stage (EIMAC 4CX12000A) have a lifetime of around 15 000–20 000 hours and have been used for 10 000 hours. It is planned to send the two tubes that were previously in use to EIMAC for refurbishment, and these will be supplied as spares with the amplifier. Two power supplies for the filament currents of the EIMAC tubes are old and somewhat difficult to adjust and should be replaced.

As seen in Appendix 1, the estimated cost for the FLAIR collaboration to make these replacements was estimated to be 387 k€ in 2005 prices.

The new installations needed for injection and extraction are described in sections 5 and 6. Major pieces of new equipment are:

- Septum magnets for injection and extraction

- Current supplies for the septum magnets, one of which will be a Foeldi supply recovered from CELSIUS.

- Vacuum tank for the injection straight section with electrostatic deflector and kicker plates for the multiturn injection.

- Vacuum tank for the extraction septum magnet and for adjacent parts of the extraction straight section

- Electrostatic septum with its vacuum tank.

- Kicker magnets for injection and extraction with pulse supplies.

- Ceramic vacuum chambers for the kicker magnets.

These items will be provided by MSL, except for one septum-magnet current supply (the one needed in addition to the Foeldi supply). Originally it was foreseen that also this one would be purchased by MSL, but with the delays of the FLAIR project this must be postponed for the same reason of long storage time as mentioned above and in Appendix 2.

In addition, the dipole vacuum chambers before the extraction and after the injection must be modified to increase their horizontal aperture by increasing the horizontal diameter of the pipes coming in and out of the chambers from 100 mm to 150 mm. This will be done by MSL. Also, the present large dipole chamber that has been installed after the electron cooler is suggested to be replaced with the original chamber as mentioned in section 3.10.

4.4. Main Magnet Power Converters

The main magnet power converters, i.e., those supplying the main dipoles, quadrupoles and the electron cooler, were delivered as a single package by Holec B.V. Some upgrades, improving their reliability, have been performed by MSL during the time since their delivery. These include the replacement of ageing ±5 V / ±15 V supplies and an improvement of the protective circuitry for the active filter where relays were replaced by faster CMOS switches.

More importantly, there is a difference between the present installation and that at FAIR in that the voltage of the grid coming in to MSL is 10.5 kV while it will be 20 kV at FAIR. As described in section 3.13, there is a specially designed 10.5-kV transformer for the dipole converter, a more regular 10.5 kV / 400 V transformer and a harmonic filter connected to the 10.5 kV grid. The 10.5 kV / 400 V transformer can be replaced by one going from 20 kV at a relatively modest cost, and the harmonic filter may not be needed at FAIR, since load variations from other installations at FAIR are in any case expected to be large compared to those from the LSR. The dipole transformer, which is oil-immersed, will be more costly to replace, however, and as an alternative, an intermediate transformer from 20 kV to 10.5 kV could be installed.

The issue about how to adapt the installations to the FAIR grid voltage has been discussed with the group responsible for power installations at GSI and with Imtech Vonk who are expected to be contracted for the transfer of the converters to FAIR.

5. Design of Injection

5.1. Introduction

5.1.1. Injection at CRYRING

At present, CRYRING has a nominally 10-turn horizontal electrostatic multiturn injection, designed to match the injectors that existed or were foreseen at the time of the conception of the CRYRING facility. The main focus was on the EBIS source that then was in operation, and a small source for light singly charged ions was also included in the project, but mainly for test purposes. It was therefore chosen to inject through an RFQ that took particles from 10 keV per nucleon, given by the ion-source platforms, to 300 keV per nucleon. The RFQ can accelerate particles with charge-to-mass ratios q/A above 0.25. For highly charged ions this means q/A between 0.25 and 0.5, and in additions protons or H^- can be accelerated. Highly charged ions accelerated in the RFQ are thus injected into the ring at a magnetic rigidity between 0.16 and 0.32 Tm while protons or H^- are injected at 0.079 Tm.

Already from the beginning there were also plans to add injection of other kinds of ions, i.e. those with q/A less than 0.25, directly from a high-voltage platform, without using the RFQ. Here, the range of rigidities depends both on platform voltage and on q/A, and if these can be chosen freely, the only restrictions are given by what the ring can accept. These plans were realized when the small test source was rebuilt and used for a programme of atomic and molecular physics with singly charged atomic and molecular ions, including quite heavy species up to masses above 200. Also an ECR source on a 300-kV platform was added to the facility.

Given the range of magnetic rigidities of the ring and the properties of the RFQ and of the high-voltage platform, the combinations of beam energy and charge-to-mass ratio accepted by the ring can be illustrated in a diagram like in fig. 5.1. Here, constant beam rigidities correspond to diagonal lines with one slope and constant platform voltages to diagonal lines with another slope. Note that the low-rigidity limit is somewhat soft, since remanence effects and hysteresis in the magnets become increasingly severe when the rigidity decreases below that of 300 keV (anti)protons, and also the ripple of the power converters increases on a relative scale. At present, the low-current limit of the dipole converters corresponds to $B\rho$ = 0.054 Tm or 0.038 $B\rho_{max}$ or 140 keV (anti)protons, not taking remanence and hysteresis into account.

The same diagram will be valid for ions from the low-energy injector at FLAIR. The RFQ will still inject protons or H^- ions at 300 keV. With an ECR source on a high-voltage platform, all charge states (i.e., all ions with $q/A < 0.5$) can be injected at a rigidity no smaller than that of 300 keV protons without use of the RFQ if the platform voltage is at least 150 kV. If the RFQ is used to accelerate the ions which have q/A between 0.25 and 0.5, the platform voltage can be reduced to 75 kV. The shaded gray area in the diagram shows, as another example, which area can be reached if ions are injected from a platform at 100 kV, without the RFQ being used, and then accelerated in the ring. The upper part of the area with gray stripes indicates injection below the rigidity of 300 keV protons. Here, longer setup times and/or larger particle losses at injection can be expected compared to injection at higher rigidities.

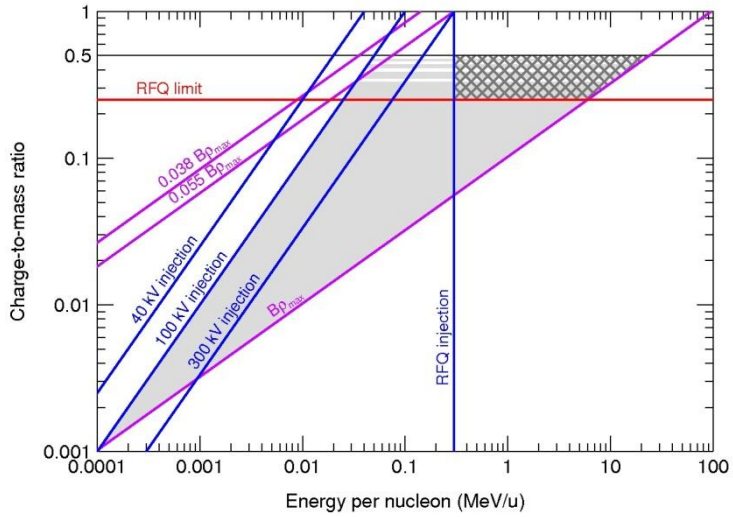

Fig. 5.1. Diagram showing what combinations of energy per nucleon and charge-to-mass ratio that ions stored in CRYRING can have. Injection from the RFQ takes place on the vertical blue line and above the red line representing the lowest charge-to-mass ratio that the RFQ can accelerate. Injection from a high-voltage platform takes place on one of the diagonal blue lines, depending on the platform voltage (three different voltages are shown as examples). The diagonal pink lines show the maximum rigidity $B\rho_{max}$ of 1.44 Tm, and the minimum setting of the dipole supplies give a minimum rigidity of 0.054 Tm or 0.038 $B\rho_{max}$. However, hysteresis and remanence effects in the magnets make operation below 300 keV (anti)protons, corresponding to 0.079 Tm or 0.055 $B\rho_{max}$ and the third pink line, increasingly difficult. As an example, acceleration of ions from a 100-kV platform produces beams within the shaded, gray area. The upper part is more difficult to reach since the injection rigidity becomes lower than 0.055 $B\rho_{max}$, and this is indicated by gray stripes. Acceleration of ions by the RFQ produces beams within the cross-hatched area. With deceleration, the complementary areas from the injection line down to the minimum rigidity are reached instead.

5.1.2. Injection at FLAIR

At FLAIR, particles can be injected into the LSR either from the dedicated low-energy injector according to the diagram in fig. 5.1 or from the NESR at a fixed energy of 30 MeV for antiprotons and at the same rigidity as 30 MeV antiprotons for ions. The beamlines from NESR and from the low-energy injector will be merged upstream of LSR such that all beams will use the same injection system in LSR. The possibility to do multi-turn injection of low-energy particles will be maintained, but the multi-turn injection will be combined with a fast single-turn injection for the NESR beams. A CAD model of the LSR injection straight section is seen in fig. 5.2.

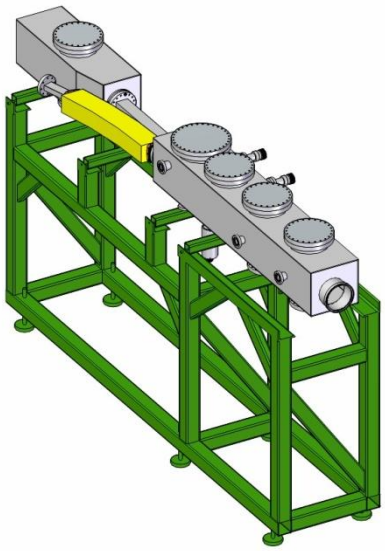

Fig. 5.2. CAD model of the new injection straight section with electrostatic deflection plates for the multi-turn injection inside two vacuum chambers separated by the septum magnet in yellow.

The electrostatic multi-turn injection stacks the beam in horizontal phase space, using a closed-orbit bump local to the injection straight section that decreases to zero over ten turns. The system in CRYRING today consists of an electrostatic septum and four pairs of deflector plates that produce the closed-orbit distortion. This is illustrated in fig. 3.17. In order to combine this with the injection from NESR, the electrostatic septum has to be replaced by a magnetic septum to achieve sufficient bending power, and to compensate for the larger thickness of the magnetic septum, two additional deflection plates are needed as shown in fig. 5.3. The fast injection from NESR uses, in addition to the magnetic septum, a kicker magnet to align the injected beam with the closed orbit.

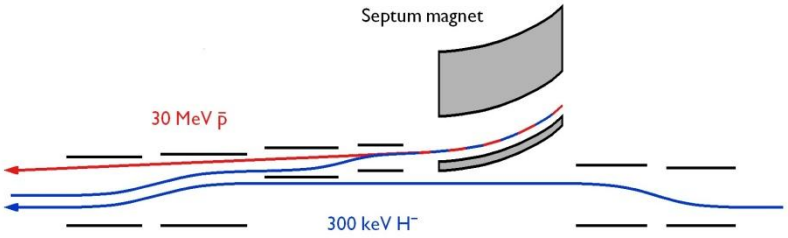

Fig. 5.3. Birds-eye view of the injection section for, as examples, kicker injection of 30 MeV antiprotons (red) and multiturn injection of 300 keV H^- ions (blue, two turns are shown schematically). The scale in the direction transverse to the beam is exaggerated for clarity.

5.2. Position of Septum and Kicker Magnets

At the septum magnet, the injected beam enters the ring at a certain horizontal displacement from the closed orbit. The purpose of the deflection plates of the multi-turn injection and of the kicker magnet of the fast injection is to align this beam with the closed orbit. In the case of the fast injection, a beam

that is displaced at the septum magnet will cross the closed orbit, such that it can be aligned with it by a deflection in a kicker magnet, if the difference in betatron phase between the septum and the kicker is $\pi(n+1/2)$ where n is an integer. The longitudinal positions of the septum and the kicker magnets are in addition constrained by the space available in the ring while the horizontal displacement of the septum, and thus of the injected beam, is constrained by the acceptance needed for the circulating beam.

5.2.1. Longitudinal Position of Septum and Kicker Magnets

There are at least three partially conflicting requirements on the longitudinal position of the injection septum magnet: There must be sufficient space on both sides for the deflection plates of the multi-turn injection, it must not be too close to the dipole magnet before the injection straight section to avoid a too big deflection angle, and there is an optimal position relative to the kicker magnet in order to obey the $\pi(n+1/2)$ condition of the betatron phase difference.

As a result of these considerations, the geometry of fig. 5.4 is chosen. The beam in the injection beam line then comes as close to the ring dipole magnet at the start of the injection straight section as it is today at CRYRING. The fringe field of the dipole magnet has a noticeable effect on the beam in the injection line today, but the effect can easily be compensated for with steering magnets in the injection line.

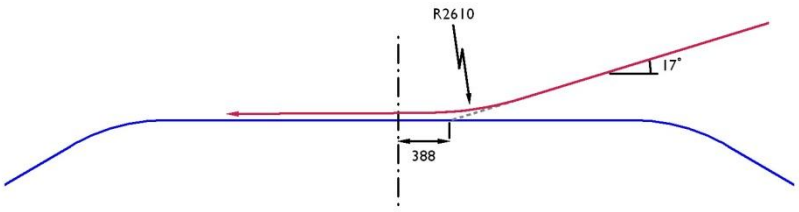

Fig. 5.4. Geometry of the beam injection, showing the position and angle of the beam in the injection beamline (red) relative to the closed orbit in the ring (blue). The NESR beam comes in at an angle of 17 degrees to the injection straight section, bends with radius 2413 mm through an angle of 16.81 degrees and leaves the septum magnet with an angle of 0.19 degrees and at an offset of 52 mm (see sections 5.4.1 and 5.2.2) from the closed orbit. The beam from the low-energy injector has a larger emittance and must come in at a 5 mm larger distance from the septum coil compared to the NESR beam, and it is thus translated 5 mm upward in the figure, exiting the septum magnet at 57 mm offset from the closed orbit.

Fig. 5.5 shows the betatron phase advance as a function of position over one superperiod relative to the centre of a magnet-free straight section and for the working point $Q_x = 2.42$, $Q_y = 2.42$, which is the standard working point in CRYRING, and which is also foreseen when using the fast injection. With the septum magnet positioned close to the centre of the injection straight section, it is seen that the betatron phase has advanced by $\pi/2$ approximately in the space between the last quadrupole of the following straight section and the dipole magnet at the end of that section. However, this space is too short for a kicker magnet, and it will instead be positioned in the space after the defocusing quadrupole and the adjacent defocusing sextupole. It will be placed symmetrically in this drift section which has 624 mm nominal length, c.f. fig. 3.1.

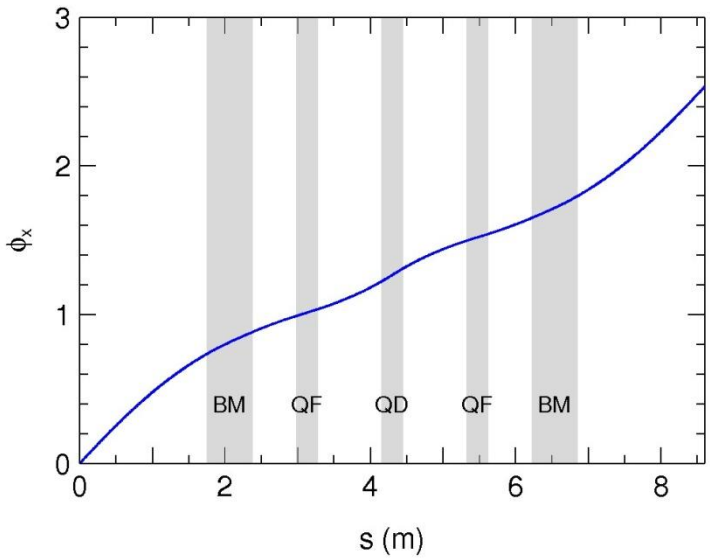

Fig. 5.5. Betatron phase advance for the working point $Q_x = 2.42$, $Q_y = 2.42$ that will be used for the fast injection (and fast extraction). The shaded areas illustrate the position of dipole and quadrupole magnets (c.f. fig. 3.1).

5.2.2. Transverse Position of Magnetic Injection Septum

The transverse position of. the of the magnetic septum, i.e. its horizontal offset from the closed orbit, is a compromise between maximizing the horizontal acceptance for the circulating beam and minimizing the required strength of the kicker magnet and the deflectors that produce the closed-orbit bump for the multi-turn injection. There is also an influence from the extraction systems, since there is no point in having a larger acceptance in the injection straight section than in the extraction straight section (or vice versa). Furthermore, in the case of the fast injection, the beam on its first turn must not have a displacement in the first quadrupole magnet that is bigger than the radius of the vacuum chamber in this magnet, and this puts an upper limit on the transverse offset of the magnetic septum.

As a result of these deliberations, a suitable compromise if found to be that the inside of the magnetic septum as seen by the beam (i.e., inside vacuum) is positioned 25 mm outside the closed orbit. The horizontal beta function at the septum is 2.2 m, and taking the maximum particle displacement as 25 mm minus 5 mm to allow for magnet and alignment errors, a single-particle acceptance of 180 π mm mrad is obtained. Comparing with the value calculated in section 3.6, this is a reduction with about 30 %. Since it can be assumed that the beams injected from the NESR are relatively cold, a slightly reduced acceptance will be of no importance for deceleration of NESR beams. Only beams of large emittance from the low-energy injector may be affected, and here the maximum intensity may shrink somewhat compared to the situation at CRYRING today. According to section 5.5, the thickness of the magnetic septum (as measured in vacuum) is 22 mm. The width of the electrostatic septum channel is today 25 mm, but with the same argument about the relatively cold NESR beam, it will be enough with a 5 mm margin between the NESR beam in the septum channel and the septum-channel wall. The beam thus enters the ring at a displacement of 25 + 22 + 5 = 52 mm from the closed orbit. As seen in section 5.4.1, it also enters at an angle of approximately 7 mrad. The larger-emittance beam from the low-energy injector can enter the ring at a slightly larger displacement of 57 mm, leaving 10 mm margin to the septum-channel wall. This larger displacement for the low-energy beam

is possible since it uses the multi-turn injection which aligns the injected beam with the equilibrium orbit already on the injection straight section, eliminating the problem with the limited aperture in the quadrupole magnets.

5.3. Multi-Turn Injection

5.3.1. Multi-Turn Injection Subsystems

The beam steering for the multi-turn injection will be done with three different subsystems as shown in fig. 5.3.

1. Four pairs of electrostatic kicker plates move the closed orbit in the ring towards the septum. Before the injection starts, the closed orbit is moved outward so the incoming beam comes on the closed orbit, then the orbit is moved back to the original position during 10 turns, which takes 70 μs for a 300 keV (anti)proton beam.

   In CRYRING, there are two different bipolar power supplies, one for ions accelerated by the RFQ and one for slow heavy ions. The requirement for the first one is to give a linear ramp down from maximum ±30 kV to zero in 60–120 μs (for protons the voltage is ±8 kV). The second one is used for slow ions not accelerated by the RFQ, and it ramps down linearly from at maximum ±1 kV down to zero in up to a few ms.

2. The septum magnet, described in section 5.5, which needs to bend a beam with up to ten times lower magnetic rigidity than when it is used for fast injection.

3. Two pairs of electrostatic plates, to the left of the magnet in fig. 5.3. The pair to the left is the electrostatic septum, which is needed since the magnetic septum will be much too thick for multiturn injection. The first pair will move the beam towards the septum, and the septum will make the injected beam parallel with the circulating beam.

5.3.2. Four Electrostatic Kickers

The kickers all have different requirements on the apertures. From the right, i.e. in the direction of the beam, the first one needs the smallest aperture, in the second one needs room for the displaced closed orbit, the third and fourth kickers are similar to the first two, but also need to have room for the injected beam. Thus, all four ones will have different apertures, but for simplicity they should all be connected to the same pulsed high voltage supply. It is not sufficient to have the same ratio between length and gap, since fringe fields are important. Instead, calculations with SIMION have been performed on a simple variant of the injection chamber.

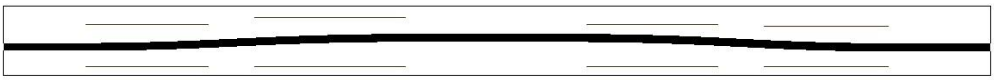

Fig. 5.6. Bump on the closed orbit in the beginning of the injection, ±4 kV gives a 21.5 mm bump. Only the four pairs of kicker plates are shown in this picture from a SIMION calculation. The septum magnet and the two pairs discussed earlier are not shown.

Kicker no.	Gap (mm)	Length (mm)	Deflection (deg.)
1	74	299	3.7
2	79	306	3.7
3	97	378	3.3
4	91	335	3.3

Table 5.1. Lengths and gaps of the four kickers, numbered from right to left, i.e. in the direction of the beam in CRYRING.

In CRYRING it has been possible to change the position of all the kicker plates with stepper motors, but since this system has been used only a few times, it has been decided to remove the motors and only keep the possibility to move the actuators manually.

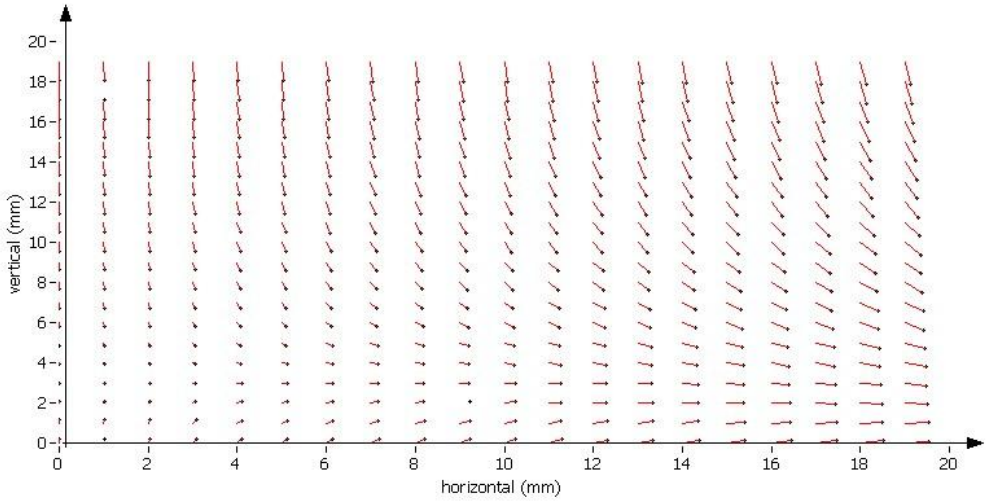

Fig. 5.7. Since the kicker plates have a finite size the field will vary with the transverse position. The figure shows the result of a SIMION run where this dependence is studied. In the beginning of the injection chamber, ions were created in a regular mesh with zero transverse velocity. In the chamber the closed orbit was moved 20 mm towards the septum and then back again. The difference between the transverse start and stop position is shown as a red line, with a black dot at stop. The chamber is modelled as shown in fig. 5.6.

After the septum magnet, the beam comes to two short steering pairs. These will be fed by DC voltages on the plates away from the circulating beam. The other ones will be on earth potential to minimize the disturbing effects on the circulating beam. It is of course necessary that both a low energy beam and a high energy beam can pass without hitting the plates as shown below with results from SIMION calculations.

5.3.3. Two Electrostatic Deflectors

In the new design of the injection chamber, two extra electrostatic deflectors after the magnetic septum are needed to accomplish multiturn injection for ions coming from the low-energy injector. The thickness of the septum inside vacuum is 20 mm, and these two pairs of deflection plates move the beam inwards, towards the circulating beam, by the same 20 mm.

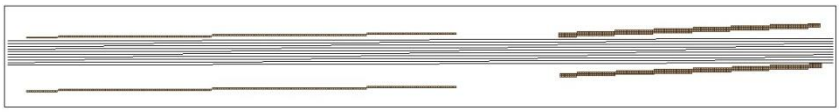

Fig. 5.8. SIMION calculation showing the path of a 30 MeV beam which not is affected by electrostatic bends. The apertures are 39 mm in the left pair, 27 mm in the right pair, and the resulting aperture as seen by the beam is around 18 mm. The actual beam size will be approximately 1 mm.

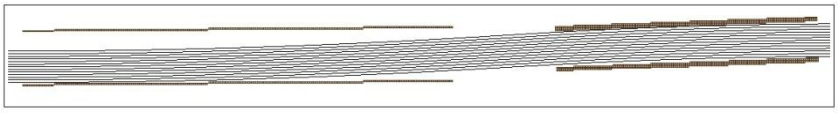

Fig. 5.9. A 300 keV/u beam is moved very close to the septum to enable multiturn injection. With +4 kV and –4 kV on the upper plates (in the figure) and earth potential on the opposite ones, the 25 mm wide proton beam seen in the figure can pass through without losses. A beam from the low-energy injector is in reality expected to have a size of 5–10 mm.

Fig. 5.8 shows the path of a high-energy beam where the deflector plates are not used as obtained from calculations with SIMION. Clearly, the available aperture is more than sufficient for a cooled beam coming from the NESR which is much smaller than the beam in the figure. Fig. 5.9 shows a beam from the low-energy injector, where a horizontal beam size of up to 25 mm can be accepted.

Two DC high-voltage supplies are needed for these deflectors, one positive and one negative. For protons, 4 kV is needed while particles with q/A=0.25 require 16 kV. For ions not accelerated in the RFQ, less than less than ±1 kV is sufficient.

5.3.4. Beam Parameters at Injection

A LabVIEW program has been written to simulate the multiturn injection, and one of its applications has been to find optimal beam parameters at the end of the injection beamline. This beamline is not yet designed, so the results show what one should aim for in the design. It is assumed that the beam from the RFQ has a (horizontal) emittance of 5π mm mrad and a relative momentum spread $\Delta p/p$ equal to ±0.01. The latter number is what is calculated for the RFQ without debuncher. With debuncher, the momentum spread should be reduced by a factor 2. The tune of the ring is Q_x = 2.43, which is the standard working point for CRYRING.

Table 5.2 shows the optimum values and an interval where the intensity is at least 95 percent of the maximum if only one parameter deviates from the optimum value, indicating how sensitive the injection is to the settings.

A limitation in the calculations is that RF capture is not included. To get complete results, the losses at the start of the acceleration should also be included. In CRYRING, it has been seen that there are rather large losses when the acceleration of an uncooled beam starts, and probably the lost ions are the ones with too large momentum deviation to be captured by the RF.

Parameter	Optimum value	95% interval
β_x	1.5 m	0.4 – 2.3 m
α_x	–0.3 m	–1.9 – 0.9 m
D_x	0.2 m	–0.15 – 0.35 m
position	2.8 mm	2.1 – 4.1 mm
angle	0.75 mrad	–0.4 – 2.0 mrad

Table 5.2. Optimum beam parameters at the end of the injection beamline. The 95 percent interval indicates where the intensity is at least 95 percent of the maximum if only one parameter deviates from the optimum value. The position is measured from the centre of the beam to the electrostatic septum and the angle is measured with respect to the closed orbit in the ring.

5.3.5. Simulation of Multiturn Injection

The multiturn injection itself was simulated by injecting groups of 1000 particles into the ring on ten consecutive turns, tracing them with MAD (with the lattice geometry defined as in table 3.3) from one turn to the next. The particles have an emittance of 5π mm mrad and a relative momentum spread $\Delta p/p$ equal to ±0.01, the tune is Q_x = 2.43, and the optimum beam parameters found in the previous section are used.

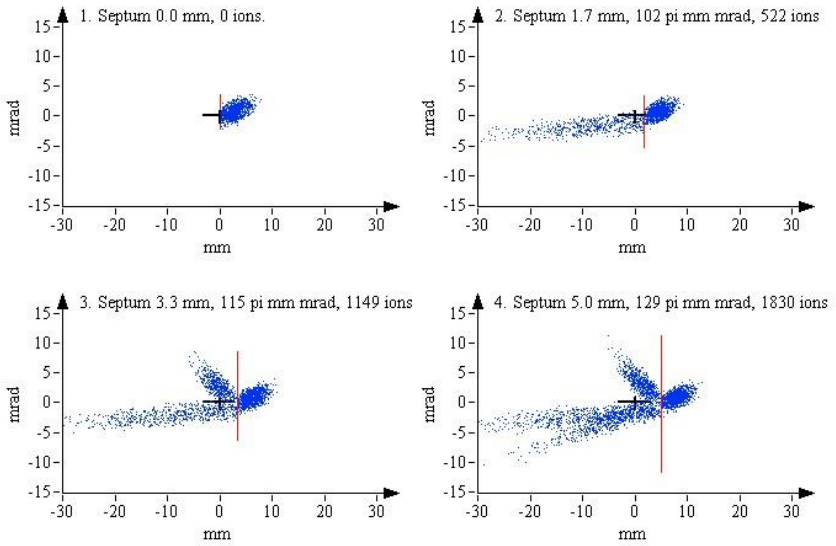

Fig. 5.10. Phase-space plots illustrating multiturn injection. The red line represents the septum, and the black cross indicates the position of the circulating beam's closed orbit. The closed orbit defines origin of the horizontal coordinate, and the coordinate of the septum increases during the injection process as the voltage of the electrostatic kickers shrinks to zero (although in reality it is of course the position of the closed orbit that changes while the septum is fixed). The first, upper left plot shows the incoming beam in the injection channel, while the following plots represent the situation one, two and three turns later, still with a beam in the injection channel. For each plot, the emittance of the beam inside the septum and the number of particles in this beam are indicated.

Fig. 5.10 shows, at the upper left, particles entering the ring in the injection channel, and in the other plots, the situation one, two and three turns later, with particles still entering. Due to the large momentum spread and the 1.6 m dispersion at the centre of the magnet-free straight section of CRYRING, the injected beam gets quite wide when it comes back, after one turn and a significant fraction of the particles hit the back of the septum. Therefore, the injection efficiency becomes quite low for the first turns.

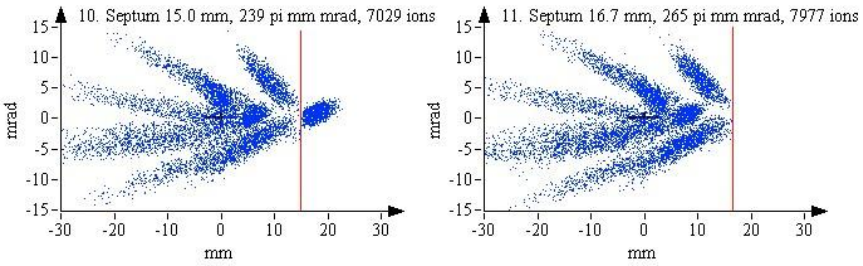

Fig. 5.11. Phase space at turns no. 10 and 11 where the injection pulse ends.

This is seen in fig. 5.11, depicting the beam in the ring at turn 10 and 11. At turn 11, the injection pulse has just ended, and 80% of the injected particles remain in the ring. The injection efficiency increases towards the end since the particles then are injected with a large positive displacement relative to the closed orbit and therefore come back with a large negative displacement, i.e., away from the septum, on the next turn due to the betatron motion.

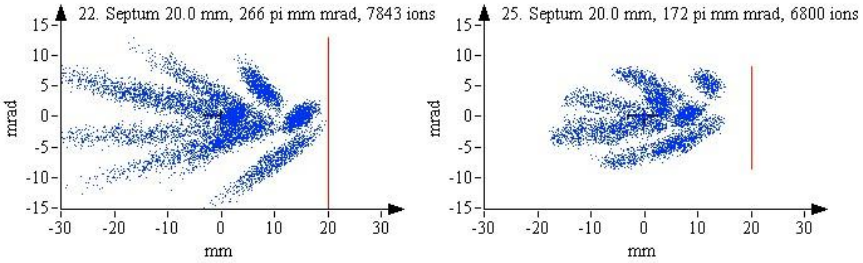

Fig. 5.12. Phase space at turn no. 22 and at turn no. 25 after removal of particles outside the ring acceptance.

Finally, fig. 5.12 shows the phase space at turn 22 and turn 25. In between these two plots, ions having a maximum amplitude in the direction opposite to the septum larger than 25 mm are removed, approximating the limit due to the horizontal acceptance of the ring. The number of particles remaining at the end are 6800, giving a total multiturn injection efficiency of 68 percent.

5.4. Single-Turn Injection

5.4.1. Deflection at the Kicker Magnet

In order to calculate the deflection required in the kicker magnet to align the injected beam with the closed orbit, and also to calculate the deflections at the electrostatic extraction septum or the extraction kicker, we use the solution $x(s)$ to Hill's equation for the horizontal motion and its derivative $x'(s)$ [18]:

$$x(s) = A\beta(s)^{1/2}\cos[\psi(s)+\delta]$$
$$x'(s) = -A\beta(s)^{-1/2}\{\alpha(s)\cos[\psi(s)+\delta]+\sin[\psi(s)+\delta]\}$$

With x and x' of a particle as well as β and α known at the position of the deflecting element (kicker magnet or electrostatic extraction septum, denoted by index d), the equations can be solved for A and the phase. The particle displacement at the magnetic septum (index m) is then found to be

$$x_\mathrm{m} = x_\mathrm{d}\frac{\beta_\mathrm{m}^{1/2}}{\beta_\mathrm{d}^{1/2}}\frac{\cos(\theta_\mathrm{d}+\Delta\psi_\mathrm{d\text{-}m})}{\cos\theta_\mathrm{d}} \tag{5.1}$$

$$x'_\mathrm{m} = -x_\mathrm{d}\frac{1}{\beta_\mathrm{d}^{1/2}\beta_\mathrm{m}^{1/2}}\frac{\alpha_\mathrm{m}\cos(\theta_\mathrm{d}+\Delta\psi_\mathrm{d\text{-}m})+\sin(\theta_\mathrm{d}+\Delta\psi_\mathrm{d\text{-}m})}{\cos\theta_\mathrm{d}} \tag{5.2}$$

where

$$\tan\theta_\mathrm{d} = -\frac{x'_\mathrm{d}\beta_\mathrm{d}}{x_\mathrm{d}} - \alpha_\mathrm{d}$$

and $\Delta\psi_\mathrm{d\text{-}m}$ is the change in the phase $\psi(s)$ from the deflecting element to the septum (with a suitable sign depending on whether the deflecting element comes after the septum as for the injection or before as in the case of the extraction). For a kicker acting on a transversally cold beam with small extension in x, such that we can set $x_\mathrm{d} = 0$, this simplifies to

$$x_\mathrm{m} = x'_\mathrm{d}(\beta_\mathrm{d}\beta_\mathrm{m})^{1/2}\sin\Delta\psi_\mathrm{d\text{-}m} \tag{5.3}$$

$$x'_\mathrm{m} = -x'_\mathrm{d}(\beta_\mathrm{d}/\beta_\mathrm{m})^{1/2}(\alpha_\mathrm{m}\sin\Delta\psi_\mathrm{d\text{-}m}-\cos\Delta\psi_\mathrm{d\text{-}m}) \tag{5.4}$$

Table 5.3 shows β and α at the septum magnet and the injection kicker as well as the betatron phase relative to the centre of the injection section for the standard working point of $Q_x = 2.42$, $Q_y = 2.42$. Setting $x_\mathrm{m} = 52$ mm in equations (5.3) and (5.4), the required deflection angle at the kicker becomes $x'_\mathrm{d} = 16.3$ mrad and the angle of the beam coming in at the septum must be $x'_\mathrm{m} = 3.4$ mrad.

	β [m]	α	$\Delta\psi$
Injection septum magnet	1.952	0.102	−0.102
Injection kicker magnet	5.187	−1.684	1.443

Table 5.3. Twiss parameters for working point used today at CRYRING, suitable for fast injection at LSR, with $Q_x = 2.42$, $Q_y = 2.42$.

The trajectory of injected particles from the septum to the kicker is shown in fig. 5.13. It is seen that the beam will enter the 100-mm-diameter vacuum chamber in the first quadrupole magnet at a displacement of approximately 43 mm, leaving an adequate 7-mm margin to the chamber wall.

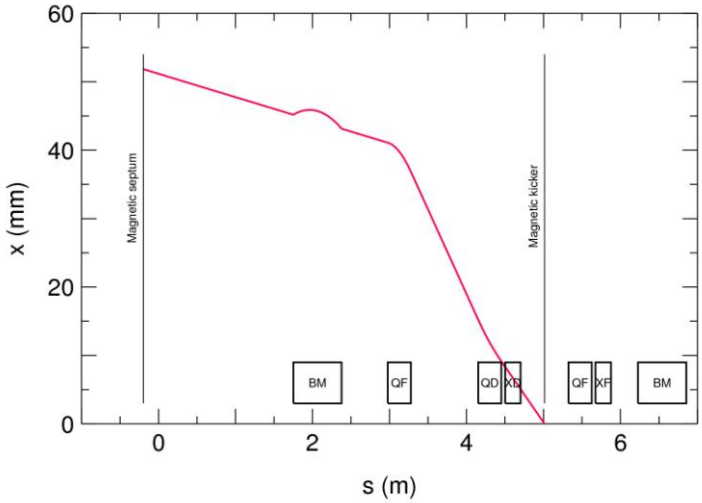

Fig. 5.13. Trajectory of injected particles starting in the injection channel at the exit of the magnetic septum and crossing the closed orbit at the position of the injection kicker at an angle of 16.3 mrad.

5.4.2. Rise Time, Pulse Length and Stability of Kicker Magnets

The cost and complexity of the kicker magnets depend strongly on the requirements on the time structure of the kicker pulse. The main parameters for the injection kicker are here fall time, maximum pulse duration and stability during the pulse (for the extraction kicker it is rise time instead of fall time that is important).

At the fixed injection rigidity of 0.80 Tm, corresponding to 30 MeV antiprotons, the fall time has to be shortest for the fastest particles which are the antiprotons themselves. Requiring that the injected bunch of particles can occupy 60% of the 51.63-m ring circumference, the minimum fall time of the injection kicker becomes 40% of the revolution period of 30 MeV antiprotons or 280 ns. The same arguments and the same numbers hold for the minimum rise time of the extraction kicker.

The maximum pulse duration for the injection kicker is given by the slowest particles that will be injected from the NESR. At the fixed rigidity of 0.80 Tm, these are the ions with the lowest charge-to-mass ratio foreseen, i.e., 1/4. Calculating again with a bunch length which is 60% of the ring circumference, a maximum pulse duration of 1.7 μs is obtained. For the extraction kicker, the slowest particles are defined to be ions with charge-to-mass ratio 1/4 at the rigidity of 300 keV antiprotons, giving a maximum pulse duration of 17 μs.

If the field in the injection kicker magnet is not constant during the pulse, an increase in the stored beam emittance will result. If the particle distribution in the beam is drawn in a diagram with axes x and $(\beta x' + \alpha x)$, a beam with emittance ε_1 can be represented by a circle with radius $(\beta\varepsilon_1)^{1/2}$. A particle getting an angular offset $\Delta x'$ due to an imperfect kicker field will be shifted by an amount $\beta\Delta x'$ along the vertical axis in the diagram. The superposition of the two circles can be approximated by an ellipse with axes $(\beta\varepsilon_1)^{1/2}$ and $(\beta\varepsilon_1)^{1/2} + \beta\Delta x'/2$ if $\Delta x'$ is small, and as a result the emittance increases from ε_1 to

$\varepsilon_2 = \varepsilon_1 + (\beta\varepsilon_1)^{1/2}\Delta x'/2$. At the injection kicker, β = 5.2 m, so if the emittance can be allowed to increase by a factor two, an angular error of 0.9 $\varepsilon_1^{1/2}$ can be allowed. The deflection in the kicker magnet is 16.5 mrad, so the relative angular error can be approximately 50 $\varepsilon_1^{1/2}$, and with an injected emittance of 1 π mm mrad, the relative stability of the kicker supply needs to be 5%. Undershoot, overshoot, etc. of the field decrease can be included in this value, as well as pulse-to-pulse variations and other irregularities. For the extraction kicker, pulse variations will instead affect the effective emittance of the extracted beam.

5.5. Injection and Extraction Septum Magnets

The injection and extraction will use C-shaped dc septum magnets with coils in air separating the circulating and injected/extracted beams. For economical and practical reasons, the two magnets will have the same dimensions although one will be the mirror image of the other. The geometry at the injection is more constrained because of the combination with multi-turn injection and thus determines the dimensions. To make room for the vacuum tank with kicker plates, the injection septum magnet must have a curved coil following the path of the injected beam. The magnets will have a bending radius of 2413 mm, and they will deflect the beam by 16.8 degrees. Their length, i.e. the length of the yoke, will be 674 mm projected on the ring straight section and 683 mm along the arc. Both magnets are designed for beam rigidities up to 0.80 Tm, corresponding to 30 MeV antiprotons, requiring a field strength of up to 0.33 T. The magnets will have an iron screen outside of the coil in order to reduce the stray field and its effect on the circulating beam as well as field clamps to shield the circulating beam from the ends of the coils. Procurement of these magnets was initialized at the end of 2010, and the data in this section are still preliminary.

A Foeldi current supply which has been used for a septum magnet at the CELSIUS ring has been provided to LSR by the The Svedberg Laboratory in Uppsala, and this supply can be used to power one of the magnets (a second supply needs to be purchased, c.f. section 4.3). The coils of the LSR septum magnets are designed to match the Foeldi supply, which is rated at 2 kA and 28 V, with a good margin.

The septum magnets are envisaged to be dc magnets, although made from laminated iron. The leakage magnetic field outside of the coil that exists in a non-ideal geometry, i.e., when the coil is not a homogeneous conductor covering the entire gap, when the permeability of the iron is not infinite, when the coil ends are taken into account, etc., is then particularly serious for the injection septum of a decelerating machine where the magnetic rigidity of the particles decreases relative to the injection value. For this reason, there is a screen of soft iron outside of the septum coil, and it is very simple to add a small a trim coil to further reduce the influence of the septum magnetic field on the circulating particles. There are also field clamps at the ends whose primary purpose thus is to sheild the circulating beam from the field of the coil ends, although they also produce a sharper definition of the fringe field along the injected/extracted beam. On top and bottom there are welded plates of solid iron for, e.g., attachment of eye bolts and support frame.

The septum coil is 7 mm wide including insulation (c.f. table 5.4). Outside of the coil, there is a 3 mm air gap, a 2 mm iron screen, a 2 mm air gap and the 3 mm thick vacuum-chamber wall. Inside of the coil, there is also a 2 mm air gap and a 3 mm thick chamber wall. As a result, the total thickness of the septum in vacuum is 22 mm. The path of the injected NESR beam is assumed to lie 5 mm inside the

chamber wall, while the larger-emittance beam from the low injector has a 10 mm margin to the chamber wall. Also the path of the extracted beam will have a 5 mm distance to the vacuum chamber. The width of the vacuum pipes inside the septum magnets will be 50 mm, and the total width of the gaps will be 81 mm.

For the calculation of the height of the magnet gap, it is assumed that the beam injected from the low-energy injector has a maximal vertical emittance of 50π mm mrad. The NESR beam will have a much lower emittance. Given the vertical beta function of 2.3 m at the position of the septum, a vertical aperture of the vacuum chamber inside the septum magnet of 24 mm will be sufficient even if alignment errors are taken into account. Adding the 3 mm thickness of the vacuum chamber wall and a 4 mm air gap, the septum magnet needs a gap height of 38 mm. This translates to a coil with 10 000 ampere-turns for 0.80 Tm rigidity assuming infinite permeability of the iron, or, adapting the coil to the 2 kA Foeldi supply, 6 turns and 1670 A at maximum field. The yoke and the coil are split in two halves, such that they can be fitted around the vacuum chamber.

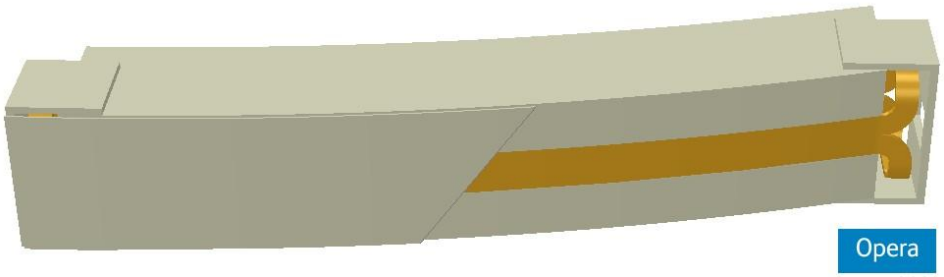

Fig. 5.14. Model from Opera-3d of the injection septum magnet with part of the soft-iron screen cut away.

Fig. 5.14 shows a 3d model of the magnet, and the cross section of the iron yoke is seen in fig. 5.15 together with field lines from two-dimensional Poisson calculations (where the curvature of the magnet thus is neglected). The average field in the back of the yoke is approximately 0.7 T, increasing to a maximum of 1.3 T in the inside corner.

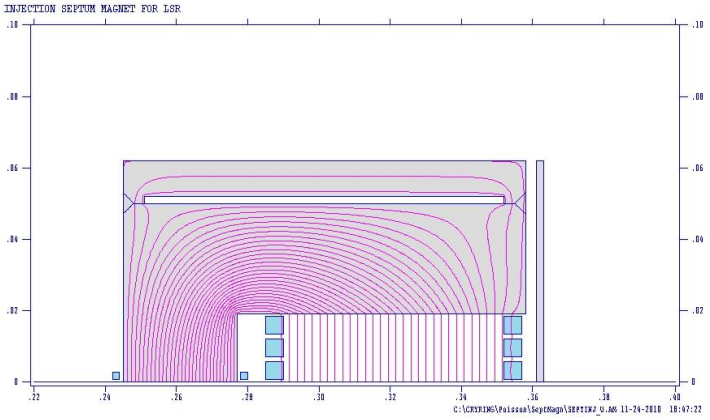

Fig. 5.15. Plot from 2-d magnetic-field calculations of injection septum magnet with field lines. Only the upper half of the mirror-symmetric magnet is shown. The iron is gray and the coil, with three turns seen, is blue. The thin region to the right is the iron screen and the blue areas with small cross section indicate a trim coil.

Fig. 5.16 shows the field in the centre of the magnet along a horizontal line perpendicular to the direction of the beam, i.e., along the horizontal axis in fig. 5.15 as calculated with Poisson. The position of the coil is indicated with gray shaded areas. The stray field outside of the screen is in the order of 1 G and can be made even smaller with the trim coil as seen in fig. 5.17.

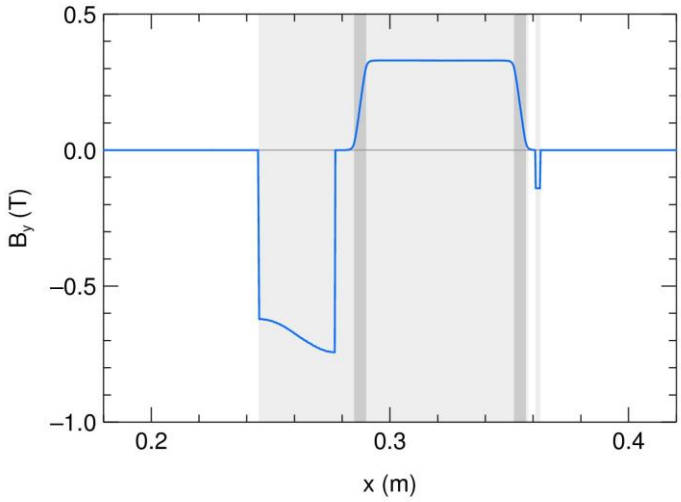

Fig. 5.16. Vertical component of the magnetic field, taken from the 2-d field calculation represented in the plot of fig. 5.15. The x-axis is the same as in that plot, and the two darker gray areas indicate the position of the coil while the lighter gray indicates the iron.

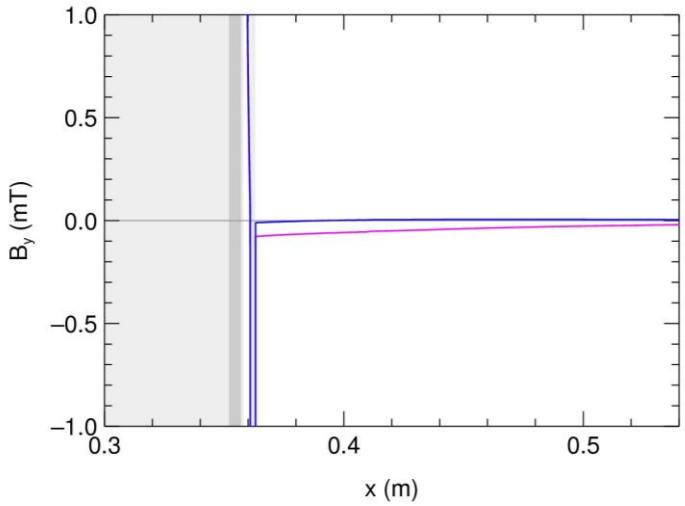

Fig. 5.17. Similar as fig. 5.16 but on a different scale, showing the stray field outside of the screen. Violet curve is the field without current in the trim coil, blue curve is with 13 A in the trim coil which makes the stray field equal to zero for all practical purposes.

One effect of the leakage field from the septum magnet is the distortion of the closed orbit due to the dipole component of the field. The displacement of the closed orbit is [43]

$$x(s) = \frac{\theta \beta^{1/2}(s - s_0)\beta^{1/2}(s_0)}{2 \sin \pi Q} \cos\left[\psi(s - s_0) - \pi Q\right]$$

for $0 < \psi < 2\pi Q$, where s_0 is the position of the deflection

$$\theta = \frac{\int B_\perp \mathrm{d}s}{B\rho}$$

caused by the leakage field. The horizontal β value at the septum magnet is 2.2 m, and the maximum is 6.6 m in the focusing quadrupoles, see fig. 3.10. Ignoring the phase, the maximum displacement can simply be approximated as $x_{\max} = 2.2\ \theta$. Allowing, conservatively, a displacement of 1 mm, it is found that the deflection due to the leakage field of the septum magnet can be at most 0.5 mrad or 1.5×10^{-3} of the 17 degree deflection of the injected beam in the septum magnet. The average leakage field along the septum magnet can thus be 0.5 mT at the $B\rho$ of the injected beam. If the antiproton beam is decelerated to 300 keV while the field in the septum magnet remains unchanged, only 0.05 mT can be tolerated. Judging from the Poisson calculations of fig. 5.17 and taking into account that the curved magnet bends away from the circulating beam, the passive iron screen alone should provide sufficient shielding, although just barely. With a trim coil, the leakage field can definitely be made insignificant, and it would also be possible to simply ramp down or turn off the septum field at the same time as the particles are decelerated

A similar calculation can be made for the maximum allowed quadrupole component or field gradient B' of the leakage field. A field gradient gives rise to a lens with focal length

$$\frac{1}{f} = \frac{\int B' \mathrm{d}s}{B\rho},$$

and the consequent tune shift is

$$\delta Q = \frac{1}{4\pi}\frac{\beta_0}{f},$$

where β is the beta function at the septum. If a δQ of 0.01 can be tolerated, the maximum field gradient is 0.07 T/m at the injection energy and 0.007 T/m if antiprotons are decelerated to 300 keV with a constant field in the septum magnet. Comparing again with fig. 5.17, it is seen that the quadrupole component of the leakage field is of similar importance as the dipole component, and that the use of a trim coil or ramping down of the septum field during deceleration is motivated also because of the quadrupole component.

From the 3-d calculations with Opera, the vertical field component along the incoming/outgoing beam is obtained as in fig. 5.18. The length of the iron along the arc is 683 mm, and from the integral of the field in the figure, an effective length of 708 mm along the arc is obtained. With the 2413 mm bending radius, this arc length gives a bending angle of 16.8 degrees, which is the angle required according to fig. 5.4.

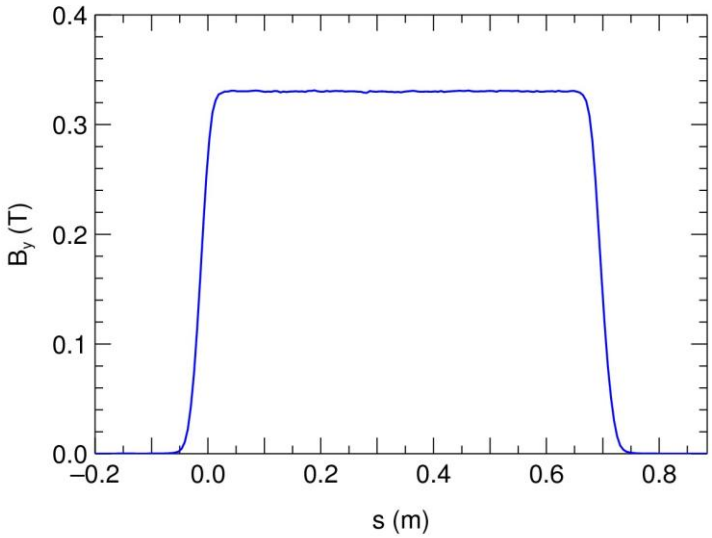

Fig. 5.18. Vertical magnetic-field component along an arc in the septum magnet, obtained from 3-d calculations with the geometry illustrated in fig. 5.14. The field is calculated with 10 000 ampere-turns and on an arc 10 mm inside the septum coil. The effective length does not depend significantly on the position of the arc in the interval relevant for the incoming or outgoing beams.

Magnet length (projected length of iron yoke)	674	mm
Deflection angle (including fringe fields)	16.8	degrees
Bending radius	2413	mm
Gap height	38	mm
Gap width	80	mm
Maximum field strength	0.33	T
Coil turns	6	
Turn length (average)	1660	mm
Wire dimension	5 × 5	mm^2
Cooling-channel diameter	3	mm
Thickness of wire insulation	0.5	mm
Maximum current	1670	A
Maximum voltage	17.2	V
Maximum power	28.6	kW
Inductance	56	μH
Parallel hydraulic circuits	6	
Length of hydraulic circuit (approx.)	1700	mm
Maximum temperature rise	30	°C
Total water flow at maximum power	14	l/min
Maximum pressure drop over cooling circuit	2.3	bar

Table 5.4. Data for septum magnets. Current, voltage etc. are for an ideal magnet with, e.g., iron of infinite permeability.

The coil is wound from a hollow copper conductor, and the main design criterion is, except for the matching with the Foeldi current supply, to achieve a septum that is as thin as possible without compromising robustness or reliability. A wire with a quadratic cross section of dimension 5 × 5 mm^2,

including a 3-mm-diameter cooling channel is chosen. Each turn, having approximately 1.7 m length, constitutes one hydraulic circuit. A pressure drop of 2.3 bar across the turns is then sufficient to get the water flow required for a maximum allowed temperature rise of 30 °C. The main parameters of the magnets are summarized in table 5.4. The values for, e.g., current and voltage are for an ideal magnet. The finite permeability of the iron, resistance in cables, etc., make it necessary for the current supply to have a current margin of approximately 10% and a voltage margin of around 20%.

5.6. Injection and Extraction Kicker Magnets and Pulse Supplies

Kicker magnets with pulse generators have been ordered from Sigmaphi in Vannes, France. Injection and extraction kicker magnets will be identical and of window-frame type, so both are described in this section, although the pulse supplies will be different. The available space for the overall length of the kicker magnets, between screw-heads of the ceramic vacuum chambers, is 457 mm for the injection kicker and 467 mm for the extraction kicker, and the elliptical vacuum chambers will have 105 mm horizontal diameter and 85 mm vertical diameter. The magnets will be manufactured with a length of 400 mm and with a gap of 107 mm horizontally and 87 mm vertically. Their longitudinal positions in the ring are discussed in sections 5.2.1 and 6.2.1.

As calculated in sections 5.4.1 and 6.3.2, the injection kicker magnet has to kick the beam by an angle of 16.5 mrad while the extraction kick has to be 17.3 mrad. In order to have a small margin for errors in beam optics and alignment, both magnets are specified to produce a kick angle of 20 mrad. Injection into LSR from NESR is foreseen always to be made at a rigidity of 0.80 Tm, corresponding to 30 MeV antiprotons, so 20 mrad implies that a fixed integrated field of 0.016 Tm is required from the injection kicker. The extraction kicker is designed for a variable rigidity between 0.054 Tm, corresponding to 140 keV antiprotons, and 0.80 Tm, requiring an integrated field variable between 0.0016 and 0.016 Tm. In this design report, the lowest antiproton energy is normally considered to be 300 keV, but since there have been suggestions to go to lower energies, and because of the expected cost and difficulty of modifying the kicker pulse supply, it is from the beginning designed to go down to the energy given by the lowest current of 40 A in the main dipole power converter. To ensure an extra operational margin and increased robustness, 20% is added to the maximum field strength, and the magnets should thus to have an integrated field of minimum 0.0192 Tm. Table 5.5 gives some of the magnet parameters.

Magnet length	400 mm
Horizontal aperture	107 mm
Vertical aperture	87 mm
Ferrite thickness	20 mm
Insulation thickness	4 mm
Maximum field strength	0.048 T
Number of turns in coil	1
Maximum current in coil	3630 A
Inductance	0.88 μH
Maximum voltage	10.7 kV

Table 5.5. Main parameters of injection and extraction kicker magnets.

According to section 5.4.2, the shortest fall time required of the injection kicker (and the fastest rise time of the extraction kicker) are given by 30 MeV (anti)protons to 280 ns. It was argued that a five per cent error could be allowed in the size of the kick. The magnets are therefore specified to have the fall time (rise time) defined as the time it takes for the integrated magnetic field to drop from 99% to 1% (or rise from 1% to 99%), and in addition specifications are given concerning the constancy of the flat-top field, how close to zero the field must go, pulse-to-pulse variations, etc.

Since the fast injection always is made at the same magnetic rigidity, the flat-top current is always the same for the injection kicker. Extraction can be made at a range of energies, from 140 keV to 30 MeV for antiprotons, which means that the flat-top current of the extraction kicker must be variable within a rather wide range. In addition, the maximum flat-top length must be much longer than for the injection kicker. Since the longest flat tops are required for the lowest currents and the slowest rise times, however, the amount of energy in the kicker pulse is still limited. Fig. 5.19 shows the rise time and pulse length as a function of the strength of the kick (integrated field in the magnet, proportional to magnet current). Both times are inversely proportional to the current, but the maximum flat-top time is limited to 16.3 μs, since extraction of highly charged ions is not foreseen below the rigidity 0.079 Tm of 300 keV antiprotons, even though the extraction kicker is specified to go down to the 0.054 Tm rigidity of 140 keV antiprotons.

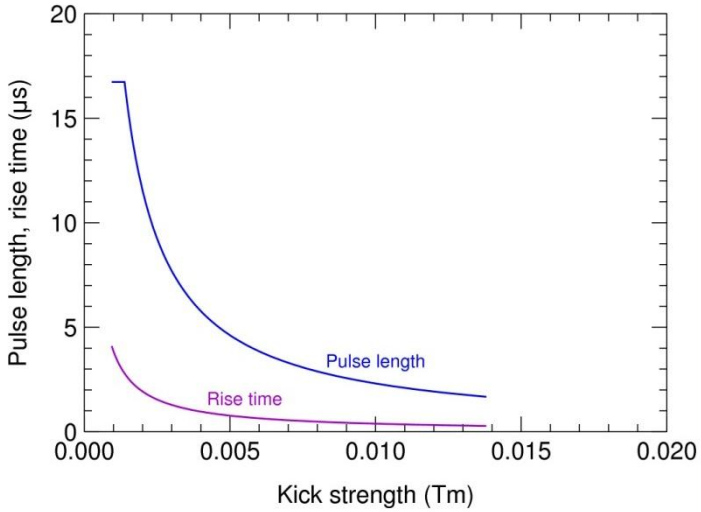

Fig. 5.19. Rise time and pulse length of extraction kicker as a function of nominal kick strength or integrated field in the kicker magnet. The nominal strength is based on the kick angle of 17.3 mrad which requires 0.0138 Tm at the beam rigidity 0.80 Tm of 30 MeV antiprotons.

The pulse supplies that will be delivered together with the magnets are based on semiconductor technology with fast IGBT (Insulated Gate Bipolar Transistor) switches. The principle is to have a high-voltage supply that is switched on to provide the high voltage during the short ramp up. In parallel, there is a low-voltage supply that feeds current through the magnet during the flat top [42]. With a second switch, the circuit is interrupted to create the ramp down, and the stored energy is then absorbed in a free-wheel circuit. For the injection supply, the free-wheel circuit has to be fine-tuned to give an optimal ramp down while it can have a simpler design in the extraction supply. In contrast to the case of a standard pulse-forming line or pulse-forming network, this supply is not matched to the load, and it therefore operates with a lower voltage. In fig. 5.20, a schematic diagram of the pulse

circuit is shown. Since both the supply and the magnet are designed by Sigmaphi, further details cannot be given at present.

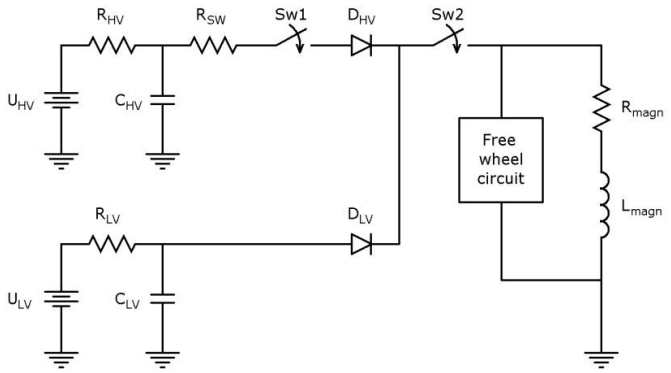

Fig. 5.20. Schematic diagram of pulse supply for injection and extraction kicker magnets.

6. Design of Extraction

6.1. Introduction

The aim with the extraction from LSR is that it should be possible to provide users with beams of ions and antiprotons over a parameter range that is as wide as possible. Relevant particle species are antiprotons from the NESR ring, light ions from the low-energy injector for singly charged ions and heavy multiply or highly charged ions from an ECR ion source connected to the low-energy injector or from NESR. The range of extraction energies coincides with the range of energies through which particles will be decelerated in LSR, i.e. 300 keV to 30 MeV for antiprotons, and for ions extraction will be possible through the same range of magnetic rigidities as for the antiprotons. Both fast single-turn extraction and slow resonant extraction will be implemented. Single-turn extraction uses a fast kicker magnet whereas the resonant extraction is based on rf-noise excitation of the beam in the vicinity of a third-order horizontal resonance.

Although 30 MeV antiprotons corresponds to only 55% of the maximum rigidity of CRYRING, it has been decided by the FLAIR collaboration to set an upper limit for the extraction energy at this value in order to save costs and complexity for extraction systems and beamlines.

6.2. Position of Kicker and Septa

6.2.1. Longitudinal Position of Kicker Magnet and Electrostatic Septum

The extraction system has three main components: a fast kicker for the single-turn extraction, an electrostatic septum for the resonant extraction and a magnetic septum which is common for single-turn and resonant extraction.

The purpose of both the kicker magnet and the electrostatic septum is to cause a deflection of the beam which results in a displacement at the magnetic septum, and the displacement must be larger than the

thickness of the magnetic septum plus its displacement from the closed orbit of the circulating beam. The requirement that a deflection is translated to a displacement means the betatron phase separation between the two must be close to an odd number of quarter betatron wavelengths, which is the same condition as for the injection kicker. Fig. 6.1 shows the betatron phase advance as a function of position over one superperiod relative to the centre of a magnet-free straight section and for the working point $Q_x = 2.33$, $Q_y = 2.42$, i.e., on the third-order horizontal resonance used for slow extraction. The curve is very similar to the one for $Q_x = 2.42$, $Q_y = 2.42$, which is the working point foreseen for fast injection and extraction and which is shown in fig. 5.5.

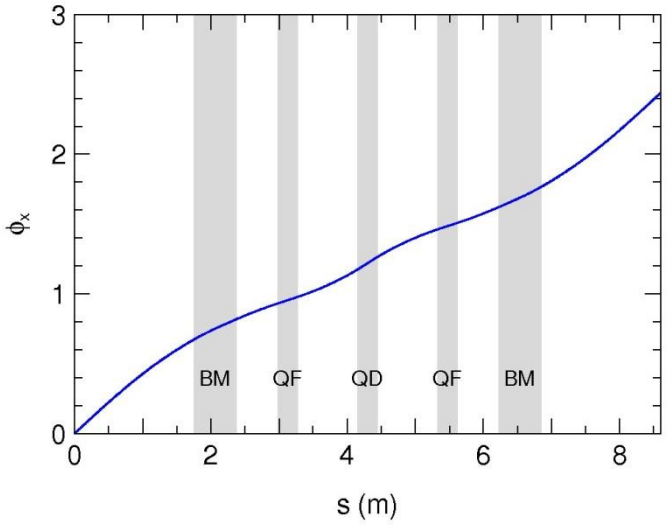

Fig. 6.1. Horizontal betatron phase advance in one superperiod for the working point $Q_x = 2.33$, $Q_y = 2.42$ that will be used for the resonant extraction. The shaded areas illustrate the positions of dipole and quadrupole magnets (c.f. fig. 3.1).

It is there seen, in a similar way as for the injection, that if the magnetic septum is close to the centre of its straight section, a betatron phase difference of $\pi/2$ occurs just at the beginning of the preceding straight section. The free space at that position, between the dipole magnet and the quadrupole magnet that follows it, is however too short for a kicker magnet, and putting the electrostatic septum there gives rise to an aperture problem: An electrostatic septum has to sit at some radial distance from the closed orbit, and it deflects the beam further out horizontally. Since the beam pipe has an inner diameter of 100 mm in the quadrupoles at the same time as the horizontal beta functions are at maximum in the focusing quadrupoles, the deflection required for the beam to cross the magnetic septum becomes too big at the second focusing quadrupole in the section of the electrostatic septum, and the beam would hit the chamber wall at this quadrupole before reaching the extraction channel at the magnetic septum.

The best solution is instead to have the extraction kicker between the first focusing quadrupole and the defocusing quadrupole on the section before the magnetic septum, and the electrostatic septum will be positioned after the defocusing quadrupole and the adjacent defocusing sextupole. The betatron phase difference for the electrostatic septum is less optimal at this position, but the septum foil can be made longer because there is more available space, so the septum voltage can be approximately the same as if the position immediately after the dipole could be used.

With the kicker magnet, the problem with the aperture in the focusing quadrupole is somewhat smaller since the kicker deflects particles that move near the closed orbit. These particles reach large horizontal displacements slightly later than those deflected by the electrostatic septum.

The kicker magnet and the electrostatic septum will, more specifically, be placed symmetrically in the drift sections of 874 mm and 624 mm nominal length, respectively, that can be seen in fig. 3.1.

6.2.2. Transverse Position of Septa

The horizontal position of the electrostatic septum foil, i.e., its distance from the closed orbit, should be as far out as possible in order not to reduce the horizontal acceptance of the ring more than necessary, but it must be sufficiently close to the centre of the beam pipe such that the deflected beam does not hit the vacuum-chamber wall on the way to the magnetic septum. The most critical limitation is due to the 100-mm vacuum pipe through the quadrupole and sextupole following the electrostatic septum. This diameter can hardly be increased without installing new magnets. On the other hand, the separation from the equilibrium orbit must have reached at least 52 mm at the position of the magnetic septum as discussed below, and the diameter of the beam pipe from the dipole chamber to the magnetic septum, including the dipole chamber itself with its bellows, will be increased from the present 100 mm to 150 mm for the LSR.

An offset of 30 mm from the closed orbit is close to optimum if a relatively large horizontal acceptance is to be maintained. This offset value allows enough room for the deflected beam, but not with very large margins, and at the same time it reduces the horizontal acceptance only slightly compared to the limit set by the magnetic septa. Calculating the acceptance as in section 5.2.2, with a horizontal beta function of 4.94 m (see table 6.1) and still a 5 mm margin for magnet and alignment errors, a single-particle acceptance of 130π mm mrad is obtained. If, on the other hand, a smaller acceptance can be allowed for low-emittance NESR beams, the septum offset can be reduced to 20 mm in order to get more room for the deflected beam. These two cases are investigated numerically in section 6.6.2, and the electrostatic septum will be movable so that the exact optimum can be found experimentally.

The situation is similar for the magnetic septum, and this has also been discussed in the section about the transverse position of the injection septum. If it is too close to the closed orbit it will reduce the ring acceptance. If it is too far out, the kicker magnet must be made stronger and the voltage on the electrostatic septum will have to be higher than necessary, and also the issue with insufficient horizontal aperture between electrostatic and magnetic septa appears again. As in the case of the injection septum, it is chosen to position the inside of the magnetic septum as seen by the beam (i.e., inside vacuum) 25 mm outside of the closed orbit. Since the lattice functions are the same in the extraction section as in the injection section, the extraction septum will thus produce the same small acceptance reduction to 180π mm mrad for the circulating beam as discussed in the section about the position of the injection septum.

The extracted beam can be assumed to be well cooled and we therefore use the same 5 mm margin between the beam in the septum channel and the septum wall as at the injection. With a septum thickness of 22 mm, the deflections at the electrostatic septum or the extraction kicker thus have to produce a displacement of 25 + 22 + 5 = 52 mm at the entrance to the septum channel.

6.2.3. Longitudinal Position of Magnetic Septum

Given the positions of the extraction kicker and the electrostatic septum, and the fact that optimum performance is obtained if the betatron phase difference between these and the magnetic septum is close to $\pi/2$, the magnetic septum should be located as far downstream on its straight section as possible. This would imply a geometry symmetrical to that of the injection section. To get somewhat further away from the stray field of the dipole magnet after the extraction section, however, it is chosen to move the magnet approximately 200 mm upstream, so that the beam enters the septum magnet at the centre of the straight section. The extraction septum magnet has the same dimensions as the injection septum magnet and is described in more detail in section 5.5.

6.3. Deflection at Electrostatic Septum and Kicker Magnet

6.3.1. Deflection at Electrostatic Septum

The deflection required at the extraction kicker magnet or the electrostatic septum is calculated as in section 5.4.1 for the injection kicker. Table 6.1 shows the values of the lattice parameters β, α and the betatron phase $\Delta\psi$ at the positions of the electrostatic and magnetic septa at the working point of $Q_x = 2.33$, $Q_y = 2.42$ foreseen for slow extraction. The betatron phase is measured from the centre of the section where the magnetic septum is located.

	β [m]	α	$\Delta\psi$
Electrostatic septum	4.941	-1.593	-1.036
Extraction septum magnet	2.197	0	0

Table 6.1. Lattice parameters at the positions of electrostatic and magnetic septa for the working point at slow extraction with $Q_x = 2.33$, $Q_y = 2.42$.

To calculate the deflection needed at the electrostatic septum when it is offset by 30 mm from the closed orbit, we set $x_d = 30$ mm and $x_m = 52$ mm in equations (5.1) and (5.2) and solve for x'_d and x'_m, finding $x'_d = 24.4$ mrad and $x'_m = 3.4$ mrad. At the same time, particles that have not quite reached the electrostatic septum must pass the septum magnet unhindered, so for these particles we put $x_m = 20$ mm, including a 5 mm margin to the inside of the magnetic septum at 25 mm, and still $x_d = 30$ mm, now finding $x'_d = 13.1$ mrad and $x'_m = -5.2$ mrad. The difference between 24.4 mrad and 13.1 mrad, or 11.3 mrad, is the deflection angle that the electrostatic septum has to provide, if the particles to be extracted follow an outgoing separatrix that intersects the electrostatic septum position of $x_d = 30$ mm exactly at $x'_d = 13.1$ mrad. The trajectories from the electrostatic septum to the magnetic septum for particles starting at this point, deflected and undeflected, are shown in fig. 6.2. It is seen that the deflected particles in this ideal case will pass through the focusing quadrupole and sextupole at a displacement x of approximately 43 mm. Since the beam pipe there has an inside diameter of 100 mm, this leaves a 7 mm margin that can be taken up by the horizontal size of the extracted beam.

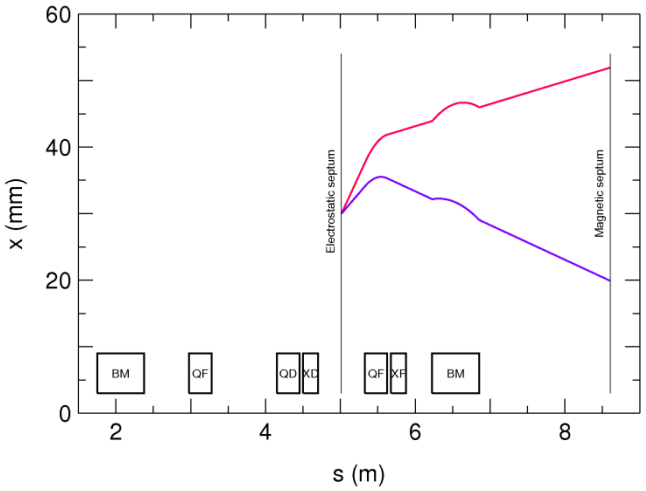

Fig. 6.2. Trajectories of particles starting at the electrostatic septum with a 30 mm offset from the equilibrium orbit and ending in the extraction channel at x = 52 mm after deflection at the septum (upper curve) or ending at x = 20 mm without having been deflected at the electrostatic septum.

In order to get more room for the extracted beam through the quadrupole and sextupole, the electrostatic septum can be shifted inward by 10 mm to a displacement of 20 mm from the equilibrium orbit. This reduces x'_d both for the deflected and undeflected beam by 2.0 mrad, leaving the required deflection angle at the electrostatic unchanged at 11.3 mrad. Particle trajectories for this case are shown in fig. 6.3. It is seen that the room for the extracted beam in the quadrupole and sextupole magnets now has increased from 7 mm to 15 mm. This is achieved at the expense of a reduced horizontal acceptance of the ring.

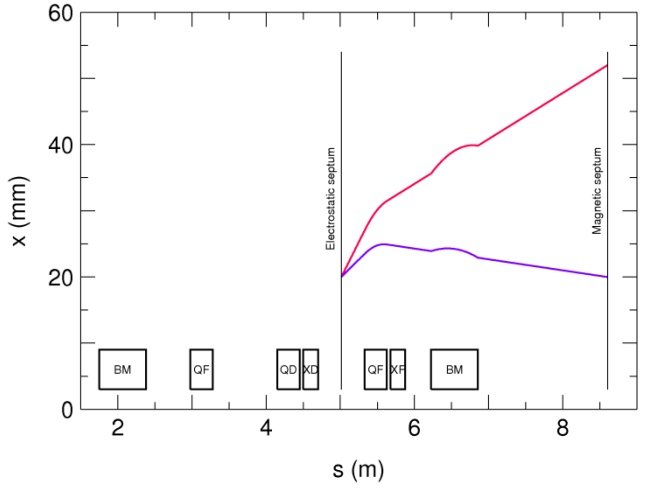

Fig. 6.3. Similar to fig. 6.2, except that the electrostatic septum has been moved in from 30 mm outside of the equilibrium orbit to 20 mm outside of the equilibrium orbit.

Table 6.3 summarizes the two cases with the two different septum positions. A more complete numerical calculation, taking finite beam size and momentum spread into account, is presented in section 6.6.2. There it is also discussed how to obtain a separatrix with the required orientation.

6.3.2. Deflection at Extraction Kicker

For the deflection at the kicker magnet we can instead use equations (5.3) and (5.4). Also, we use the working point $Q_x = 2.42$, $Q_y = 2.42$ which is the standard one at CRYRING today, and where the lattice parameters at the positions of the kicker and the magnetic septum are given in table 6.2.

	β [m]	α	$\Delta\psi$
Extraction kicker magnet	4.778	1.592	-1.418
Extraction septum magnet	1.932	0	0

Table 6.2. Lattice parameters for the working point used today at CRYRING, suitable for fast extraction at LSR, with $Q_x = 2.42$, $Q_y = 2.42$.

With $x_m = 52$ mm, we find $x'_d = 17.3$ mrad and $x'_m = 4.2$ mrad. At $Q_x = 2.33$, $Q_y = 2.42$, the corresponding values are $x'_d = 16.7$ mrad and $x'_m = 4.6$ mrad, showing that small shifts in working point are not significant for the design of the fast extraction. The trajectory of a particle starting at the kicker with $x_d = 0$ and a deflection such that it ends up at $x_m = 52$ mm is shown in fig. 6.4. It is seen that such a particle has a slightly smaller displacement through the focusing quadrupole and sextupole than a particle deflected at an electrostatic septum at $x_d = 30$ mm in fig. 6.2. The issue with the acceptance of a beam that is on its way to be extracted is thus slightly less critical for fast extraction than for slow extraction.

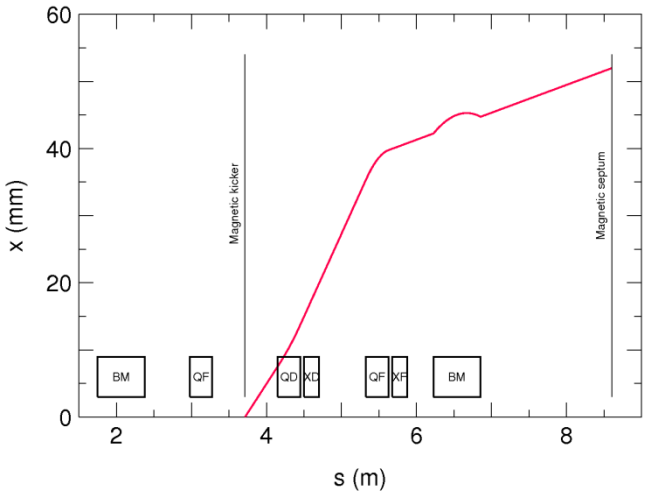

Fig. 6.4. Trajectory of particles starting on the closed orbit at the magnetic extraction kicker and being deflected there by 17.3 mrad such that they end up in the extraction channel at $x = 52$ mm.

	Q_x/Q_y	x_d (mm)	x'_d (mrad)	x_m (mm)	x'_m (mrad)
Slow extraction, septum at 30 mm	2.33/2.42	30	24.4	52	3.4
Circulating beam, septum at 30 mm	2.33/2.42	30	13.1	20	–5.2
Slow extraction, septum at 20 mm	2.33/2.42	20	22.4	52	7.0
Circulating beam, septum at 20 mm	2.33/2.42	20	11.1	20	–1.7
Fast kicker extraction	2.42/2.42	0	17.3	52	4.2

Table 6.3. Summary of beam positions and angles for extraction, at the deflection element (electrostatic septum or kicker magnet, subscript d) and at the magnetic septum (subscript m), for slow and fast extraction. The required deflection angle at the electrostatic septum is the difference between x'_d for the extracted beam and for the circulating beam, i.e., 11.3 mrad for both electrostatic septum positions.

6.4. Electrostatic Septum

The electrostatic septum consists of a thin stainless-steel foil and a gold-plated aluminium electrode attached to each other as a single moveable unit. The unit is mounted inside its vacuum tank on two linear motion feedthroughs. The electrode is electrically insulated from the foil through its mounting on alumina rods. The feedthroughs and the foil are on earth potential while the electrode is connected to a high-voltage feedthrough such that an electric field is produced between the foil and the electrode, deflecting particles that pass on the electrode-side of the foil. Fig. 6.5 shows a CAD model of the foil–electrode assembly.

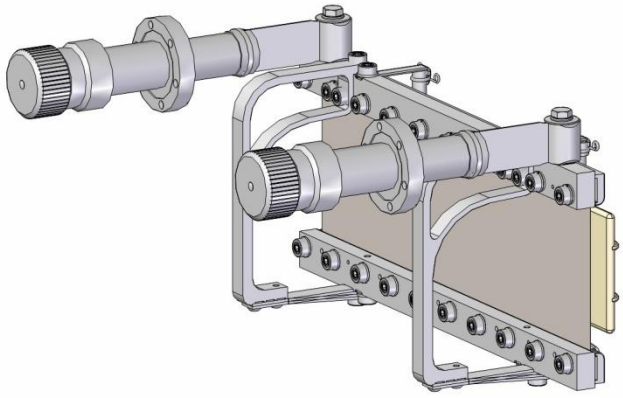

Fig. 6.5. Assembly of electrostatic septum with foil on earth potential attached to a high-voltage electrode (rightmost) through alumina rods. The position and angle of the foil can be adjusted with a pair of linear motion feedthroughs.

The septum foil has a thickness of 0.1 mm and is kept flat by tension in the suspension mechanism. The foil is 387 mm long and 109 mm high while the high-voltage electrode is equally long but 90 mm high. The distance between the foil and the electrode is 15 mm, but this can be changed easily by replacing four simple metal parts attaching the alumina rods to the foil holder. With the two linear motion feedthroughs from MDC, the horizontal position of the foil assembly can be adjusted such that the foil position can be moved from 10 mm to 45 mm outside of the centre of the vacuum chamber, i.e., outside of the nominal beam position. The attachments of the foil assembly to the motion feedthroughs are slightly flexible, so that the horizontal angle of the foil can be adjusted by setting the motion feedthroughs at different positions.

The electric field strength E required to deflect particles with mass m and charge q over an angle θ is given by

$$\theta = \tan^{-1}\left(\frac{qEL}{m\gamma v^2}\right),$$

where L is the length of the septum foil, v the particle velocity and γ the usual relativistic factor. In LSR, the highest energy protons or antiprotons require the strongest field for a given angle. Setting θ = 11.3 mrad according to section 6.3.1 and L = 0.387 m, the field strength for 30 MeV antiprotons becomes 1.72 MV/m. With the distance between septum foil and high-voltage electrode equal to 15 mm, an electrode voltage of a modest 25.9 kV is sufficient. A 30 kV high-voltage feedthrough is thus used for the electrode voltage, and the connection to the moveable electrode is made through a spring.

The vacuum tank, seen in fig. 6.6 and fig. 6.7, has 250 mm diameter and an overall length of 510 mm. The upstream end has a CF 250 flange where bellows are fitted, whereas the other end has a CF 100 flange. There are two ports for the motion feedthroughs and one for the high-voltage electrode. For mounting of the foil assembly there are two additional ports facing upward and one facing downward. These are also used for pumping with two NEG pumps upward and one ion pump downward.

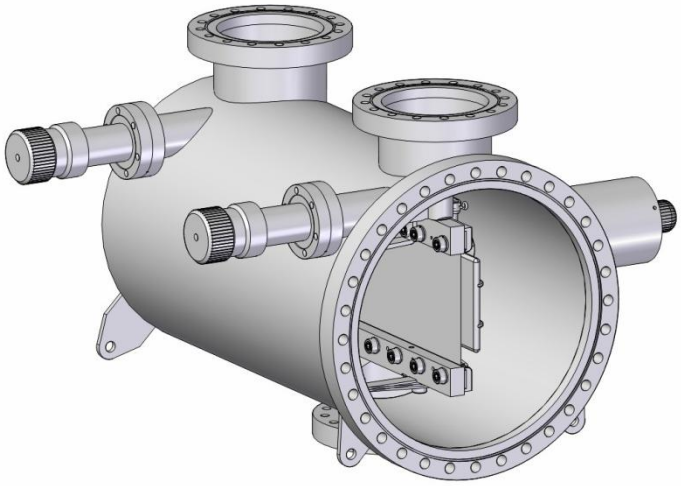

Fig. 6.6. Vacuum tank for electrostatic septum with two linear motion feedthroughs (left side) and a 30 kV high-voltage feedthrough (right side).

Fig. 6.7. Photograph of vacuum tank with electrostatic septum, with bakeout jacket installed.

6.5. Ceramic Vacuum Chamber for Kicker Magnets

The horizontal acceptance in CRYRING is limited by the 100-mm-inner-diameter vacuum chamber in the quadrupole magnets. It can be seen from fig. 3.10 that the ratio between the horizontal beta function in the focusing quadrupoles and the maximum beta in the vacuum chambers for the kicker magnets, at their locations between focusing and defocusing quadrupoles, is approximately 1.08. The horizontal aperture in the kicker magnets thus needs to be 96 mm in order not to reduce the acceptance. Similarly, the vertical acceptance in the ring is limited by the 54-mm internal height of the dipole vacuum chambers, resulting in a required vertical aperture in the kicker magnets of 75 mm.

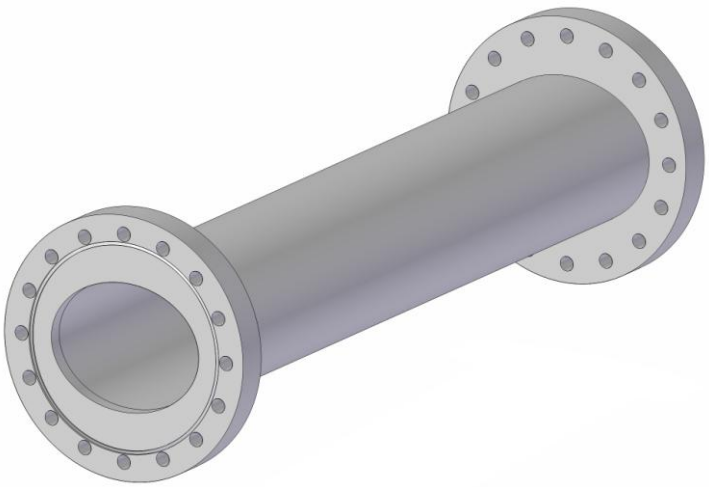

Fig. 6.8. Schematic model of ceramic vacuum chamber for injection kicker magnet.

These vacuum chambers, one for each kicker magnet, will be made from Al_2O_3 with stainless-steel CONFLAT flanges, c.f. fig. 6.8. Their inside will have an elliptical cross section with diameters 94

mm horizontally and 74 mm vertically, and they will be metallized with 0.2 μm Ti. Procurement was initialized at the end of 2010.

6.6. Detailed Calculations of Resonant Extraction

Of the modifications that need to be made to CRYRING, the resonant extraction is the one which requires the most careful study. Details to investigate include the geometry of the extraction, the efficiency and how to deal with ripple on power supplies. Since extraction has to work down to the lowest energy of the ring, ripple on the magnet power converters will have a strong influence on the time structure of the extracted beam unless countermeasures can be taken.

6.6.1. Theory Background

6.6.1.1. Excitation of a Third-Integer Resonance

The theory of resonant extraction can be found in several text books on accelerator physics, such as that by Edwards and Syphers [43]. The horizontal betatron oscillation of a particle in x–p_x phase space is written as

$$\begin{aligned} x &= a\left(\frac{\beta(s)}{\beta(s_0)}\right)^{1/2}\cos\psi(s), \\ p_x &\equiv \beta(s)x' + \alpha(s)x = -a\left(\frac{\beta(s)}{\beta(s_0)}\right)^{1/2}\sin\psi(s), \end{aligned} \tag{6.1}$$

where α and β are the usual Twiss parameters, ψ is the betatron phase, s is the longitudinal coordinate and s_0 is the coordinate of a point of observation where the betatron amplitude is a. A horizontal magnetic field of strength ΔB over a (short) distance Δs deflects the particle, which has charge q and momentum p, by an amount

$$\Delta x' = -\frac{q\Delta B\Delta s}{p}$$

giving

$$\Delta p_x = -\frac{q\beta(s)\Delta B\Delta s}{p},$$

while the particle position x in the first approximation is unchanged at the point of deflection so that $\Delta x = 0$. Differentiating equation (6.1), inserting the values for Δx and Δp_x and solving for the resulting Δa and $\Delta\psi$, one finds

$$\Delta a = \frac{q\beta_0}{p}\left(\frac{\beta(s)}{\beta(s_0)}\right)^{1/2} \Delta B \Delta s \sin\psi(s),$$
$$\Delta \psi = \frac{q\beta_0}{p}\left(\frac{\beta(s)}{\beta(s_0)}\right)^{1/2} \Delta B \Delta s \cos\psi(s).$$

If there is a distribution of fields $\Delta B(x, s)$, the amplitude and phase changes can be integrated over one turn. Treating the turn number n as a continuous variable, the amplitude change per turn is immediately found to be

$$\frac{\mathrm{d}a}{\mathrm{d}n} = \frac{q\beta_0}{p}\oint\left(\frac{\beta(s)}{\beta(s_0)}\right)^{1/2} \Delta B(x,s)\sin\left[\psi(s_0)+\Delta\psi(s)\right]\mathrm{d}s. \qquad (6.2)$$

With the phase change per turn in the absence of perturbing fields equal to $2\pi Q$, integrating the phase changes due to ΔB, one finds

$$\frac{\mathrm{d}\psi}{\mathrm{d}n} = \frac{q\beta_0}{p}\oint\left(\frac{\beta(s)}{\beta(s_0)}\right)^{1/2} \Delta B(x,s)\cos\left[\psi(s_0)+\Delta\psi(s)\right]\mathrm{d}s + 2\pi Q.$$

In the case of resonant extraction using sextupole magnets, the perturbing field will have the form

$$\Delta B(x,s) = \frac{B''(s)}{2}x^2.$$

This field can be inserted into equation (6.2) using the expression for x from (6.1) and some trigonometric identities to find the amplitude growth for a particular sextupole setting. The resulting expression will contain terms proportional to sin $\psi(s_0)$ and cos $\psi(s_0)$ that vary rapidly from turn to turn and average to zero, but there will also be terms proportional to sin $3\psi(s_0)$ and cos $3\psi(s_0)$ that vary slowly close to a third-integer resonance. Retaining only the latter ones, the amplitude growth at s_0 becomes

$$\frac{\mathrm{d}a}{\mathrm{d}n} = \frac{1}{4}a^2\left[A\sin 3\psi(s_0) + B\cos 3\psi(s_0)\right]$$

with

$$A = \frac{q\beta(s_0)}{p}\oint\left(\frac{\beta(s)}{\beta(s_0)}\right)^{3/2}\frac{B''}{2}\cos\left(3\frac{Q_0}{Q}\Delta\psi(s)\right)\mathrm{d}s,$$
$$B = \frac{q\beta(s_0)}{p}\oint\left(\frac{\beta(s)}{\beta(s_0)}\right)^{3/2}\frac{B''}{2}\sin\left(3\frac{Q_0}{Q}\Delta\psi(s)\right)\mathrm{d}s.$$

Here we have used $Q \approx Q_0$, the tune exactly on the resonance, and introduced the factor Q_0/Q in the expressions for A and B, so that these are machine parameters calculated on the resonance. The change of ψ can be written in a similar way, but to get a phase coordinate that does not jump around from turn to turn, "rotating" coordinates with a phase

$$\tilde{\psi} = \psi - 2\pi Q_0 n$$

are first introduced. Then, the change in amplitude and phase is

$$\frac{\mathrm{d}a}{\mathrm{d}n} = \frac{1}{4}a^2\left[A\sin 3\tilde{\psi}(s_0) + B\cos 3\tilde{\psi}(s_0)\right],$$
$$\frac{\mathrm{d}\tilde{\psi}}{\mathrm{d}n} = \frac{1}{4}a^2\left[A\cos 3\tilde{\psi}(s_0) - B\sin 3\tilde{\psi}(s_0)\right] + 2\pi\delta,$$

where $\delta = Q - Q_0$.

Now, $\mathrm{d}a/\mathrm{d}n$ and $\mathrm{d}\tilde{\psi}/\mathrm{d}n$ can be set equal to zero, and three fixed points in x–p_x or x–x' phase space are then found. These are given by

$$a = \frac{-8\pi\delta}{(A^2 + B^2)^{1/2}},$$
$$\tilde{\psi} = -\frac{1}{3}\arctan\frac{B}{A}.$$

The corresponding x and x' are obtained from equation (6.1), giving

$$x = -\frac{8\pi\delta}{(A^2 + B^2)^{1/2}}\cos\left(\frac{1}{3}\arctan\frac{B}{A} + n\frac{2\pi}{3}\right),$$
$$x' = \frac{8\pi\delta}{\beta(s_0)(A^2 + B^2)^{1/2}}\left[\sin\left(-\frac{1}{3}\arctan\frac{B}{A} + n\frac{2\pi}{3}\right) + \alpha(s_0)\cos\left(\frac{1}{3}\arctan\frac{B}{A} + n\frac{2\pi}{3}\right)\right].$$

Analyzing the particle motion further, it is found that these points are the corners of a triangle, the separatrix, separating stable trajectories for particles inside the triangle from unstable trajectories outside. If particles with stable trajectories can be excited, for example by the application of rf noise, across the separatrix, their oscillation amplitudes will grow, and they can—if the geometry is chosen carefully—end up in the extraction channel. Particles inside the separatrix can also get unstable trajectories if the size of the separatrix is reduced by changing quadrupole or sextupole settings.

6.6.1.2. Application of Third-Integer Extraction to CRYRING

The way that extraction will be configured in CRYRING is illustrated in fig. 6.9. Particles that are excited slightly past the separatrix will follow its outgoing legs as indicated by arrows. An electrostatic septum at a certain x deflects the particles as indicated in fig. 6.9a. Downstream at approximately $\pi/2$ betatron phase advance, as shown in fig. 6.9b, this deflection allows the particle to cross the magnetic septum and get extracted from the ring.

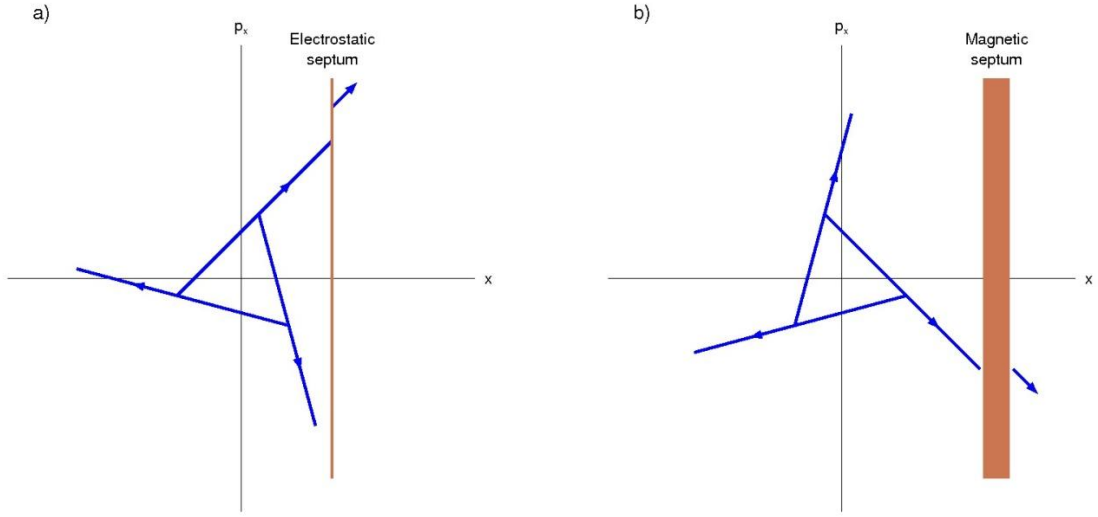

Fig. 6.9. Illustration of extraction geometry. To the left (a) is a phase-space diagram at the position of the electrostatic septum, where particles that have reached unstable orbits follow the outgoing legs of the separatrix until the cross the electrostatic septum and get deflected. The right diagram (b) shows the situation at the magnetic septum where the kick at the electrostatic septum makes the particles cross the magnetic septum and continue into the extraction channel.

For this extraction scheme to work, several criteria must be fulfilled. First the area of the separatrix must be reasonably big, and the separatrix must be rotated to a correct angle to match the extraction geometry as seen from the figure. This is achieved by selecting the proper values of *A*, *B* and δ. The area is proportional to δ, the distance to the resonance, while both the area and the rotation are influenced by *A* and *B*. Since CRYRING has one focusing and one defocusing sextupole in each of the six superperiods, *A* and *B* can be written as

$$A = \beta(s_0)\left[\sum_{i=1}^{6}\left(\frac{\beta_\mathrm{f}}{\beta(s_0)}\right)^{3/2}\frac{S_{\mathrm{f},i}}{2}\cos 3(\psi_{\mathrm{f},i}-\psi_0)+\sum_{i=1}^{6}\left(\frac{\beta_\mathrm{d}}{\beta(s_0)}\right)^{3/2}\frac{S_{\mathrm{d},i}}{2}\cos 3(\psi_{\mathrm{d},i}-\psi_0)\right],$$

$$B = \beta(s_0)\left[\sum_{i=1}^{6}\left(\frac{\beta_\mathrm{f}}{\beta(s_0)}\right)^{3/2}\frac{S_{\mathrm{f},i}}{2}\sin 3(\psi_{\mathrm{f},i}-\psi_0)+\sum_{i=1}^{6}\left(\frac{\beta_\mathrm{d}}{\beta(s_0)}\right)^{3/2}\frac{S_{\mathrm{d},i}}{2}\sin 3(\psi_{\mathrm{d},i}-\psi_0)\right].$$

Here, $S_{\mathrm{f},i}$ and $S_{\mathrm{d},i}$ are the normalized sextupole strengths, defined by $S = B''L/B\rho$, for the focusing and defocusing sextupoles respectively, and β_f, $\psi_{\mathrm{f},i}$, etc. are the beta functions and phases at the sextupoles. Index 0 still denotes the point of observation. Since the 12 sextupoles can be individually controlled, there are many possibilities to achieve the desired separatrix.

For particles with a momentum difference Δp from the nominal momentum, dispersion will cause the orbit to shift in *x*. The position of the closed orbit will change from $(x, x') = (0, 0)$ to (D, D'), where $D(s)$ is the dispersion function. If there is also chromaticity, the distance to the resonance δ will change with Δp, and the size of the stable area in phase space will change. If the dispersion function and the chromaticity are properly selected, it is possible to fulfil the condition (the Hardt condition) that all particles reach the electrostatic septum at the same angle which minimizes the number of particles hitting the inside or the outside of the septum foil. This is illustrated in fig. 6.10. The need to control

the chromaticity in this way puts another constraint on the sextupole settings, but with the 12 degrees of freedom available, settings consistent with all requirements can be found.

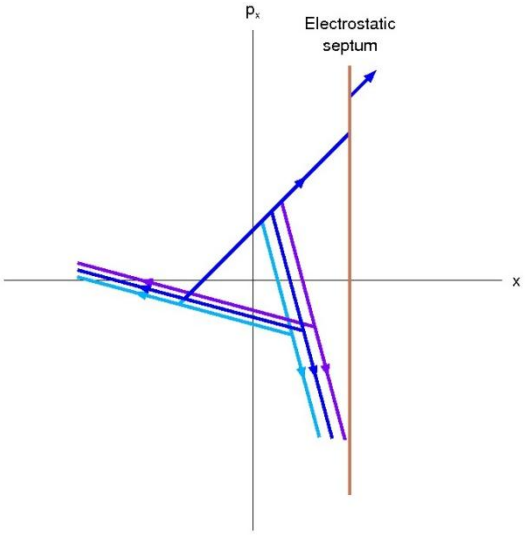

Fig. 6.10. Illustration of the Hardt condition where particles arrive to the electrostatic septum at the same angle independently of their momentum deviation. The three triangles represent three different momenta.

6.6.1.3. Chromaticity

It is necessary to control the chromaticity in the ring in order to get the Hardt condition fulfilled. The natural chromaticity of the linear lattice has contributions from the dipole and quadrupole magnets. The sextupole magnets used to excite the extraction resonance generate additional contributions, and the sextupoles are also used to set the desired overall chromaticity.

The quadrupoles generate horizontal and vertical chromaticities given by

$$Q'_x = \frac{\Delta Q_x}{\Delta p / p} = -\frac{1}{4\pi}\sum k_{x,i} L_i \beta_{x,i} = -\frac{1}{4\pi}\left(12 k_\mathrm{f} L \beta_{x,\mathrm{f}} - 6 k_\mathrm{d} L \beta_{x,\mathrm{d}}\right),$$

$$Q'_y = \frac{\Delta Q_y}{\Delta p / p} = \frac{1}{4\pi}\sum k_{y,i} L_i \beta_{y,i} = \frac{1}{4\pi}\left(12 k_\mathrm{f} L \beta_{y,\mathrm{f}} - 6 k_\mathrm{d} L \beta_{y,\mathrm{d}}\right).$$

Here $k_\mathrm{f}L$ and $k_\mathrm{d}L$ are the normalized strengths of the focusing and defocusing quadrupoles (see also section 3.6 and 3.7), $\beta_{x,\mathrm{f}}$, $\beta_{x,\mathrm{d}}$, $\beta_{y,\mathrm{f}}$ and $\beta_{y,\mathrm{d}}$ are the horizontal and vertical beta functions at these quadrupoles, and we are using the fact that CRYRING has 12 focusing quadrupoles and 6 defocusing quadrupoles used in two single families. At the working point Q_x = 2.33, Q_y = 2.42, the quadrupole strengths are k_f = 1.74 and k_d = 2.30 m^{-2}, and the beta functions are approximately $\beta_{x,\mathrm{f}}$ = 6.3, $\beta_{x,\mathrm{d}}$ = 3.3, $\beta_{y,\mathrm{f}}$ = 3.6 and $\beta_{y,\mathrm{d}}$ = 8.3 m. A more precise calculation where the beta functions are integrated over the quadrupoles give quadrupole chromaticities $Q'_x = -2.03$ and $Q'_y = -0.92$.

For the chromaticities due to the dipole magnets, we use the expressions of [44] (see also [45]), which contain contributions both from the dipole edges and from their interiors. Their expressions contain field gradients which we set equal to zero and terms arising from curved magnet edges which we also do not have. What remains is

$$\begin{aligned} Q'_x = -\frac{1}{4\pi}\{ & \int_{s_1}^{s_2} [h^2\beta + h(2D'\alpha - D\gamma)]\mathrm{d}s \\ & + [-h\beta\tan\theta + h\tan^2\theta(\beta D' - 2\alpha D + hD\beta\tan\theta)]_{s=s_1} \\ & + [-h\beta\tan\theta - h\tan^2\theta(\beta D' - 2\alpha D - hD\beta\tan\theta)]_{s=s_2}\}, \end{aligned}$$

$$\begin{aligned} Q'_y = -\frac{1}{4\pi}\{ & \int_{s_1}^{s_2} (-hD\gamma)\,\mathrm{d}s \\ & + [h\beta\tan\theta - h\tan^2\theta(\beta D' - 2\alpha D - hD\beta\tan\theta) - \beta hD']_{s=s_1} \\ & + [h\beta\tan\theta + h\tan^2\theta(\beta D' - 2\alpha D + hD\beta\tan\theta) + \beta hD']_{s=s_2}\}. \end{aligned}$$

The first terms with the integrals are due to the magnet interior while the terms evaluated at $s = s_1$ and $s = s_2$ derive from the upstream and downstream edges respectively. In addition to the Twiss parameters α, β and γ and the dispersion function D and its derivative D', the expressions contain the inverse of the bending radius h and the beam entrance angle θ which in our case is 15 degrees. A numerical evaluation of these expressions give dipole chromaticities equal to $Q'_x = 0.39$ and $Q'_y = -2.05$.

The sextupoles, finally, introduce chromaticities

$$Q'_x = \frac{1}{4\pi}\sum S_i\beta_{x,i}D_i = \frac{1}{4\pi}\left(\sum_{i=1}^{6} S_{\mathrm{f},i}\beta_{x,\mathrm{f}}D_{\mathrm{f}} + \sum_{i=1}^{6} S_{\mathrm{d},i}\beta_{x,\mathrm{d}}D_{\mathrm{d}}\right),$$

$$Q'_y = -\frac{1}{4\pi}\sum S_i\beta_{y,i}D_i = -\frac{1}{4\pi}\left(\sum_{i=1}^{6} S_{\mathrm{f},i}\beta_{y,\mathrm{f}}D_{\mathrm{f}} + \sum_{i=1}^{6} S_{\mathrm{d},i}\beta_{y,\mathrm{d}}D_{\mathrm{d}}\right).$$

Here S_f and S_d are the normalized strengths (defined as $S = B''L/B\rho$) of the focusing and defocusing sextupoles, $\beta_{x,\mathrm{f}}$ and $\beta_{x,\mathrm{d}}$ are the horizontal beta functions and D_f and D_d are values of the horizontal dispersion at the sextupoles. We have used the fact that the sextupoles have the same positions in all superperiods, so that beta functions and dispersions are the same at all six focusing sextupoles and at all six defocusing sextupoles. Note that the horizontal dispersion enters also for the vertical chromaticity correction.

It is seen from section 6.6.1.2 that the influence of sextupole magnets on the excitation of the extraction resonance depends on the betatron phases $\psi_{\mathrm{f},i}$, and $\psi_{\mathrm{d},i}$ at these magnets, and due to the symmetry of CRYRING, two magnets located diametrically opposite to each other will contribute to the excitation with opposite sign. Their contribution to the chromaticity, on the other hand, have the same weight in all superperiods. If the resonance is excited using pairs of diametrically opposite

sextupoles with fields that have opposite signs, no additional chromaticity is thus introduced, while the effects in exciting the resonance are added within the pairs. The inverse holds if the aim is to change the chromaticity. This can be achieved by changing all focusing sextupoles or all defocusing sextupoles with the same amount, and then there is no effect on the excitation of the resonance.

An additional criterion to apply when selecting which sextupoles to use for excitation of the resonance is to make sure that the overall sextupole strengths are as low as possible. This will minimize higher-order effects that the sextupoles introduce such as coupling between the horizontal and vertical particle motion.

6.6.2. Numerical Simulations

6.6.2.1. Introduction

In order verify analytical calculations of the extraction geometry and to study the effects of magnet ripple on the resonant extraction, numerical simulations of the extraction process have been performed. A simple tracking code was written based on linear transfer matrices. It uses 3-d transfer matrices in the two planes (x, x', p_x) and (y, y', p_y) to represent quadrupole fields and edge focusing in dipoles as defined in the MAD file of table 3.3. In addition, sextupole magnets are included as thin lenses with amplitude-dependent strengths, and the code features electrostatic and magnetic extraction elements as well as heating of the beam with white noise on a transverse electrostatic kicker. Chromaticity in dipoles, quadrupoles and sextupoles is included.

The six superperiods, defined to start at the centre of the magnet-free straight sections, are labeled 1–6. Superperiod 6 is the one which ends at the straight section of the magnetic extraction septum.

In all calculations shown in this report, initial particle distributions are parabolic in horizontal and vertical betatron amplitude as well as in $\Delta p/p$. All numerical values apply to protons or antiprotons at an energy of 300 keV, although most of the general conclusions are valid for any particle species or energy. The actual energy only matters if dimensionless quantities such as, for instance, the sextupole strengths s_x and s_y have to be converted to numerical values in T/m^2, or when comparisons with fixed time scales such as that of the magnet ripple have to be made. For 300 keV protons or antiprotons, the revolution time is approximately 7 μs and simulations are run for 150 000 turns, corresponding to approximately 1 s. Up to 100 000 particles are tracked in order to give reasonable statistics.

Ripple can be included as a first-order effect in dipoles by adding a dispersive term and as a second-order effect in the quadrupoles through a modulating of their focusing strengths (second order since the effect on the particle coordinate is proportional both to particle displacement and ripple amplitude). Also ripple on sextupoles can be taken into account. All main dipole magnets of CRYRING have backleg windings, and ac currents can be imposed on these windings or on the separate correction dipoles in order to study how intensity ripple on the extracted beam can be counteracted.

Resonant extraction takes place near the third-order resonance $Q_x = 2\ 1/3$, where white noise drives the beam across the resonance. The noise is realized in the simulations as a horizontal deflection in a pair of kicker plates where the deflection angle is given by a random variable with Gaussian distribution.

The simulations below first show cases without ripple, where the distance of the electrostatic septum from the closed orbit and the size of the stable phase space are varied. Then the effect of ripple on the magnets is studied.

6.6.2.2. Large Acceptance, Large Stable Phase Space

Fig. 6.11 shows extracted intensity and phase-space distributions as a function of time for a set of parameters that fulfill all geometrical requirements on the circulating and extracted beams. The horizontal tune is Q_x = 2,323, i.e., slightly below the resonance. The vertical tune is Q_y = 2.42 which is the standard value used in CRYRING.

Four sextupoles are excited to create unstable orbits for extraction. Which sextupoles to excite and with which strengths is chosen to get, among other things, a stable phase-space area of relatively large size with an outgoing separatrix that has a suitable orientation. Here, the focusing sextupoles of magnet sections 1 and 4 and the defocusing sextupoles of magnet sections 3 and 6 are used, and their strengths are 1.700, −0.390, −2.000 and 1.590 in normalized units (equal to $B''l/B\rho$). On top of the resonance excitation, the focusing and defocusing sextupoles are used in two single families to produce a chromaticity that makes the Hardt condition fulfilled. In this case, the required chromaticity is $Q'_x = -0.5$.

The initial parabolic particle distributions in x and y have maximum amplitudes of 0.5%, and in $\Delta p/p$ the maximum amplitude is 0.05%. All particles thus start in the stable part of phase-space.

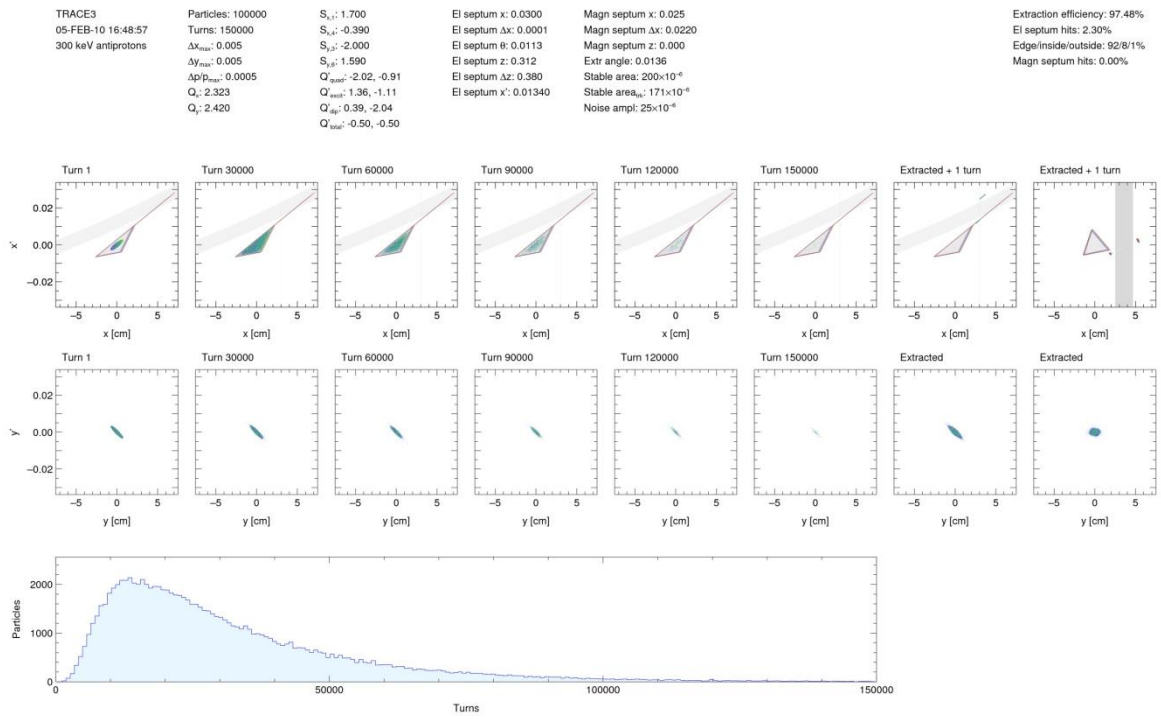

Fig. 6.11. Phase-space distributions in x–x' (upper row) and y–y' (middle row) planes during the resonant extraction process and extracted intensity as a function of turn number (lower plot). See text for details.

The upper row of plots in fig. 6.11 shows the horizontal phase space during extraction. The first six plots show particle positions at the electrostatic septum at six different moments during the spill. The turn numbers are indicated in the plot. The colour used for plotting the particles show the initial momentum spread, ranging from $-(\Delta p/p)_{max}$ (violet) through zero (blue-green) to $+(\Delta p/p)_{max}$ (red). The triangular area in the centre represents the stable phase-space. The triangular boundary to unstable phase-space and one outgoing separatrix, as calculated from the theory in section 6.6.1, are shown as lines of different colour. Blue represents the boundary for particles with momentum deviation $-(\Delta p/p)_{max}$, gray is the boundary for zero momentum deviation and red is for $+(\Delta p/p)_{max}$. The stable area for particles with zero momentum deviation as obtained from the simulations is shown as a light gray background. There are also thin blue and red triangles indicating the simulated stable area for particles with $\pm(\Delta p/p)_{max}$, but these more or less coincide with the other lines and are hardly visible. The thin, vertical line represents the electrostatic septum, and the diagonal thick line at the top represents the magnetic septum "transported" to the position of the electrostatic septum. The 7th plot shows particles that have left the stable phase space. They are plotted on the last turn before they cross the electrostatic septum and in addition just after they have crossed it and been deflected by an angle of, in this case, 11.3 mrad. The 8th plot shows the same extracted particles but at the position of the magnetic septum. Here, the electrostatic septum is instead seen as a diagonal line. In fig. 6.12, the two upper right plots of fig. 6.11 are shown enlarged.

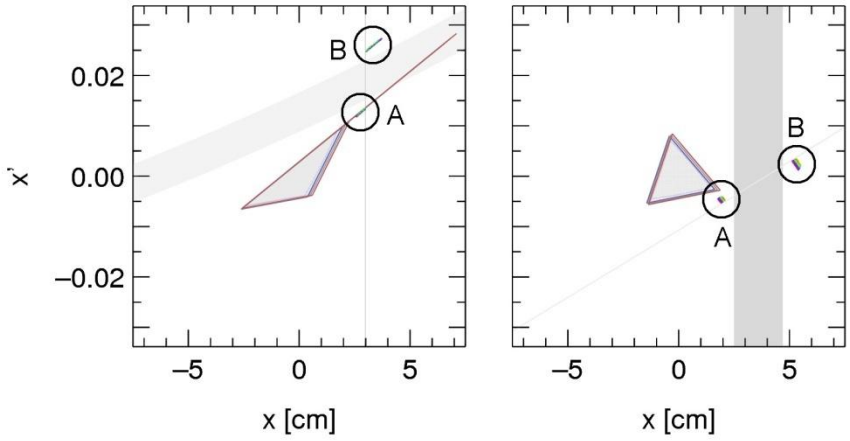

Fig. 6.12. Enlargement of upper right plots of fig. 6.11 showing the extracted beam three turns before (A) and just after (B) deflection by the electrostatic septum (left) and transported to the position of the magnetic septum (right). The triangular area in the centre represents the stable phase-space. The triangular boundary to unstable phase-space and one outgoing separatrix (in the left plot), as obtained analytically, are shown as red, gray and blue lines (see text for explanation). The stable area for particles of nominal momentum as obtained from the simulations is shown as a light gray background. The line (vertical to the left, tilted to the right) line represents the electrostatic septum. The rectangle (distorted to the left, straight to the right) shows the position of the magnetic septum.

In plots 1–7, it is seen that the outgoing separatrices coincide for all three colours (and only the red colour is then visible), i.e., they coincide for particles of all momenta. The simulations agree with the theory, and particles cross the electrostatic septum with the same angle, independent of momentum. This means that the Hardt condition is fulfilled. However, there is dispersion between the electrostatic and magnetic septa, and the rainbow of colours in the 8th plot show that particles enter the magnetic septum at positions and angles that have some dependence on momentum.

The middle row shows the corresponding particle positions in the vertical phase-space (only the last turn is shown in plots 7 and 8). The motion in the horizontal and vertical planes are only weakly coupled through the sextupole fields, and the vertical beam envelope is seen to be virtually unaffected by the extraction process.

The lower plot shows the extracted beam intensity as a function of time or turn number. In this example, the extraction noise amplitude is constant in time, giving an extracted intensity that first increases as the stored beam fills more and more of the stable phase space and then gradually decreases as the intensity of the stored beam decreases. After 150 000 turns, 0.3% of the particles still remain in the ring. As seen below, a more constant extracted intensity can be achieved with a noise amplitude that varies in time.

The electrostatic septum is positioned at a 30 mm offset from the equilibrium orbit and its thickness is 100 μm. The magnetic septum is at 25 mm offset and has a 22 mm thickness. These are the values from section 6.2 where the acceptance of the circulating beam is kept relatively large at the expense of a marginal distance between the particle trajectories and the vacuum chambers following the septum that have a 50 mm inner radius. As calculated in section 6.3, the smallest distance between the trajectory of a particle starting at 30 mm offset at the electrostatic septum and the chamber wall is 7 mm. This is approximately equal to the horizontal extension of the extracted beam (B in fig. 6.12), and the parameters of the simulation were in fact chosen so that the beam uses these 7 mm with no margin. This rather limited space for the extracted beam is thus one of the critical issues for slow beam extraction from CRYRING.

Also the extraction losses depend on this space for the extracted beam. The fraction of particles hitting the electrostatic septum is approximately equal to the ratio between septum thickness and allowed horizontal extension of the extracted beam. The ratio between 100 μm and 7 mm is relatively close to the 2.3% inefficiency obtained from the tracking code. Most of the discrepancy is due to the fact that the particle motion along the separatrix takes place in steps whose size increase with x (as seen by the difference in horizontal extension of the particle distributions A and B). See, e.g., [43] for details and an analytical expression for the step size.

6.6.2.3. Large Acceptance, Smaller Stable Area

For a fixed position of the electrostatic septum, in this case 30 mm from the equilibrium orbit, the size of the stable area can be chosen freely as long as the stable area itself does not intersect the septum. Fig. 6.14 shows a case where the sextupole settings are higher than in fig. 6.12, producing a stable area which is approximately half of that in fig. 6.12. In order to keep the extension of the extracted beam equal to the same 7 mm as above, the horizontal tune has to be moved closer to the resonance. Thus fig. 6.14 has Q_x = 2.328, producing a step size across the septum which is the same as in fig. 6.12. Otherwise only the sextupole settings are different compared to fig. 6.12. Since the extraction inefficiency is depending on the step size across the septum, it is the same 2.3% as in fig. 6.12.

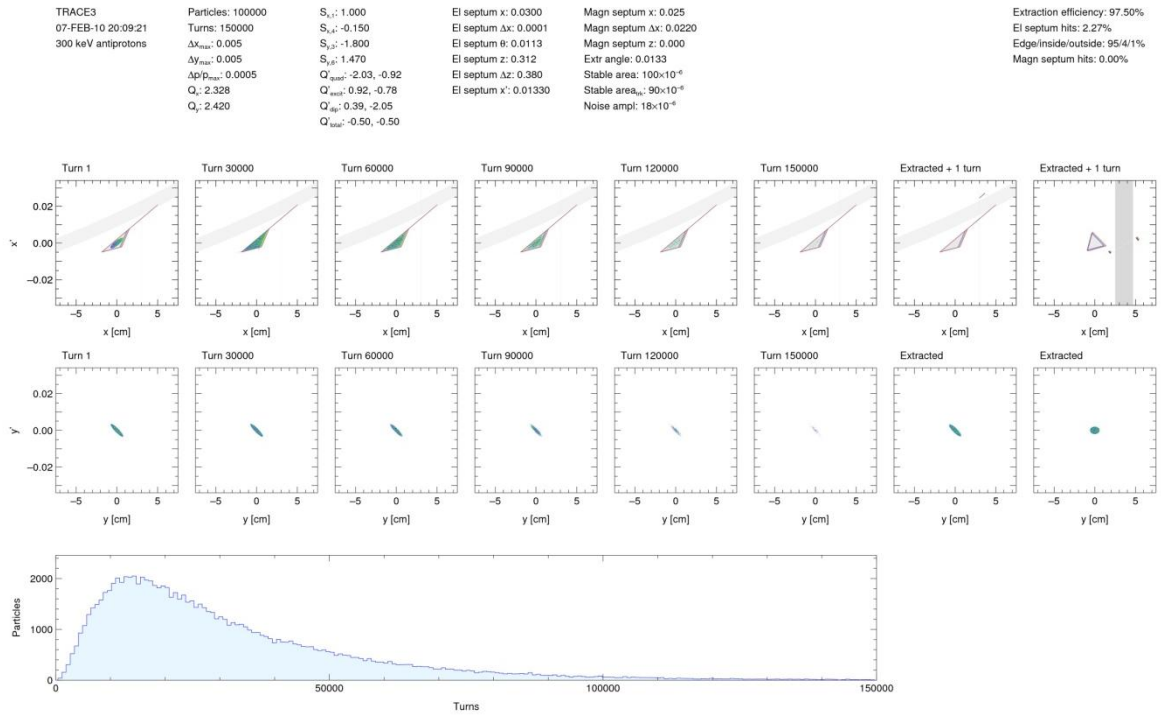

Fig. 6.13. Phase-space distributions etc. like in fig. 6.11 but with different quadrupole and sextupole settings, producing a smaller stable area.

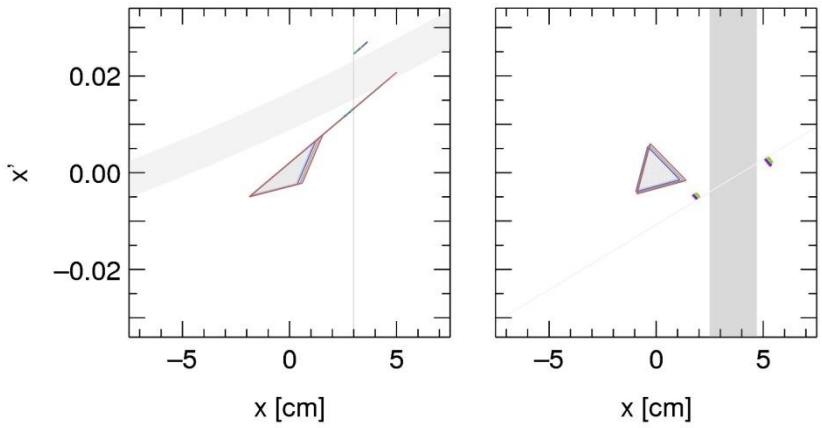

Fig. 6.14. Enlargement of the upper two plots of fig. 6.13, see caption of fig. 6.12 for explanation.

6.6.2.4. Smaller Acceptance, Lower Extraction Losses

It could be advantageous to move the electrostatic septum closer to the equilibrium orbit, since this gives a bigger margin for alignment errors before the extracted beam hits the vacuum wall on its way between the electrostatic septum and the magnetic septum. Some of the gain in alignment margin can also be traded for an increased extraction efficiency, i.e. a smaller number of particles hitting the electrostatic septum. The disadvantage of moving the septum inward is of course a smaller acceptance for the circulating beam. As an example, fig. 6.15 shows the case where the septum offset from the centre has been decreased from 30 mm to 20 mm. From the 10 mm gained outside the septum, approximately half has been used for the alignment margin and the other half has been used to reduce

the fraction of particles hitting the septum. This fraction is reduced by shrinking the size of the stable phase-space while keeping the horizontal tune in the same range as above, at Q_x = 2.326, thus increasing the size of the step by which the particles move out along the extraction separatrix at the point of the septum.

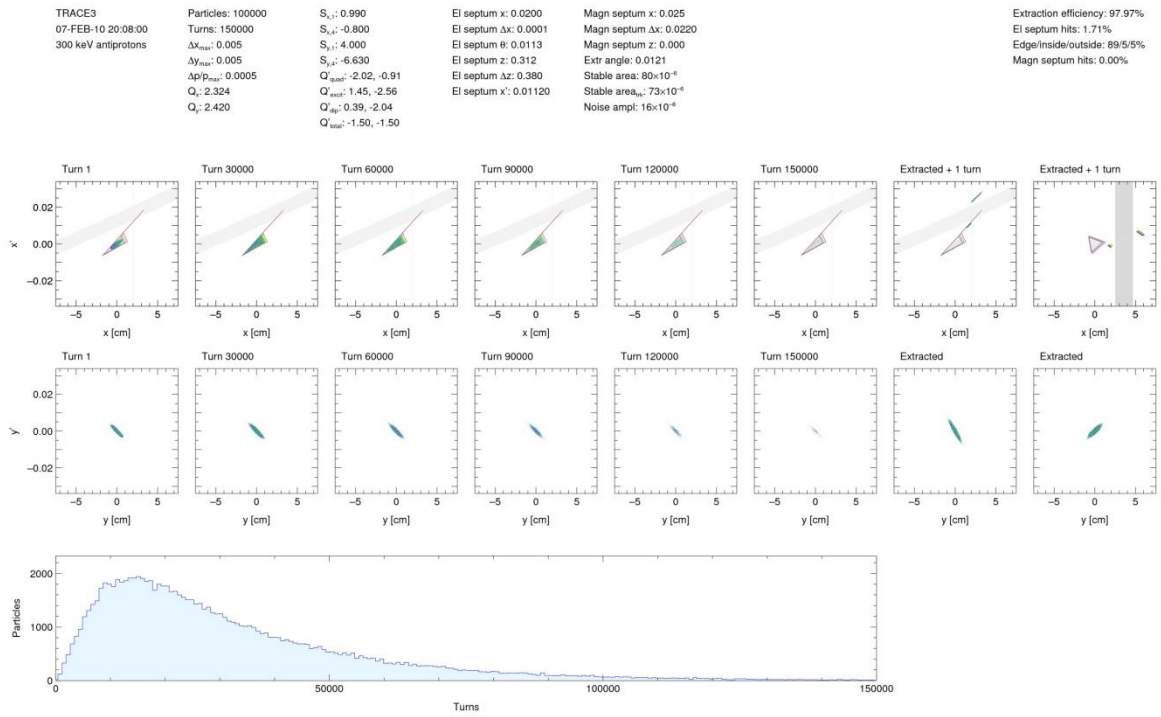

Fig. 6.15. Phase-space distributions etc. like in fig. 6.11 and fig. 6.13 but with the electrostatic septum closer to the equilibrium orbit.

The fraction of particles hitting the electrostatic septum is now reduced from 2.3% to 1.7%, and this decrease is approximately proportional to the increase in the horizontal extension of the deflected beam (upper distribution in the left plot in fig. 6.16).

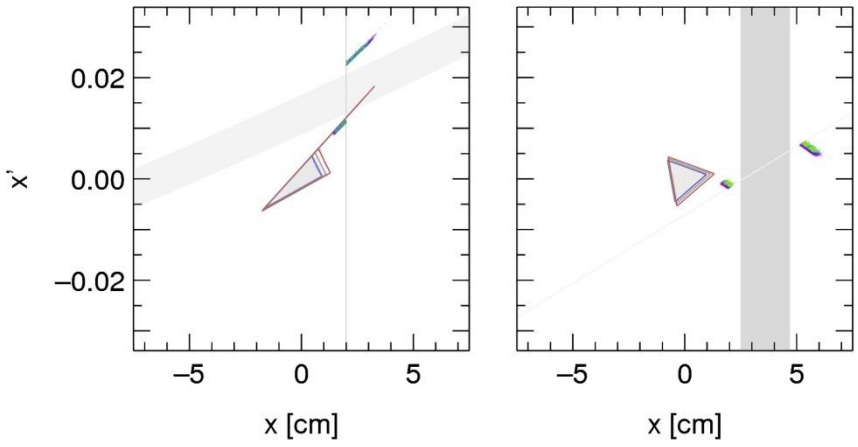

Fig. 6.16. Enlargement of upper right plots of fig. 6.15, showing the beam distribution in horizontal phase space just after deflection in the electrostatic septum and three turns before.

6.6.2.5. Constant Extracted Intensity

In fig. 6.11 etc. above, the noise applied to the beam causing the particles to get excited into unstable phase space is constant in time. This results in an extracted intensity that peaks in the beginning of the extraction period, in the plots lasting for 150 000 turns or approximately 1 s for 300 keV antiprotons, and then slowly decreases. Still after 1 s a small number of particles, a few tenths of a per cent, remain circulating in the ring. Fig. 6.17 shows that a more constant extraction intensity can be obtained by letting the noise amplitude be a function of time. No particles remain circulating in the ring at the end of the extraction period. Apart from the noise amplitude, all parameters are the same as in fig. 6.15.

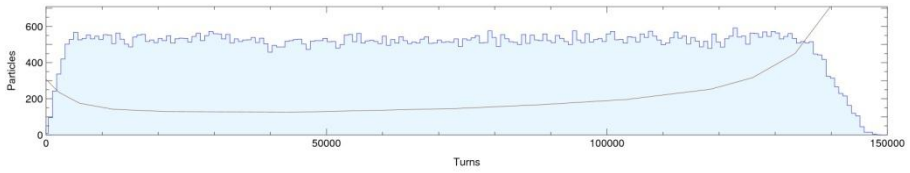

Fig. 6.17. Extracted intensity as a function of turn number. All parameters are the same as in fig. 6.13, except that the extraction noise amplitude now changes as a function of time according to the brown curve. This curve is adjusted in order to get an intensity that is constant in time. For 300 keV (anti)protons, the full period of 150 000 turns corresponds to approximately 1 s.

6.6.2.6. Ripple on Dipole and Quadrupole Magnets

Ripple on magnet power supplies, mainly dipole and quadrupole supplies, can cause intensity variations in the extracted beam. This is not so much because the particle positions move relative to the electrostatic septum. Rather it is the separatrix between stable and unstable phase space that moves with respect to the particle orbits, or vice versa.

In the tracking code, dipole ripple is implemented in first order through a dispersive term such that transport through a dipole magnet which is described by $\boldsymbol{x}_{\text{out}} = \mathbf{D}\cdot\boldsymbol{x}_{\text{in}}$ without ripple, where $\boldsymbol{x}$ is the column vector with components x, x' and $\Delta p/p$ and $\mathbf{D}$ is the horizontal transfer matrix for a dipole magnet, is replaced by $\boldsymbol{x}_{\text{out}} = \mathbf{D}\cdot\boldsymbol{x}_{\text{in}} - \Delta B/B\, \boldsymbol{D}_3$, where $\boldsymbol{D}_3$ is the third column of $\mathbf{D}$. The effect of a small increase in field strength $\Delta B/B$ thus is the same as that of a small momentum change $\Delta p/p = -\Delta B/B$ as it should be for particle motion in any magnetic field.

Quadrupole ripple is not noticeable in first order since its effect is proportional only to the product of $\Delta B/B$ and the displacement x. Nevertheless, it is implemented in the tracking code as a modulation of the quadrupole focusing strength, and sextupole ripple can be treated in the same way.

The main frequency components of both dipole and quadrupole ripple are multiples of 50 Hz, mainly up to 600 Hz, from the 12-pulse rectifiers of the power converters as discussed in section 3.14. As an example of the influence of dipole ripple on the extracted current, fig. 6.18 shows the a simulation with the same machine parameters as in fig. 6.13, except that a field ripple with amplitude $\Delta B/B = \pm 1\times 10^{-4}$ and frequency 150 Hz is added to all dipole magnets (which is much higher than the measured ripple shown in fig. 3.37). The lower right pane shows the spill is folded into a single 20-ms interval, and it is seen that the ripple results in a roughly ±50% modulation of the extracted intensity.

The size of the modulation depends on several factors, including the tune distance from the resonance, the spill rate and the horizontal chromaticity. For the parameters of fig. 6.15, where the chromaticity is near the natural chromaticity (equal to –1.63 including the dipole chromaticity according to sect. 6.6.1.3), the extracted intensity is not at all sensitive to dipole ripple such as it is modeled here. This is due to the symmetry of CRYRING, where a change in dipole field moves the closed orbit by the same amount in all sextupoles.

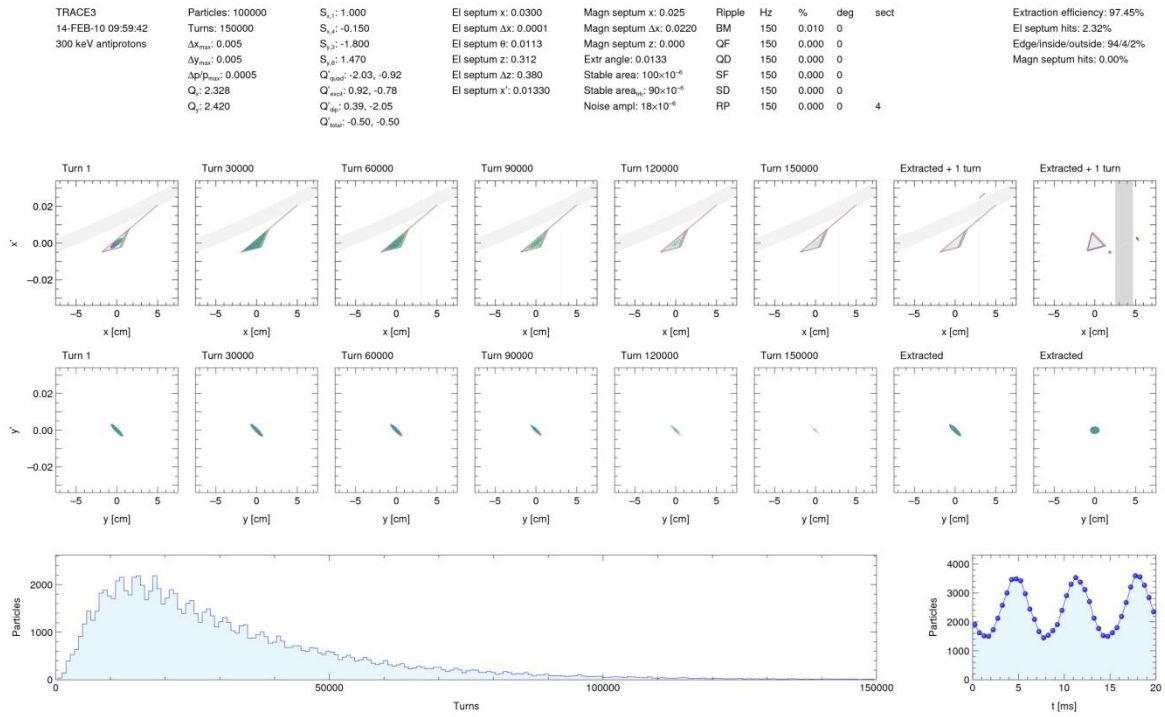

Fig. 6.18. Phase-space distributions etc. for the same machine settings as in fig. 6.13 but with 150 Hz ripple added to the dipole magnets. The lower right part of the figure shows the extracted intensity folded into a single 20-ms interval. (The wiggles in the lower left curve are smaller due to the limited time resolution.)

Because of the low measured amplitude of the dipole ripple and since it is possible to find machine settings satisfying all criteria for successful extraction, including the Hardt condition, without sextupole chromaticity, dipole ripple seems not to be a problem for slow extraction from the LSR. However, the tracking code can be used to show that, if there nevertheless is an effect of dipole ripple on the extracted beam, this can be counteracted by purposefully adding ripple on a single correction dipole. For instance, it is found numerically that the dipole ripple of fig. 6.18 can be compensated by adding ripple with the same phase on the horizontal correction dipole of magnet section 4. The field integral of the ripple amplitude in this correction dipole should be 4×10^{-6} Tm, requiring a current with 3 mA amplitude in the coil of the correction dipole, if the dipole ripple has an amplitude of $\Delta B/B = \pm 1 \times 10^{-4}$ for 300 keV (anti)protons. The measured ripple is smaller by a factor 4 (see section 3.14), so it is straightforward to build and install a small ac current supply that generates this compensating current, although the measured ripple has several frequency components (harmonics of 50 Hz) so that the compensating current also needs to generate several frequency components.

Quadrupole ripple changes the tune and thus the size of the stable phase-space triangle, again causing an intensity modulation of the extracted beam. Fig. 6.19 shows an example with, again, the machine

settings of fig. 6.13, but now with a ripple of $\pm 1 \times 10^{-4}$ amplitude at 150 Hz added to the focusing quadrupoles. The sensitivity to ripple on the defocusing quadrupoles is smaller since the tune distance to the horizontal third-integer resonance depends less strongly on the current in the defocusing quadrupoles than in the focusing quadrupoles.

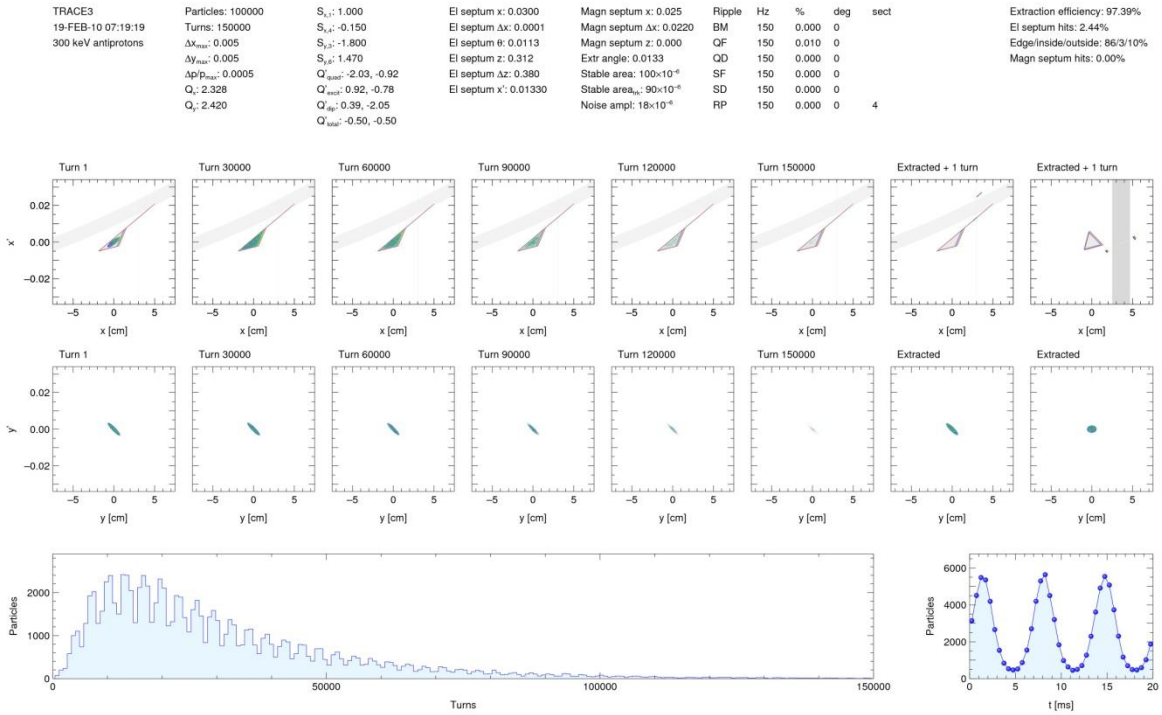

Fig. 6.19. Similar to fig. 6.18, but with a 150 Hz, 1×10^{-4} amplitude ripple on the focusing quadrupoles instead of on the dipoles.

Also the effect of quadrupole ripple on the extracted intensity can be counteracted by adding ripple on one single horizontal correction dipole. In the case of fig. 6.19, the desired effect is achieved if the field integral of correction dipole 4 has a ripple with an amplitude of 1×10^{-5} Tm, in opposite phase compared to the quadrupole ripple, at the beam rigidity of 300 keV (anti)protons. This corresponds to a current of 8 mA in the winding of the correction dipole.

Sextupole ripple has a much smaller effect on the extracted intensity. Comparing with quadrupole ripple, the size of the stable area is proportional to the sextupole strengths but to the difference between the actual quadrupole strength and the strength on the extraction resonance. Since this difference is small, a certain relative change in the quadrupole field changes the stable area much more than the same relative change in the sextupole fields, and this has also been verified numerically.

6.7. Closed-Orbit Corrections

In CRYRING there is one vertical and one horizontal correction dipole in each superperiod, and they are situated between the first focusing quadrupole and the defocusing one. In the LSR the correction magnets in superperiod 2 have to be moved to give room for the extraction kicker magnet.

In CRYRING there is one vertical and one horizontal correction dipole in each superperiod, and they are situated between the first focusing quadrupole and the defocusing one. In the LSR the correction magnets in superperiod 2 have to be moved to give room for the extraction kicker magnet.

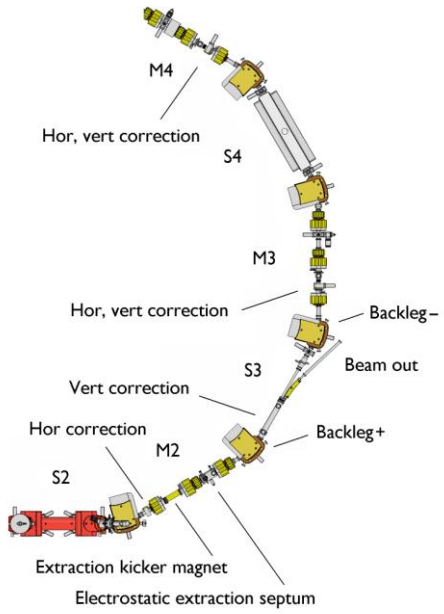

Fig. 6.19. Magnets for closed-orbit correction around the extraction at LSR.

A new correction scheme which includes new position for two magnets and one new power supply for two backleg magnets can be as follows:

The horizontal correction magnet will be moved upstream, and will be placed between the ring dipole and the focusing quadrupole. The vertical correction will be moved downstream, right after the first dipole on the extraction section.

In addition a new current supply will be connected to the presently unused 30 turn backleg windings on the two dipoles around the extraction section. A problem with backleg windings is that a large current will be induced when the magnetic field in the dipoles changes during deceleration. However, two backleg windings can be connected in series so that the induction from the acceleration cycle will cancel. When used, the two backleg windings will give kicks in opposite directions, and thus a parallel shift of the horizontal orbit. For example, 1 A will shift a 3 MeV (typical energy for cooling) antiproton beam 5 mm, so the current supply for the backleg windings can be small. It will be possible to adjust the horizontal closed orbit also without backleg windings, but the deformations of the orbit in other places will be larger. In fig. 6.20 the orbit after a change of the position at the electrostatic septum is shown.

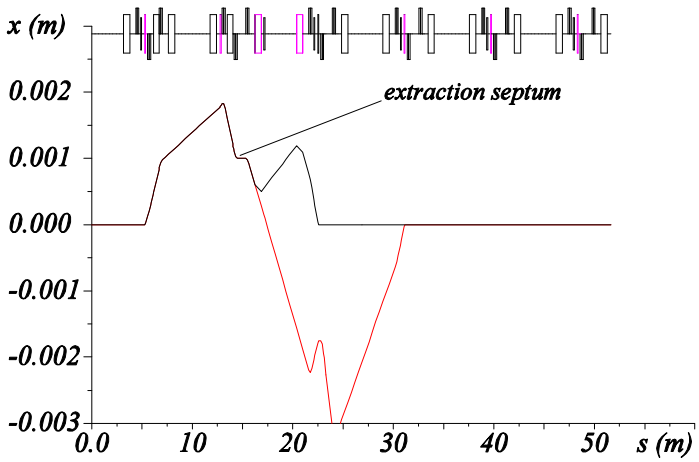

Fig. 6.20. Horizontal orbit adjustment of 1 mm at the electrostatic extraction septum. Red: without backleg windings, black: correction with backleg windings. Horizontal correction elements are shown in pink.

Vertically it will be more difficult to adjust the closed orbit, especially in the extraction section right after the moved magnets. Now the distance between the vertical correction magnets in superperiods 1 and 2 is much longer and the deviation of the closed orbit becomes unacceptably large. The maximum displacement is almost -5 mm to get a 1 mm shift. See the red line in fig. 6.21. The situation is not better if one instead uses only the correction in superperiod 6, green line. However, a combination of these gives an acceptable result, the maximum deviation becomes –1.5 of the shift in the extraction section as the black line shows. The strength of the correction magnet in superperiod 6 should be 0.53 of the one in superperiod 1.

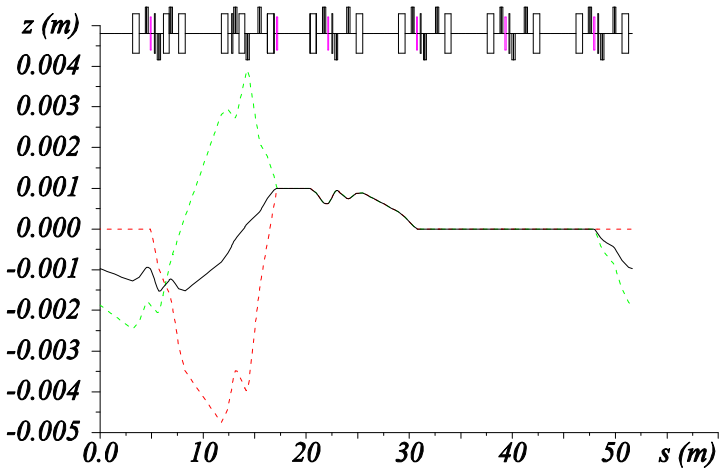

Fig. 6.21. Three different vertical closed orbits to get 1 mm change in the extraction section. Green line: VK6 only, red line: VK 1 only, black line: both combined gives a much smaller orbit deviation. The vertical correction elements are shown in pink in the magnet sequence at the top.

6.8. Tests of Slow Extraction at CRYRING

Tests of slow extraction were performed in CRYRING, using the electrostatic septum described in section 6.4 and a REX viewer, c.f. section 3.12, at the position foreseen for the magnetic septum. The REX viewer was provided with a rim, imitating the septum coil, to ensure that the particles seen by the viewer were not simply scraped off the beam, but that they had been deflected by the electrostatic septum. The third-integer resonance was excited by one sextupole magnet, and broadband noise on the transverse diagnostics kicker was used to drive particles out of stable phase space. The positions of these components are seen in fig. 6.22.

The REX viewer had video camera, allowing the position and intensity of the beam extracted on the detector could be visualized on a computer screen. In addition, a fast timing signal was picked up from the back surface of the MCP stack and connected, through a timing-filter amplifier and a constant-fraction discriminator, to a multi-scaler PC card. This allowed the count rate of the detector to be monitored on the PC. The current in the ring was 20–40 nA and the extraction time sufficiently long for the MCP to be well below saturation, and the registered count rate was thus proportional to the particle current on the detector.

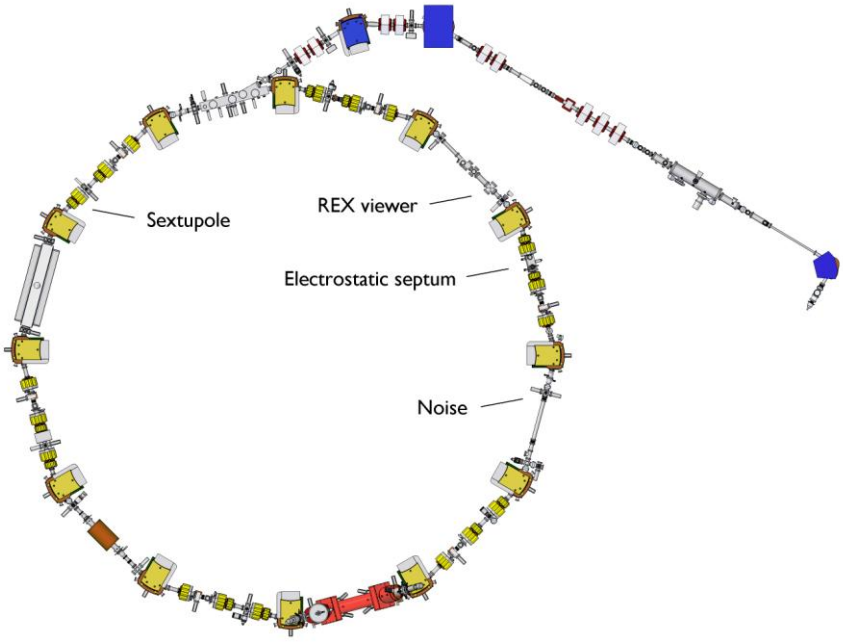

Fig. 6.22. Hardware components used for tests of slow extraction.

The extraction tests were performed with a beam of 3 MeV/u deuterons, chosen mainly because it is one of the easiest beams to set up at CRYRING. The horizontal tune was slightly below the 2 1/3 resonance at approximately 2.32. After acceleration, the sextupole was ramped up and the beam was cooled for 5 s before the noise on the diagnostics kicker was switched on for 2 s. The cooling was off during the extraction. The noise had an approximately constant spectral density over the 3 MHz bandwidth of the kicker amplifier, see section 3.12, and the noise amplitude, as measured on an oscilloscope, was approximately 60 V.

For simplicity, only one sextupole was excited, namely the focusing sextupole two superperiods downstream from the electrostatic septum, c.f. fig. 6.22. The outgoing leg of the separatrix then intersects the electrostatic septum at an x' which is somewhat smaller than optimal, requiring a correspondingly higher voltage on the electrostatic septum, but this was of no concern at the 3 MeV/u particle energy. The beam started to decay as soon as the noise was turned on, but it was seen on the detector only when the correct sextupole was excited. All settings were constant during the 2 s extraction time, including quadrupoles, sextupoles and noise power.

Fig. 6.23 shows an example of the current extracted on the detector during a 2-s interval, starting when the noise is turned on. The current has a large ripple, and also shown in the figure is a smoothened curve representing a sliding average over 20 ms, i.e. over one 50-Hz period. As stated in section 3.14, the ripple on the extracted current is mainly expected to derive from the current ripple on the focusing quadrupoles. The absolute amplitude of the quadrupole ripple is approximately independent of the value of the current, and the relative amplitude is thus expected to be in the order of 5×10^{-5} for the 3-MeV/u deuterons. The lower right plot of fig. 6.19 shows the simulated effect on the extracted current of 300 keV protons from a 150-Hz quadrupole ripple that has twice this amplitude, or 1×10^{-4}, and it is rather similar to what is seen in the figure below. This indicates a qualitative agreement between measurements and expectations, but a more detailed comparison would have to include a

more detailed knowledge and analysis of the different harmonics of the magnet ripple and their relative phases on both focusing and defocusing quadrupoles at this specific magnet current.

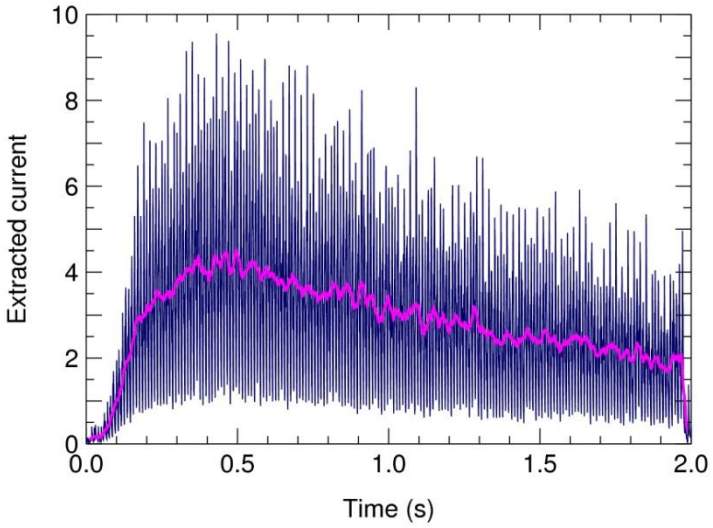

Fig. 6.23. Extracted current (arbitrary scale) measured on the MCP anode of the REX viewer, in blue. The smoothened pink curve is a sliding 20-ms average of the current.

A Fourier transform of the current in fig. 6.23 is shown in fig. 6.24. The dominating frequency component is 100 Hz. As with the current, no sufficiently detailed study of the quadrupole ripple has been made to allow a comparison between measured and expected harmonic contents.

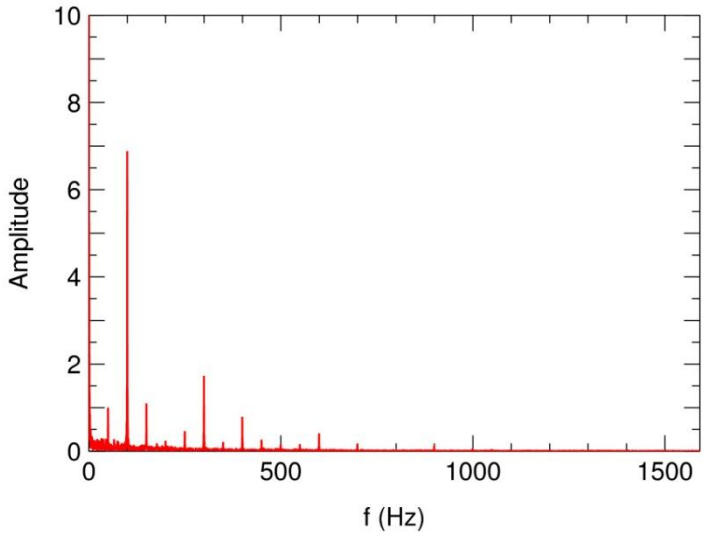

Fig. 6.24. Fourier transform of the extracted current in fig. 6.23, showing that 100 Hz is the dominating frequency component.

Given the count rate on the detector and the current of the circulating beam, the extraction efficiency was calculated to be 30–60%. With the beam current measured to an accuracy of about 10% with the AC current transformer (see section 3.12), the main uncertainty in the extraction efficiency is due to the uncertainty in the efficiency of the detector. This efficiency is expected to be in the range between 55% (the open-area ratio of the MCP) and 100%, depending on the secondary-electron yield when an

ion hits the Al plate of the detector, resulting in the above range of extraction efficiencies. This is somewhat less than one would hope for during production, and there is room for more careful optimizations as well as for measures to counteract the magnet ripple as discussed in sections 3.14 and 6.6.2.6. Nevertheless, these tests have successfully demonstrated slow extraction from CRYRING.

7. Experimental Investigations Related to Deceleration of Protons at CRYRING

7.1. Motivation for Beam Experiments

Between 2004 and 2007, a series of studies and measurements were made at CRYRING in order to investigate how well the ring could be expected to perform as a deceleration ring at FAIR. It was clear already at the start of the discussions about transferring CRYRING to FAIR that the ring fulfilled many of the requirements for this new task. The injection was not designed for 30 MeV particles and extraction was missing, but otherwise it had the right energy range, efficient electron cooling, very good vacuum, etc. In addition to the ring having a suitable hardware configuration, the relevant features had been in routine operation and used for experiments in atomic and molecular physics since a long time. One example is that the ring had been operating in deceleration mode as well as in acceleration mode, although deceleration had not been performed through the entire energy range that will be needed at FLAIR. Another example is that both positive and negative ions had been used, among both them protons and negative hydrogen ions, H^-. From an operational point of view, protons are the same as antiprotons apart from a polarity change of magnets and electrical fields. Such polarity changes have routinely been performed in a few hours, and comparisons between running protons and H^- indeed have shown that the two behave in a very similar way in the ring (apart from the lifetime which is much shorter for the H^- since it easily can lose an electron in collisions with the residual gas). At the other end of the particle spectrum of interest for FLAIR, heavy highly charged ions from the EBIS and ECR ion sources, up to $^{208}Pb^{55+}$, have been used, giving experience of, e.g., the lifetime of highly charged ions at energies down to the injection energy of 300 keV per nucleon.

Of particular interest in terms of expected performance is the throughput of antiprotons, which for instance can be measured as the maximum number of antiprotons that can be decelerated per unit time. Other similar and also interesting performance criteria are the maximum number of antiprotons that can be decelerated in one batch or the minimum particles losses that can be achieved during a deceleration cycle. The machine studies have thus focused on the following items [46]:

- Maximum intensity of stored protons
- Cooling forces and cooling times
- Deceleration of protons through the entire range from 30 MeV to 300 keV
- Losses during deceleration

Another reason for performing these studies have been to verify that the diagnostics is sufficient to perform the deceleration with reasonable ease, and that the operational procedures were sufficiently well developed in order to set up a decelerated beam with a reasonable effort and within a reasonable amount of time.

7.2. Space-Charge Limit

The intensity limit in a small low-energy ring as CRYRING, i.e., the maximum number of particles that can be stored or accelerated/decelerated, is normally determined by the space-charge limit. The space-charge of an intense beam tends to defocus the beam, and the defocusing action is different for particles at different radii from the beam centre. This defocusing adds to the focusing or defocusing

due to the quadrupole magnets in the ring, changing the tune of the particles (the number of betatron oscillations per turn). Since the tune change is different for different particles, the result is a tune spread, and the tune spread must always be sufficiently small so that no particles enter into strong resonances where the tunes Q_x and Q_y are rational numbers with small denominators, or more generally where $mQ_x + nQ_y = p$ and m, n, and p are small integers in the case of transversely coupled motion.

The space-charge tune shift, or incoherent tune shift, ΔQ is the tune change for a particle at the centre of the beam performing small betatron oscillations (where the change is largest), and its magnitude is [43]

$$\Delta Q = -\frac{N r_0}{4\varepsilon\beta^2\gamma^3}, \tag{7.1}$$

where N is the total number of particles in the ring, r_0 is the classical particle radius, ε the un-normalized beam emittance and β and γ are the usual relativistic factors. In the LSR, γ is close to unity, and the tune shift is thus to a good approximation inversely proportional to the particle energy. For completeness, the classical particle radius is given by

$$r_0 = \frac{q^2}{4\pi\varepsilon_0 m c^2},$$

where $q = Zq_e$ is the particle charge and $m \approx Am_p$ its mass. The emittance is defined as

$$\varepsilon = \frac{\pi\sigma^2}{\beta}$$

for a round Gaussian beam with radius σ at a point in the ring where the beta function is β (note the two different meanings of β).

This applies for a coasting beam distributed evenly over the entire ring circumference. For a bunched beam, the expression for the tune shift, equation (7.1), has to be divided by a bunching factor B equal to the ratio between the effective bunch length and the ring circumference.

Tests were performed at CRYRING in order to verify that particles could be stored up to this space-charge limit. Given the maximal particle number, the maximum allowed tune shift could then be calculated from equation (7.1). The tests were performed at the injection energy where the space-charge limit is most severe, and protons were used both because the settings of the ring are the same as for antiprotons and because they have a comparatively long lifetime at their injection energy of 300 keV. The particle intensity was increased gradually using cooler stacking with pulses coming from the injector at a rate of 2 Hz at the same time as the beam was cooled using the electron cooler. The cooling also damps coherent instabilities which may arise as the intensity grows (CRYRING has no system for active damping of such instabilities).

The highest number of stored protons that could be achieved in this way, after several minutes of accumulation, was 4.7×10^9. Both the longitudinal and transverse beam profiles were observed using

residual-gas beam-profile monitors [33], and the emittances were estimated to 15π mm mrad horizontally and 5π mm mrad vertically.

Fig. 7.1 shows the theoretical space-charge limit for a coasting protons according to expression (7.1). The three lines represent three different emittances, and a maximum tune shift of a rather conservative −0.02 is assumed. It is planned that LSR will decelerate the antiprotons to 300 keV, and below this energy, further deceleration in the USR ring (Ultralow energy Storage Ring) is assumed to take place.

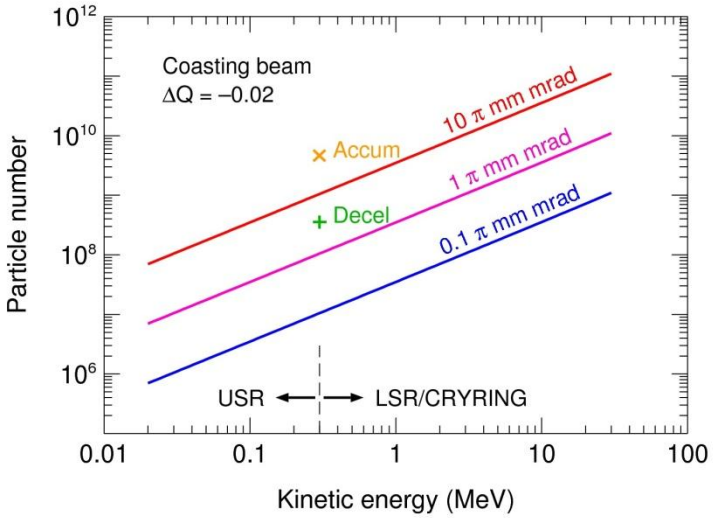

Fig. 7.1. Space-charge limit in LSR/CRYRING and USR for a coasting beam with maximum allowed tune shift of −0.02, indicated by lines for different (1σ) emittances. The two crosses represent the highest number of protons that has been stored in CRYRING and, as described further down in the text, the highest number of protons that has been decelerated from 30 MeV to 300 keV.

Also shown in fig. 7.1 is the result of the machine studies, represented by a cross at 300 keV and 4.7×10^9 particles. With the measured emittance of 15π mm mrad horizontally and 5 mm mrad vertically, the actual tune shift can be calculated to approximately −0.1. This beam was, however, quite unstable and easily disrupted by what was assumed to be coherent instabilities. Taking this into account and also a bunching factor, it was predicted that it would not be possible to decelerate more than 1×10^9 protons or antiprotons [47] with a beam emittance of 10π mm mrad. As seen below and also indicated in the figure, the highest number of protons that has actually been decelerated to 300 keV is above 3×10^8.

7.3. Electron Cooling of H⁻ ions

It is foreseen that beams that are decelerated in the LSR will have to be electron-cooled at one or two energies. In order to understand how long a deceleration cycle will be, which is a parameter that may affect the throughput of antiprotons or ions through the LSR, it is necessary to estimate the time needed to cool the beam.

The cooling time can in principle be estimated from experience at CRYRING, where measurements of cooling forces and cooling times, both longitudinally and transversally, have been made at many occasions, and they also have been compared to results from other electron coolers [22, 23]. It is

interesting, however, that electron cooling may act differently on positive and negative particles, and that negative particles may cool faster than positive particles.

Electron cooling is in the first approximation based on the Coulomb interaction between the electrons in the cooler and the stored ions, and then cooling rates should only be sensitive to the ion charge squared. However, the magnetic field in the cooler makes the ion–electron interaction more complicated and can create effects that depend on the sign of the ion charge. Such effects were seen in measurements of drag forces on protons and H^- ions in Novosibirsk [48], where a stronger drag force was observed for the negatively charged particles. If this is true also for beam parameters relevant for the LSR, antiprotons may cool faster than protons.

In order to investigate whether such a difference between positive and negative ions can be seen at CRYRING, both longitudinal and transverse cooling of H^- ions were studied and compared to existing data for positive ions.

7.3.1. Longitudinal Drag Force

The longitudinal drag force, or cooling force, is the longitudinal force exerted by the cooler electrons on an ion with a purely longitudinal velocity. Studies of this force have been performed at CRYRING with several different methods [22] on a number of different ion species, but prior to the discussions about FLAIR, no measurements hade been made with negative ions. A comparison between protons and H^- ions have now been made, however, with a result shown in fig. 7.2. For both particle species the energy was 3 MeV, and only 14 mA electron current was used, corresponding to an electron density of 2.9×10^{12} m^{-3}. The drag force in the figure is normalized to an electron density of 1×10^{14} m^{-3} to allow an easy comparison with earlier data. Due to the low injection rigidity of protons and H^-, the magnetic field in the cooling solenoid was 150 G instead of the 300 G normally used in CRYRING.

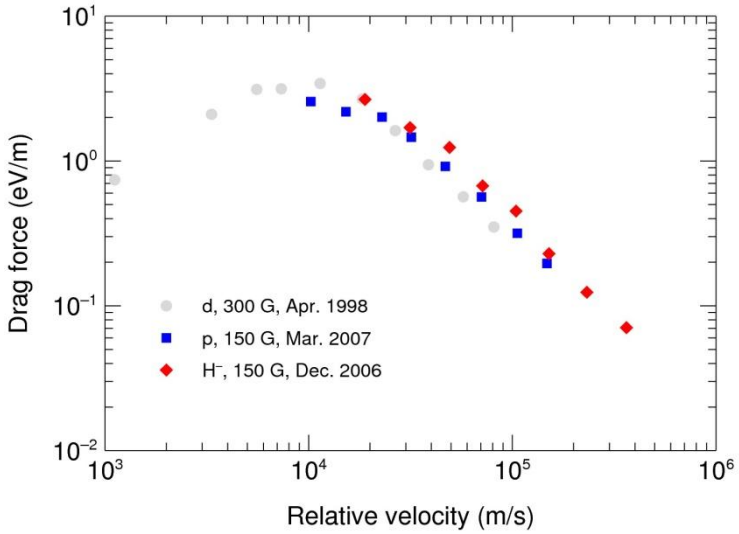

Fig. 7.2. Longitudinal drag force for protons and H^- ions compared to earlier measurements on deuterons [23]. The force is normalized to an electron density of 1×10^{14} m^{-3}.

From the figure, it seems that the drag force on the negative ions indeed is slightly higher. However, it is known from experience that the reproducibility of this kind of measurement is limited and that variations in data taken at different occasions are of a similar order of magnitude as the difference between the protons and the H^-. Thus it is not possible to conclude from these measurements that there is any difference in the drag force between positive and negative ions at the beam and cooler parameters used here.

7.3.2. Transverse Cooling Times

There is no simple way of measuring the transverse drag force, and from a practical point of view, cooling times are more important than cooling forces. The transverse cooling time is in addition expected to dominate over the longitudinal one since the electrons are colder longitudinally than transversally. Thus, H^- was compared to positive ions also with respect to transverse cooling times. The H^- measurements were made at an energy of 3 MeV which is representative for the energy range of the LSR and is also close to the 4.2 MeV where earlier data for positive ions used for comparison were taken.

Fig. 7.3 shows a set of vertical beam profiles, measured with a residual-gas-ionization beam-profile monitor [33]. The initial beam emittance was approximately 5π mm mrad, which is more than expected for antiprotons at 3 MeV if they are injected with 0.25π mm mrad emittance at 30 MeV (estimated from [50], where 0.05π mm mrad is given for a coasting beam at 30 MeV). The beam was cooled using an electron current of 18 mA, giving an electron density of 3.8×10^{12} m^{-3}. As usual for electron cooling, the particle in the centre of the distribution cool faster, which is due to the strength of the electron–ion interaction as a function of relative velocity. After 1 s, however, also the particles at the edge of the distribution have been substantially cooled, and after 1.5 s, a steady-state condition was reached.

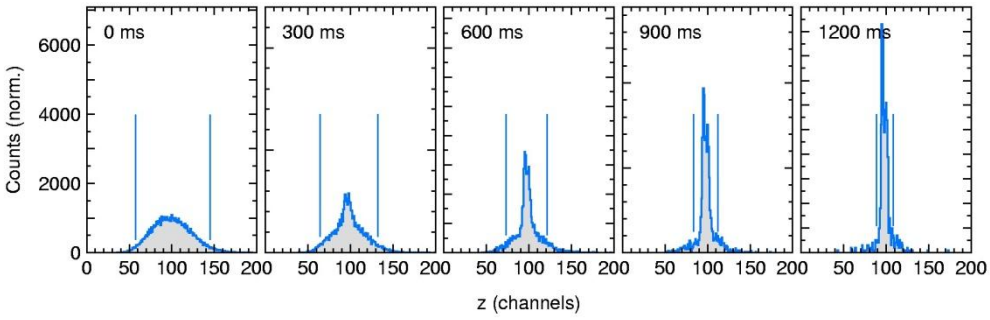

Fig. 7.3. Transverse beam profiles during electron cooling of H^- ions. The full horizontal scale of 200 channels corresponds to 40 mm, and the time interval between the profiles is 300 ms. The markers are added manually and are intended to give a representative measure of the beam width.

The resulting cooling time can be compared to previous measurements of transverse cooling times for singly and multiply charged ions in CRYRING [49]. In those measurements, hollow ion beams were produced by misaligning the electron beam with respect to the ion beam, such that all ions performed betatron oscillations with the same amplitude, and cooling rates could thus be determined as a function of betatron amplitude. Such hollow beams were not used in the present studies of H^- ions. Instead markers were put manually in an attempt to get a representative beam width, as indicated in fig. 7.3.

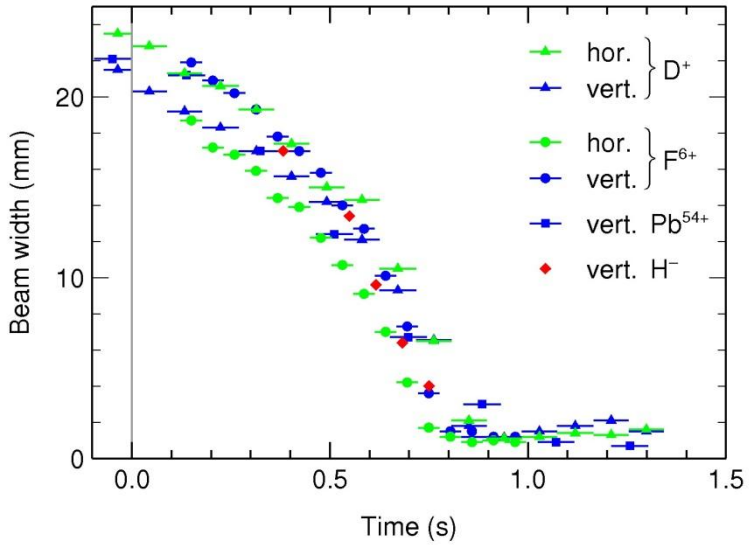

Fig. 7.4. Normalized transverse cooling times of positive ions with different charge states [49] and of H^- ions. The H^- data are normalized to the same electron density of 1.7×10^{13} m^{-3} as used for the positive ions, and these were in addition scaled with $q^{1.7/A}$. The new H^- data points were also shifted horizontally so that the beam reaches a cold equilibrium at approximately 0.7 s, as was the case for the positive ions.

Fig. 7.4 shows the beam size as a function of time for the H^- ions together with the earlier results for positive ions. The data for the different ion species are normalized to the same electron density of 1.7×10^{13} m^{-3}, which is the reason why the cooling time for H^- appears shorter in fig. 7.4 compared to fig. 7.3. The definition of $t = 0$ is related to how the earlier measurements were made, and the points for H^- are shifted horizontally so that the approximately coincide with the earlier measurements where the beam reached a cold equilibrium at 0.7 s.

Although there is a small uncertainty due to the difference in the definition of the beam width, no significant difference in cooling times between negative and positive ions is seen. At the same time, the cooling time is found to be so short compared to, e.g., the cooling time in the NESR ring [50], that electron cooling in the LSR will not limit the amount of antiprotons that can be decelerated per unit time at FLAIR.

7.4. Deceleration of Protons

The best way of determining how CRYRING will perform as a deceleration ring at FLAIR is to set up the machine for deceleration through the same energy range as at FLAIR and study what cycle time is required, what the efficiency is, i.e., how small the particle losses can be, etc. For these studies, protons were used in order to have particles with the same | q/A | as antiprotons. This is somewhat important since protons or antiprotons at 300 keV have a rigidity which is only 0.056 times the maximum rigidity of 1.44 Tm, and remanence and hysteresis effects in the ring magnets then become noticeable. The difference between positive and negative particles is, however, not expected to be significant. Only a polarity change of magnets and of some electrostatic elements is required, and experience tells that there is no difference in the behaviour of the machine depending on the polarity. These tests could in principle have been made with H^- ions, but the lifetime of the H^- ions is of the same order of magnitude as the length of the deceleration cycle, so it would have been difficult to

separate beam losses due to problems with the deceleration as such from losses due to detachment of the loosely bound extra electron of H^- in collisions with the residual gas.

There is no way to inject 30 MeV protons into CRYRING. Instead the tests were made with protons that were injected at the usual 300 keV and then accelerated to 30 MeV before they were decelerated back to 300 keV again [46]. This does not imply, however, that deceleration can be performed just by reversing the magnet and rf ramps used for acceleration. Remanence and hysteresis effects in the magnets make the deceleration process completely independent of the acceleration. Only beam parameters such as emittance and time structure depend to some extent on how the acceleration was made.

Fig. 7.5 shows an example of an acceleration–deceleration cycle with beam current as a function of time on the left scale and the corresponding particle number on the right scale. The beam current was measured with the Bergoz DC current transformer (c.f. section 3.12), and to reduce the noise, the curves in the figure are averages over many machine cycles. To reach maximum beam intensity, cooler stacking was used in the same way as for the tests of the space-charge limit as described above. The 2 Hz stepwise increase in beam current before $t = 0$ can with some effort be discerned in the figure. At $t = 0$, acceleration starts after a current of 4.9 μA, corresponding to 2.1×10^8 protons, has been accumulated.

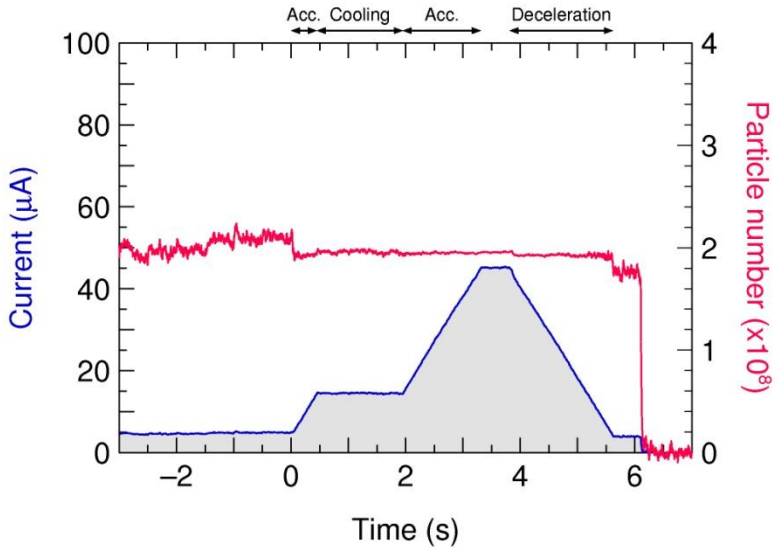

Fig. 7.5. Proton beam current (left scale and lower blue curve) and particle number (right scale and upper red curve) as functions of time during an acceleration–deceleration cycle.

The acceleration is made in two steps, first to 3 MeV in a little less than 0.5 s, then the beam is cooled for 1.5 s before the final acceleration to 30 MeV is made. The reason for cooling at 3 MeV is discussed below. The beam current is proportional to the particle number and to the beam velocity (or the square root of energy for non-relativistic particles). It is seen that there is a small loss of particles, about 5%, at the start of the acceleration. Otherwise there is no significant loss during acceleration or cooling and the current indeed increases by close to a factor 10 when the energy increases from 300 keV to 30 MeV. The beam was bunched during the entire cycle, including the cooling period and the flat top.

At 4 s into the cycle, the deceleration back to 300 keV started. There was a very small loss of particles at the start of the deceleration ramp, otherwise it is seen that no further losses occurred during the ramp down which lasted 1.8 s. Only when the ramp met the flat bottom there was another loss of approximately 5%, but it should be noted that no cooling was needed during the ramp down. At 6.1 s, the beam was dumped, and a new cycle started. Out of the initial 2.1×10^8 protons, 1.8×10^8 remained at the end of the cycle, implying a total efficiency of 85%. However, only the efficiency in deceleration from 30 MeV to 300 keV is important at FLAIR, and from these measurements one can conclude that it is possible to perform this deceleration with at least 90% efficiency, i.e. at most 10% losses, given the beam properties at 30 MeV of this experiment. The plot of fig. 7.5 is the result of about one day of tuning of ring parameters such as magnet and rf ramps, settings of sextupoles and correction dipoles, etc., and one can assume that the efficiency can be improved further with more optimization of these parameters.

Fig. 7.6 shows a similar acceleration–deceleration cycle but with an initial beam current almost twice as high. Here the losses are somewhat larger, in particular when the deceleration ramp meets the flat bottom. Nevertheless, 2.8×10^8 particles were brought back to 300 keV. The highest number of protons that have been decelerated from 30 MeV to 300 keV and stored at that energy is 3.6×10^8, in which case the losses were still somewhat higher. This number is compared to the space-charge limit in fig. 7.1 and agrees quite well with it, taking the bunching factor into account. One can conclude that protons can be decelerated in CRYRING up to an intensity which is close to the space-charge limit.

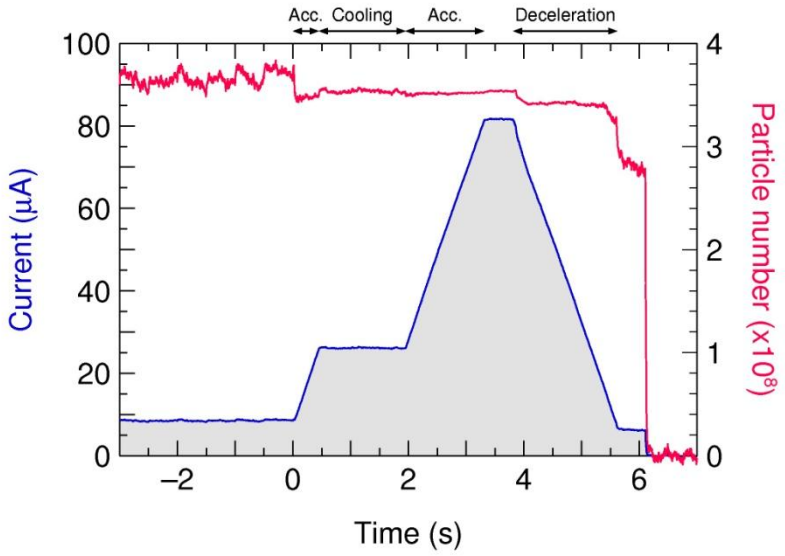

Fig. 7.6. Proton beam current (left scale and lower blue curve) and particle number (right scale and upper red curve) as functions of time during an acceleration–deceleration cycle for a higher injected intensity than in fig. 7.5.

7.5. The Need for Cooling at Studies of Deceleration

In the first tests of deceleration at CRYRING, no intermediate cooling was performed during the acceleration phase. Cooling was only applied at the injection energy, before what is defined as $t = 0$ in fig. 7.5 and fig. 7.6. It was then not possible to decelerate the beam from 30 MeV without getting large

losses, more than 50%, at the start of the ramp down [51]. This problem was alleviated with the introduction of the cooling plateau at 3 MeV during the acceleration.

The cooling at injection energy reduces the transverse emittance of the beam and also the momentum spread. Although the equilibrium values are rather high since the intensity approaches the space-charge limit as discussed above, acceleration can be performed without losses. It therefore seemed unlikely that, for instance, a too large transverse emittance was causing the losses at the start of the deceleration. Instead, some investigations were made concerning the longitudinal structure of the bunched beam during the same acceleration–deceleration cycle as above from 300 keV to 30 MeV and back again. As before, the rf was on with a constant amplitude during the entire cycle from the start of the acceleration, keeping the beam continuously bunched from the acceleration phase to the deceleration.

Fig. 7.7a shows an acceleration–deceleration cycle which has a plateau at 3 MeV during the acceleration phase, but where no cooling was applied at that plateau. Also shown, in the inset, is the bunch shape at 30 MeV, just before deceleration starts. The bunch shape was measured with an electrostatic pickup connected to an oscilloscope, and the bunches are nearly sinusoidal due to the strong longitudinal space-charge force at low energy. Under these conditions it is seen that about 1/3 of the beam intensity is lost as the deceleration starts.

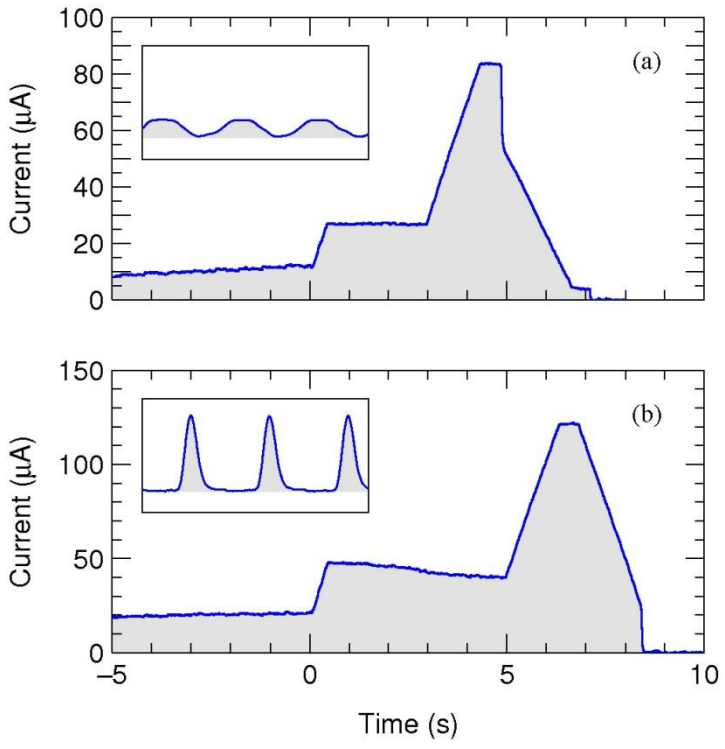

Fig. 7.7. Proton beam current during an acceleration cycle with (a) cooling only at the injection energy before $t = 0$ and (b) cooling applied also at 3 MeV between $t = 0.5$ and 5 s. The beam was bunched from $t = 0$ and onward, and the insets show the bunch shape at the flat top of 30 MeV. The machine settings were not as well optimized as when fig. 7.5 and fig. 7.6 were taken, instead the focus was on the losses at the start of the deceleration (at $t = 5$ and 7 s respectively) which showed a strong correlation with bunch length.

The cycle in fig. 7.7b is similar, but here cooling was applied at the 3-MeV plateau. As a result, the bunches are much shorter, as seen in the inset. Due to less well optimized machine settings, perhaps in combination with an accumulated current twice as high as in fig. 7.6, there were now losses during the cooling, and all of the beam was lost at the end of the deceleration ramp. The focus was, however, on the losses at the start of the deceleration, and it is clear that they are virtually non-existent. Over all, a strong correlation between bunch length and beam losses at the start of the deceleration was found, and it is expected that bunches filling 50−60% or less of the ring circumference can be decelerated in the LSR ring without further developments.

References

[1] FLAIR Technical Proposal, unpublished.

[2] K. Abrahamsson, G. Andler, L. Bagge, E. Beebe, P. Carlé, H. Danared, S. Egnell, K. Ehrnstén, M. Engström, C.J. Herrlander, J. Hilke, J. Jeansson, A. Källberg, S. Leontein, L. Liljeby, A. Nilsson, A. Paál, K.-G. Rensfelt, U. Rosengård, A. Simonsson, A. Soltan, J. Starker, M. af Ugglas and A. Filevich, Nucl. Instr. Meth. B **79** (1993) 269.

[3] C.J. Herrlander and A. Bárány, Proc. ECOOL 84, KfK 3846, Ed. H. Poth (Kernforschungs-zentrum Karlsruhe 1984), p. 429.

[4] C.J. Herrlander, L. Bagge, A. Bárány, S. Borg, H. Danared, P. Heikkinen, S. Hultberg, L. Liljeby and Th. Lindblad, Proc. Part. Acc. Conf., PAC 85, IEEE Trans. Nucl. Sci. NS **32** (1985) 2718.

[5] A Bárány, C.J. Herrlander, K.-G. Rensfelt and J. Starker, Nucl. Instr. Meth. B **23** (1987) 200.

[6] S. Borg, H. Danared and L. Liljeby, Proc. Third Int. EBIS Workshop, Eds. V. O. Kostroun and R. W. Schmieder (Cornell Univ. 1985) p. 47.

[7] J. Arianer, C. Goldstein, H. Laurent and M. Malard, Proc. Part. Acc. Conf., PAC 83, IEEE Trans. Nucl. Sci. NS **30** (1983) 2737.

[8] U. Rosengård, G. Rouleau and K.-G. Rensfelt, Nucl. Instr. Meth. B **139** (1998) 428.

[9] Publications and Dissertations from the CRYRING Facility 1992–2010, Manne Siegbahn Laboratory, Stockholm University 2010.

[10] A. Simonsson, Ph. D. Thesis, Manne Siegbahn Institute of Physics and Royal Institute of Technology, Stockholm, 1991.

[11] A. Schempp, H. Deitinghoff, M. Ferch, P. Junior and H. Klein, Nucl. Instr. Meth. B **10/11** (1985) 831.

[12] P. Heikkinen, Ph. D. Thesis, Department of Physics, University of Jyväskylä, Research Report No. 1/1987.

[13] J. Jeansson and A. Simonsson, Proc. Eur. Part. Acc. Conf., EPAC 88, Ed. S. Tazzari (World Scientific 1989), p. 720.

[14] K. Abrahamsson, G. Andler and C.B. Bigham, Nucl. Instr. Meth. B **31** (1988) 475.

[15] K. Abrahamsson, G. Andler and C.B. Bigham, Proc. Eur. Part. Acc. Conf., EPAC 88, Ed. S. Tazzari (World Scientific 1989), p. 935.

[16] G. Dôme, CERN Accelerator School Oxford 1985, CERN 87-03 p. 110.

[17] L. Bagge, H. Danared, K. Ehrnstén, C.J. Herrlander, J. Hilke, A. Nilsson and K.-G. Rensfelt, Vacuum **44** (1993) 497.

[18] A. W. Chao and M. Tigner, "Handbook of Accelerator Physics and Engineering", World Scientific, Singapore, 1999.

[19] H. Danared, Phys. Scr. **48** (1993) 405.

[20] H. Danared, Nucl. Instr. Meth. A **335** (1993) 397.

[21] H. Danared, G. Andler, L. Bagge, C.J. Herrlander, J.Hilke, J. Jeansson, A. Källberg, A. Nilsson, A. Paál, K.-G. Rensfelt, U. Rosengård, J. Starker and M. af Ugglas, Phys. Rev. Lett. **72** (1994) 3775.

[22] H. Danared, Nucl. Instr. Meth. A **391** (1997) 24.

[23] H. Danared, A. Källberg, G. Andler, L. Bagge, F. Österdahl, A. Paál, K.-G. Rensfelt, A. Simonsson, Ö. Skeppstedt and M. af Ugglas, Nucl. Instr. Meth. A **441** (2000) 123.

[24] G. Gwinner, A. Hoffknecht, T. Bartsch, M. Beutelspacher, N. Eklöw, P. Glans, M. Grieser, S. Krohn, E. Lindroth, A. Müller, A.A. Saghiri, S. Schippers, U. Schramm, D. Schwalm, M. Tokman, G. Wissler and A. Wolf, Phys. Rev. Lett. **84** (2000) 4822.

[25] V.I. Kudelainen, V.A. Lebedev, I.N. Meshkov, V.V. Parkhomchuk and B.N. Sukhina, Sov. Phys. JETP **56** (1982) 1191.
[26] U. Rosengård, S. Leontein, A. Nilsson, A. Paál, A. Filevich and G. Szekely, Proc DIPAC 93, CERN PS/93-35, p. 136.
[27]. K. Kruglov, L. Weissman, P.Van den Bergh, A. Andreyev, M. Huyse and P.Van Duppen, Nucl. Instr. Meth. A **441** (2000) 595.
[28]. K. Kruglov, L. Weissman, P.Van den Bergh, M. Huyse and P.Van Duppen, Nucl. Phys. A **701** (2002) 193c.
[29]. A. Källberg and A. Simonsson, Proc. DIPAC 99 (Daresbury Laboratory 1999) p. 114.
[30] S. Leontein and E. Westlin, Proc. EPAC 98, Eds S. Myers *et al.* (Institute of Physics Publishing 1998), p. 1552.
[31] S. Borsuk, K. Agehed, W. Klamra and Th. Lindblad, Nucl. Instr. Meth. A **284** (1989) 430.
[32] S. Borsuk, M. Nadachowski, W. Klamra, Th. Lindblad and U. Rosengård, Nucl. Instr. Meth. A **316** (1992) 351.
[33] A. Källberg, A. Paál, J. Gál, J. Molnár and G. Szekely, Proc DIPAC 97, Laboratori Nazionali di Frascati LNF-97/048, p. 150.
[34] G. Andler, J. Axelsson, L. Bagge, M. Björkhage, P. Carlé, H. Danared, A. Källberg, L. Liljeby, K.-G. Rensfelt, A. Paál, U. Rosengård, A. Simonsson and M. af Ugglas, Proc. EPAC 98, Eds. S. Myers *et al.* (Institute of Physics Publishing 1998), p. 526.
[35] A. Paal, A. Simonsson, A. Källberg, J. Dietrich and I. Mohos, Proc. EPAC 04, Eds. J. Chrin *et al*., p. 2745.
[36] P. Löfgren, G. Andler, L. Bagge, M. Björkhage, M. Blom, H. Danared, A. Källberg, S. Leontein, L. Liljeby, A. Paal, K.-G. Rensfelt, A. Simonsson, H. Cederquist, M. Larsson, S. Rosén and H.T. Schmidt, Proc. EPAC 08, Eds. I. Andrian *et al*., p. 331.
[37] H.T. Schmidt, H.A.B. Johansson, R.D. Thomas, W.D. Geppert, N. Haag, P. Reinhed, S. Rosén, M. Larsson, H. Danared, K.-G. Rensfelt, L. Liljeby, L. Bagge, M. Björkhage, M. Blom, P. Löfgren, A. Källberg, A. Simonsson, A. Paál, H. Zettergren and H. Cederquist, Int. J. Astrobiol. **7** (2008) 205.
[38] H. Danared, A. Källberg, K.-G. Rensfelt and A. Simonsson, Phys. Rev. Lett. **88** (2000) 174801.
[39] J. Starker and M. Engström, Proc Int. Conf on Accelerator and Experimental Physics Control Systems, ICALEPS91 (KEK Proceedings 92-15, KEK, Tsukuba, Japan 1991) p. 167.
[40] K.T. Nielsen, J.S. Nielsen and T. Worm, Proc Int. Conf on Accelerator and Experimental Physics Control Systems, ICALEPS99 (Sincrotrone Trieste, Italy, 1999) p. 87.
[41] P. Carlé, J. Jeansson and A. Nilsson, Nucl. Instr. Meth. A **366** (1995) 31.
[42] Jian-lin Mi, AGS/AD/Tech. Note No. 295, Brookhaven National Lab. 1998.
[43] D.A. Edwards and M.J. Syphers, "An Introduction to the Physics of High Energy Accelerators", John Wiley & Sons, Inc., 1993.
[44] W. Hardt, J. Jäger and D. Möhl, CERN/PS/LEA 82−5.
[45] S. Guiducci, CERN Accelerator School, Jülich 1990, CERN Yellow Report 91−04, p. 53.
[46] H. Danared, A. Källberg and A. Simonsson, Proc. Workshop on Beam Cooling and Related Techniques, COOL 2007 (GSI, Darmstadt, Germany 2007), p. 234.
[47] H. Danared, A. Källberg and A. Simonsson, GSI Scientific Report 2005 (GSI, Darmstadt, Germany 2005), p. 5.
[48] N.S. Dikansky, V.I. Kudelainen, V.A. Lebedev, I.N. Meshkov, V.V. Parkhomchuk, A.A. Sery, A.N. Skrinsky, B.N. Sukhina, Preprint 88-61, INP Novosibirsk (1988).

[49] H. Danared, G. Andler, L. Bagge, A. Källberg, F. Österdahl, A. Paál, A. Simonsson and M. af Ugglas, Proc. EPAC 2000, Eds. J.-L. Laclare *et al*., p. 301.
[50] C. Dimopoulou, K. Beckert, P. Beller, A. Dolinkskii, U. Laier, F. Nolden, G. Schreiber, M. Steck and J. Yang, PRST-AB **10** (2007) 02010; C. Dimopoulou, O. Dolinskii, R.G. Heine, T. Katayama, U. Laier, F. Nolden, G. Schreiber and M. Steck, Proc. Workshop on Beam Cooling and Related Techniques, COOL 2009 (IMP, Lanzhou, China 2009).
[51] A. Bräuning-Demian *et al.*, GSI Scientific Report 2004 (GSI, Darmstadt, Germany 2004), p. 33.

Appendix 1, Offer from MSL to the FLAIR Collaboration

2007-11-23 Dnr. 26/07

Prof. Eberhard Widmann
Stefan Meyer Institute for Subatomic Physics
Austrian Academy of Sciences
Boltzmanngasse 3
A-1090 Vienna
Austria

Dear Eberhard,

Writing to you in your capacity as spokesperson for the FLAIR collaboration, we here wish to describe the proposal from the Manne Siegbahn Laboratory to provide CRYRING as a Swedish in-kind contribution to FAIR, for use as the LSR ring of the FLAIR facility.

As you know, a letter has been sent from the Swedish Ministry of Education to the German Ministry of Education and Research, acknowledging the willingness of the Swedish Government to commit itself "to a contribution to the construction of FAIR in the order of 10 million Euros, provided that at least 2 million Euros of these will be accounted for our proposed contribution of the upgraded CRYRING as the low energy storage ring (LSR) for the FLAIR project". If CRYRING thus will be accepted by FAIR, and if MSL gets the appropriate support from Swedish funding agencies, which we have no reason to doubt, MSL will be able to make necessary modifications to CRYRING, disassemble it and put it in storage by the end of 2010 at no cost to FAIR or the FLAIR collaboration, except that 2 million euro have to be counted as a Swedish contribution to FAIR.

The properties of CRYRING relating to its use as the LSR ring have been described in the FLAIR Technical Proposal, submitted in its latest version to GSI in December 2005. Since then it has been shown that CRYRING, as it looks already today, is capable of decelerating at least 3×10^8 protons from 30 MeV to 300 keV in less than 2 s (see, e.g., Proc. COOL07, http://bel.gsi.de/cool07/PAPERS/FRM2C04.PDF). Together with the fact that the ring is regularly running also with negative ions, including H^-, this shows that CRYRING would be able to perform very well as a deceleration ring for antiprotons at FLAIR. Deceleration of highly charged ions can, in addition, benefit from a fast ramping mode of the main magnet power converters which allows deceleration in 125 ms, minimizing recombination losses at low energies.

The MSL offer to FLAIR includes all components of the ring and its low-energy injector for singly charged ions such as they look today with some exceptions and additions. The exceptions include a number of outdated power supplies for the injection beamline and parts of the control system which we believe will not be useful at FLAIR. The additions are mainly new injection and extraction systems. The new injection will allow transfer of 30 MeV antiprotons and highly charged ions at the same rigidity from the NESR ring as well as ions from the low-energy injector. The extraction will allow fast and resonant extraction over a wide range of energies down to the lowest rigidity of LSR.

As part of this proposal, MSL provides all existing documentation of the ring components and also thoroughly documents the disassembly process such that the ring can be rebuilt at FLAIR with minimum effort once the FLAIR building is ready. MSL takes responsibility for the transport of the disassembled equipment to GSI and offers to take active part in the preparations for the installation of the LSR ring as we have done up to now, and to give advice during the reassembly and commissioning of the ring. MSL can not, however, promise to provide labour for reassembly or commissioning.

A list is enclosed to this letter showing all major components of CRYRING that are foreseen for transfer to FLAIR. Since it is not meaningful for MSL to purchase new power supplies just to put them in storage for several years, the acquisition of these will have to be the responsibility of the FLAIR collaboration, and their cost will have to be covered by the FLAIR collaboration or other sources. These items are specified in the enclosed list, and we estimate their total cost to 387 k€ in 2005 prices. This also includes the cost for reinstallation of the main magnet power converters by hired expertise, based on a preliminary quotation from a company related to the manufacturer.

The Manne Siegbahn Laboratory would be very happy to see CRYRING being modified and transferred to FAIR for use as the LSR ring, and we believe that it would be very well suited for this new purpose. The release of funds from the Swedish Research Council for the project of transferring CRYRING to FAIR of course requires that the FLAIR collaboration agrees to receive the ring. We would thus very much appreciate if you could take the necessary steps so that the FLAIR collaboration in a near future can come to a decision about whether or not it chooses to receive CRYRING.

Best regards,

Håkan Danared
Director, MSL

Encl.: List of major items offered to FLAIR

List of major items offered to FLAIR

- Ion source platform for singly charged ions, with power supplies
- Analysing magnet[1]
- Electrostatic deflectors and quadrupoles for injection beamline[2]
- RFQ with power supplies[3]
- Magnets for injection beamline[4]
- Injection and extraction systems with power supplies
- Ring magnets (dipoles, quadrupoles, sextupoles, correction dipoles)
- Power converters for ring magnets[5]
- Acceleration system[6]
- Electron cooler with power supplies[7]
- Vacuum chambers and valves for ring and injection beamline
- NEG pumps[8]
- Ion pumps[9]
- Baking jackets, including replacement of old ones using ceramic paper
- Diagnostics (Faraday cups, fluorescent screens, electrostatic pickups, Schottky pickup, current transformers, beam-profile monitors)
- Cables
- Mechanical supports
- Transport to GSI

Notes:

Estimated costs to the FLAIR collaboration in 2005 prices

1.	Magnet supply	22 k€
2.	High-voltage supplies	15 k€
3.	Rf amplifiers	25 k€
4.	Magnet supplies (depending on number of magnets)	77 k€
5.	Reinstallation of main magnet power converters	179 k€
6.	End stage for fast acceleration/deceleration (optional)	10 k€
7.	Isolation transformer	2 k€
8.	NEG bands	33 k€
9.	Ion-pump supplies	24 k€
Total		387 k€

Appendix 2. Comment on Offer to the FLAIR Collaboration and Outlook

When MSL's offer to the FLAIR collaboration, see Appendix 1, was written in 2007, it was anticipated that CRYRING could be reassembled as the LSR around 2013. Since then, the FAIR project has suffered delays of several years, and one should thus avoid to purchase new equipment that ages significantly over a period of 5–10 years. In Appendix 1, there is already a list of items that must be acquired by the FLAIR collaboration at the time of reassembly of the ring. To this list must be added a current supply for one of the septum magnets (one such supply, provided by the The Svedberg Laboratory, already exists). When the ring is reassembled, one must also expect to replace all rubber hoses for cooling water to the magnets as well as some minor items like channelplates for the beam-profile monitors.

Due to the delays of the FAIR project and to internal circumstances at MSL, the disassembly of CRYRING is now forseen to take place in the second half of 2011, such that it can be transported to Germany in late 2011 or early 2012. The boxes are expected to be stored in a warehouse in the vicinity of GSI/FAIR. According to a preliminary enquiry, the cost for such storage will be approximately 8000 € per year.

Once the FLAIR building is completed and ready for the LSR ring to be installed, the effort to reassemble the ring has been estimated to correspond to 30 person-months. Much of this work consists of manual tasks such as tightening flanges and pulling cables, although supervision of qualified accelerator scientists will be needed. Alignment of the machine is expected to take another 6 person-months. Additional resources will be required for the adaption of the ring to its new environment at FAIR as mentioned at the end of section 4.1, and one of the important points in this context will be the connection to the FAIR control system. When also the injector with its redesigned beamline has been assembled, the ring will be ready for commissioning.